Atomic Layer Deposition of Tin Oxide and Zinc Tin Oxide: Understanding the Reactions of Alkyl Metal Precursors with Ozone

A DISSERTATION
SUBMITTED TO THE FACULTY OF
UNIVERSITY OF MINNESOTA
BY

Ellis J. Warner

IN PARTIAL FULFILLMENT OF THE REQUIREMENTS
FOR THE DEGREE OF
DOCTOR OF PHILOSOPHY

Wayne L. Gladfelter, Advisor

September 2014

Copyright © 2014 by Ellis J. Warner

All rights reserved.
No part of this publication may be reproduced distributed, or transmitted in any form or by any means, including photocopying, recording, or other electronic or mechanical methods, without the prior written permission of the author except in the case of brief quotations embodied in critical reviews and certain other noncommercial uses permitted by copyright law.

Printed in the United States of America
First Printing, 2014

ACKNOWLEDGEMENTS

I would like to thank my advisor, Wayne L. Gladfelter, for his advice and support in my research projects. His expertise in chemistry and materials as well as his drive to gain a better understanding in everything we do has been a benefit in my professional development. I look forward to using the skills that I have acquired, both in scientific research and presentation, in my career.

I also would like to thank my colleagues in the Chemistry Department. My fellow graduate students—Josh Halverson, Rajan Vatassery, Ryan Hue, Clay Easterday, Amanda Oehrlein, and Thakshila Wickramaratne—and post-doctorate Vince West, I thank you all of your constant company and humor. I want to extend many thanks to Professor Stephen Campbell and his graduate student, Forrest Johnson, for their help in constructing electronic devices and general engineering advice. Special thanks also go to Professor Christopher Cramer and his graduate student, William Isley, for their excellent guidance in computational chemistry. Thanks to Shay Wallace, for AFM and ALD work performed over the semesters.

I want to express my gratitude to my parents, Dwight and Lynn Warner, and my in-laws, Edward Xu and Hui Wang, for their advice and financial support over the past four years.

Lastly, I would like to dedicate my dissertation to my wife, Ling Xu, whose encouragement, love, and support has been invaluable during my graduate studies.

TABLE OF CONTENTS

LIST OF FIGURES V

LIST OF TABLES IX

LIST OF SCHEMES X

1. CHAPTER ONE 1

1.1 Tunnel junction devices for multi-junction photovoltaic applications 2

1.2 Introduction to atomic layer deposition 6

1.2.1 Principles of ALD 6

1.2.2 ALD precursors for zinc oxide 8

1.2.3 ALD precursors for SnO_2 tin oxide 10

1.2.4 Depositing mixed metal oxides by ALD 12

1.3 Theoretical ALD mechanisms 14

2. CHAPTER TWO 17

2.1 ALD precursors and substrates 18

2.1.1 Glass and silicon substrate treatments 18

2.1.2 Precursors, vessels, and handling 19

2.2 Deposition Reactor 21

2.3 Characterization and theoretical techniques for tin and zinc tin oxide films 23

2.3.1 Spectroscopic ellispsometry 25

2.3.2 X-ray diffraction 27

2.3.3 Rutherford backscattering spectrometry 29

2.3.4 Atomic force microscopy (AFM) 32
2.3.5 Electron microscopy 34
2.3.6 Hall effect measurements 37
2.3.7 Quantum mechanical methods for computational chemistry 39

3. CHAPTER THREE 44

3.1 Introduction 45
3.2 Experimental 47
3.2.1 Computational Studies 47
3.2.2 Trapping the Organic Products Formed During ALD 48
3.3 RESULTS AND DISCUSSION 50
3.3.1 Design of Model Systems and Comparison to Known Structures 51
3.3.2 Step 1. Oxygen Atom Insertion Into the Zn-Et Bond 53
3.3.3 Step 2. Reaction of the Second Equivalent of Ozone with Zinc Ethoxide 61
3.3.4 Diethylzinc Additions to Zinc Hydroxyl Ligands 62
3.3.5 Detection of Acetaldehyde 66
3.3.6 Does Atomic Oxygen Play a Role? 68
3.4 Conclusions 70
3.5 Acknowledgement 71

4. CHAPTER FOUR 72

4.1 Summary 73
4.2 Introduction 74
4.3 Experimental 75
4.4 RESULTS AND DISCUSSION 77
4.4.1 ALD of SnO_2 with TET and Ozone 77

4.4.2 Sequential Deposition of ZTO Films 82
4.4.3 Fabrication of a Tunnel Junction Device 97
4.5 Conclusions 99
4.6 Acknowledgements 100
5. CHAPTER FIVE 101
5.1 Introduction 102
5.2 Experimental 103
5.3 Results and Discussion 105
5.3.1 ALD of SnO_2 with $SnMe_4$ and Ozone 105
5.3.2 ALD of SnO_2 with $SnBu_3Cl$, $SnBu_3H$ and Ozone 110
5.3.3 Reduced Temperature ALD of $SnEt_4$ and Ozone 113
5.3.4 Suppression of $SnEt_4$ in ternary oxides 116
5.3.5 Computational Studies of $SnEt_4$ with Ozone 120
5.3.6 Computational Studies of $SnEt_4$ with Metal Hydroxides 126
5.4 Conclusions 131
6. REFERENCE 134

LIST OF FIGURES

Figure 1.1	Multi-junction solar cell indicating two absorbers with different bandgaps.	3
Figure 1.2	Tunnel junction IV profile and band diagram depicting operation of tunnel junction.	5
Figure 1.3	Representative ALD of metal-alkyl (MEt_x) with water where the self limiting nature of ALD materials is achieved by sequential reaction of precursor and reactant following inert gas purges.	7
Figure 1.4	Tin precursors for ALD of SnO_X films.	11
Figure 1.5	Nanolaminate film from sequential ALD process	14
Figure 2.1	Stainless steel precursor vessels for ALD reactor	20
Figure 2.2	ALD reactor schematic showing the design of the deposition tool	22
Figure 2.3	Ellipsometry measurement indicating a phase shift and amplitude change in the reflected light versus incident light	27
Figure 2.4	Gemetric model for determining d-spacing in Bragg's law	29
Figure 2.5	Physics behind 1d elastic collisions which allow for the target mass to be determined from conservation of energy and momentum	30
Figure 2.6	Schematic of an AFM device indicating key components for measuring film roughness or step heights	33
Figure 2.7	Hall effect measurement illustrating the movement of carriers (*e*&*h*) with respect to an applied magnetic field and current	39
Figure 3.1	ALD reactor schematic showing diethylzinc and ozone precursors with nitrogen purge gas. Square and round valves	

denote manual and computer controlled valves. Valves 1 and 2 controll the precursor pulse entering into the trap, and valve 3 controls all precursor pulses that bypass the trap 49

Figure 3.2 Reaction coordinate showing the insertion of ozone into the Zn-Et bond of the (HO)ZnEt. Hydrogen atoms are white, carbon atoms gray, oxygen atoms red and zinc atoms are slate blue. Lines connecting stationary points are provided for viewing convenience. 55

Figure 3.3 Reaction coordinate showing the insertion of ozone into the Zn-Et bond of the $(HO)_7Zn_4Et$. 60

Figure 3.4 Reaction coordinate for the second ozone reaction leading to the elimination of acetaldehyde 62

Figure 3.5 Reaction coordinate for the 1,2-elimination of ethane upon addition of $ZnEt_2$. 65

Figure 3.6 Reaction coordinate for the 1,2- and 1,4-elimination of ethane from the cubane-like model. 66

Figure 3.7 Graph correlating the quantity of acetaldehyde and the number of ALD cycles 68

Figure 4.1 The saturation curve for SnO_2 deposition as a function of TET pulse time versus deposition rate. 79

Figure 4.2 ALD window for SnO_2 deposition using TET and O_3 precursors each data point corresponds to the average deposition rate of 3 films and the error bars indicate the standard deviation between these films. The inset indicates the observed thicknesses for films deposited close to the hot zone inlet and close to the hot zone outlet. 80

Figure 4.3 Representative RBS spectrum of ZTO and tin oxide films deposited on silicon substrates using TET&O_3 within the ALD window. 81

Figure 4.4 Deposition rate of ZTO as a fraction of tin cycles per super cycle plotted on the left axis. Film composition as measured by RBS is plotted on the right axis. 83

Figure 4.5 ZTO film densities as measured by RBS and calculated using a theoretical bulk density model. 86

Figure 4.6 Cross section of ZTO film measured by TEM, including STEM HADDF EDX (55 nm) line scan for elemental analysis. 88

Figure 4.7 Optimized geometries of tetrahedral IV-VI materials used for calculating densities of amorphous quartz phase materials and predicting the density of 4-coordiante tin oxide. 89

Figure 4.8 X-ray diffraction of ZTO films from 3:1 TET/O_3 to DEZ/O_3 to 8:1 TET/O3 to DEZ/O_3 including an annealed SnO_2 film and a 450 °C annealed 4:1 TET/O3 to DEZ/O_3. In addition to the XRD patterns, the Ilmenite $ZnSnO_3$ (PDF 52-1381) is included on the x-axis.[4] 93

Figure 4.9 Carrier concentration and electron mobility as a function of film tin concentration in 450 °C annealed ZTO films. 95

Figure 4.10 Optical transmission of 58 at.% Sn ZTO film Tauc plot (inset) for bandgap as a function of film composition 3.40, 3.42, 3.77 eV for 37, 58, 85 at.% tin. 97

Figure 4.11 Current vs. Voltage (IV) profile of a tunnel junction device composed of sputtered Cu_2O and ALD deposited $ZnSnO_3$ on an AZO/ITO coated glass substrate. 98

Figure 5.1 Thickness per cycle (TPC) of SnO_X deposition as a function of increasing O_3 and $SnMe_4$ exposure times at 350 and 380 °C respectively and SnO_X TPC as a function of increasing O_3 and $SnBu_3Cl$ exposure at 290 °C. 106

Figure 5.2 ALD window for $SnMe_4$ and O_3 SnO_X ALD and $SnBu_3Cl$ and O_3 SnO_X ALD. Precursor exposure times were 2 s ($SnMe_4$), and 15 s ($SnBu_3Cl$) 107

Figure 5.3 X-ray diffraction of as deposited $SnMe_4/O_3$ ALD film at 380 °C compared to a reference CVD film made from $SnCl_2$ and O_2 precursors.[1] 109

Figure 5.4 Thickness per supercycle (TPSC) and TPC comparison between SnO_2 deposited on itself and ZnO utilizing $SnEt_4$ and varying the precursor pulse time. Atomic % tin reported as a function of increasing $SnEt_4$ exposure on ZnO. 119

Figure 5.5 Composition of ZTO films as a function of Sn pulse ratio.The fits to the experimental data include a simple combustion model and a Brønsted elimination model with a $(f_{Sn}+1)/(f_{Zn}+1)$ ratio of 0.56. 120

Figure 5.6 Mechanism 1. Reaction coordinate and scheme for first ozonolysis of an ethyltin ligand resulting in an ethoxide intermediate. The reaction coordinate follows the conversion of all ethyl ligands to their corresponding ethoxides. 122

Figure 5.7 Mechanism 1. Reaction coordinate and scheme for second ozonolysis resulting in the elimination of acetaldehyde and formation of hydroxide functional group. The reaction coordinate follows the conversion of all ethoxides to their corresponding hydroxides. 123

Figure 5.8 Mechanism 2. Reaction coordinate and scheme for ozone abstraction of ethyl ligand hydrogen resulting in ethene elimination and formation of hydroxide functionality. The reaction coordinate follows the conversion of all ethyl ligands to their corresponding hydroxides. 125

Figure 5.9 Reaction coordinate and scheme for adsorption of $SnEt_4$ on various hydroxide functional groups. 127

Figure 5.10 Computed activation energy as a function of hydroxyl acidity for the adsorption of $SnEt_4$ on hydroxyl sites. 129

LIST OF TABLES

Table 2.1 Characterization techniques used for analyzing ALD films 24

Table 2.2 Equations for measuring and fitting films by ellipsometry 26

Table 3.1 X-ray crystal data for zinc tetramers analogous to the DFT model compound $[(HO)_7Zn_4(Et)]$. 52

Table 3.2 Measured and calculated IR absorptions assigned to the complex/cage pair formed in an Ar matrix from the reaction of Me_2Zn and O_3. The first column lists the experimental values[2] and the second column lists the predicted absorptions for $MeZnO_3Me$ calculated using the M06-L DFT functional and the 6-31+G(d,p) basis set. 57

Table 3.3 Bond lengths and angles for MeZnOMe as calculated by Varma and Ault with B3LYP[2] and compared to M06-L calculations used in this study. 58

Table 3.4 Measured and calculated IR absorptions assigned to matrix isolated MeZnOMe. 59

Table 4.1 Bond length and density for empirical and computed tetrahedral IV-VI materials. 90

Table 4.2 2-Theta values of 38% Sn/(Sn+Zn) correlated to various material phases of zinc oxide, tin oxide and zinc silicate. 94

Table 5.1 Opto-electronic properties of SnO_X films deposited using $SnMe_4$ and $SnBu_3Cl$ precursors with ozone. 110

Table 5.2 Low temperature deposition of SnO_2 and ZTO. 115

LIST OF SCHEMES

Scheme 3.1	Models of an ethyl group bound to a ZnO surface.	47
Scheme 3.3	Reaction of ozone with dimethylzinc in an argon matrix	51

CHAPTER ONE

Background

Atomic Layer Deposition of Mixed Metal Oxides as Transparent Conducting Oxides for Tunnel Junction Applications

The motivation behind atomic layer deposition (ALD) of tin oxide and zinc tin oxide materials was to develop transparent conducting oxides for tunnel junction devices in tandem CIGS (Copper Indium Gallium Selenide) solar cells. To achieve the necessary film properties by ALD, computational chemistry was employed to effectively model the reaction chemistry between alkyl metal precursors, predict deposition byproducts, and identify possible temperature regions for ALD processing. In this chapter, the background related to tunnel junction devices, the ALD of tin oxide and zinc tin oxide, as well as mechanistic theory of ALD are discussed.

1.1 Tunnel junction devices for multi-junction photovoltaic applications

In a multi-junction solar cell where two absorbers are used to increase the overall efficiency of the cell, a tunnel junction device is required to electronically connect the cells with a low resistance interface (Figure 1.1). Each cell is a NP junction where light is absorbed in the p-type material creating an electron hole pair. The electron migrates to the top contact of the n-type material and the hole migrates to the bottom contact of the p-type material. Without the tunnel junction in place, the overall stack is NPNP which would halt the flow of carriers across the reverse PN junction between absorbers.

The tunnel junction rectifies this situation by providing a material interface allowing for electron carriers to efficiently migrate from the p-type absorber of the bottom cell to the n-type top contact of the top cell and also allow for the migration of the hole in the p-type material of the top cell to the bottom contact of the bottom cell. Tunnel

junctions are devices that are fabricated from n-type and p-type materials that allow for valence-to-conduction band carrier transport at the p/n-type interface.

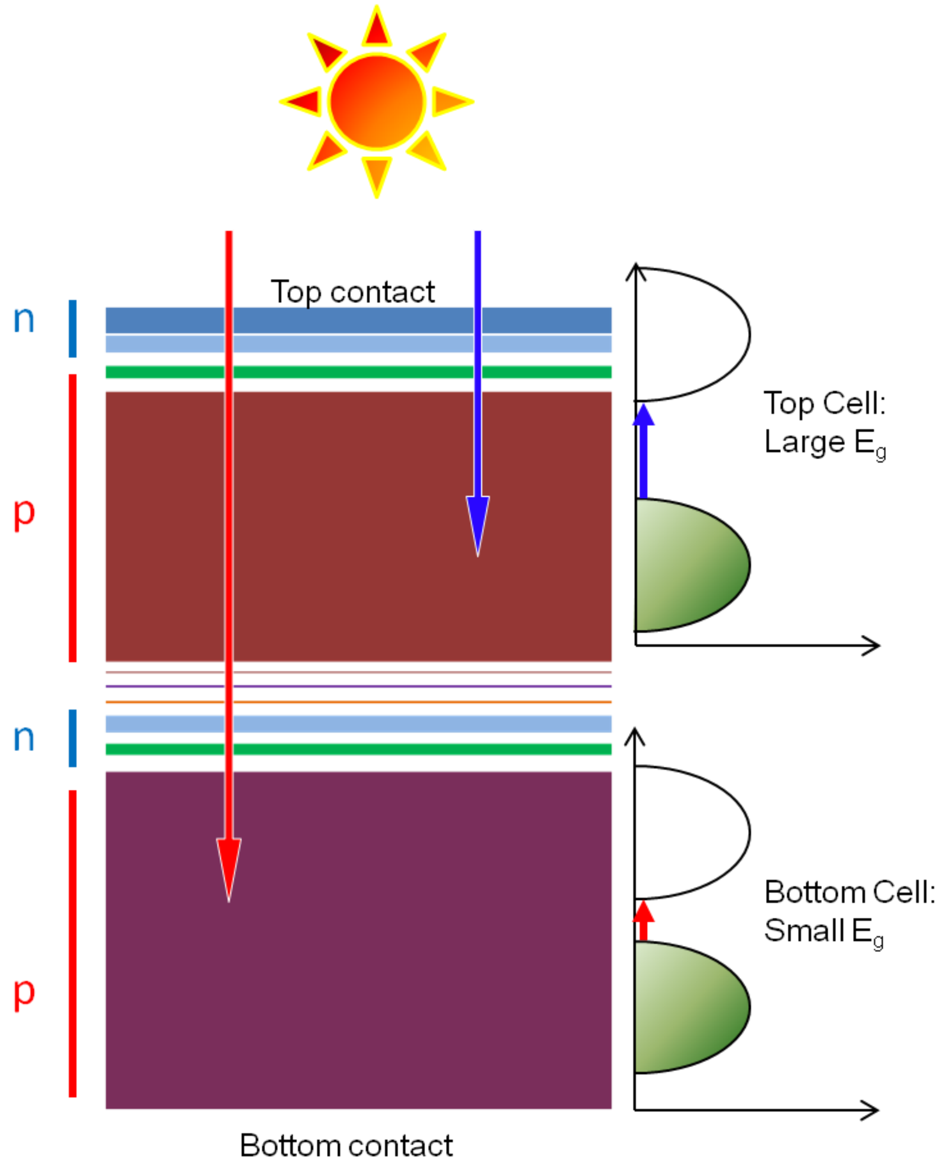

Figure 1.1 Multi-junction solar cell indicating two absorbers with different bandgaps.

The method of carrier transport inside the tunnel junction relies on quantum tunneling where the carrier can transit through a potential energy barrier and appear on the other side even though the carrier lacks the energy to overcome the barrier.[9] In the case of the tunnel junction the potential energy barrier is usually a thin depletion region that exists between the n-type and p-type materials. In order to achieve the tunnel effect, both n-type and p-type materials must be heavily doped and have high carrier concentrations which create a thin depletion region. The application of a tunnel junction to a stacked or multi-junction solar cell results in another requirement that the n-type and p-type materials be sufficiently optically transparent (above 1.9eV for most multijunction solar devices).

A band diagram illustrating the typical IV characteristics of tunnel junctions under reverse and increasing forward bias conditions is shown in (Figure 1.2). When the junction is not under any bias the electrons on both side of the depletion region are at the same energy and there is no net current (1). As the forward bias is increased, the conduction band electrons of the n-type material are raised in energy. A local maximum in current is achieved where the conduction band electrons of the n-type material tunnel into the valance band of the p-type material (2) resulting in valence-to-conduction band carrier transport.

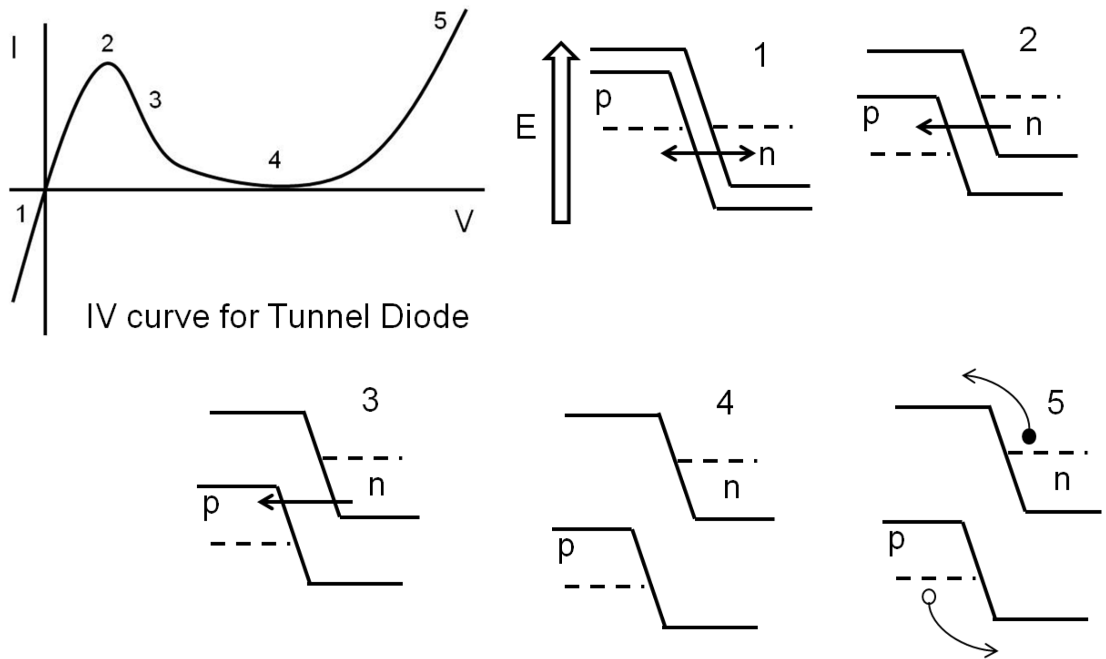

Figure 1.2 Tunnel junction IV profile and band diagram depicting operation of tunnel junction.

Current decreases once the n-type conduction band is raised, aligning to the p-type mid-gap level. This reduces available states to tunnel to in the p-type side, demonstrating negative differential resistance with increased bias in (3). If the bias is increased further, the electrons of the n-type material spill over the barrier from thermionic emission resulting in a significant increase in current from (4) to (5). More importantly for multi-junction solar cell operation under reverse bias, electrons injected in the p-type layer tunnel from the valence band into free states in the n-type conduction band, causing large current flow.

Materials that have been used for the n-type tunnel junction include III-V materials such as Si doped AlInP and InGaP in the InGaP/GaAs tandem cells.[10,11] These materials have carrier concentrations on the order of 1.0×10^{19} carriers cm^{-3}.[11] Possible alternative candidates for tunnel junction n-type materials for CIGS solar cells exist. One such material is zinc tin oxide or ZTO which is a transparent conducting oxide (TCO). Zinc tin oxide is a potential TCO of interest in making the n-type part of a tunnel junction because of its chemical stability, robustness, low surface roughness, and n-type conductivity as well as its optical and electronic properties.[12,13] Carrier concentrations for ZTO films have been reported as high as 1×10^{19} carriers cm^{-3} for sputtered films which are comparable to the AlInP and InGaP materials.[13]

1.2 Introduction to atomic layer deposition

1.2.1 Principles of ALD

Atomic layer deposition is a thin film technique for depositing uniform and highly conformal films over high aspect ratio surfaces.[14,15] The process relies on the self limiting nature of the precursor chemistry used for depositing the materials in a layer by layer fashion.[16] In metal oxide (MO_X) ALD, a typical reaction scheme exists where the precursor of interest (typically an organometallic) is chemisorbed onto a surface substrate with the elimination of one or more ligands. A purge gas is applied to remove residual precursor followed by the introduction of an oxygen source which reacts with the

chemisorbed species to produce the metal oxide. All volatile byproducts of the ALD reaction are removed by a second purge gas cycle.[16] The overall reaction chemistry proceeds in sequential steps resulting in atom by atom growth (Figure 1.3).

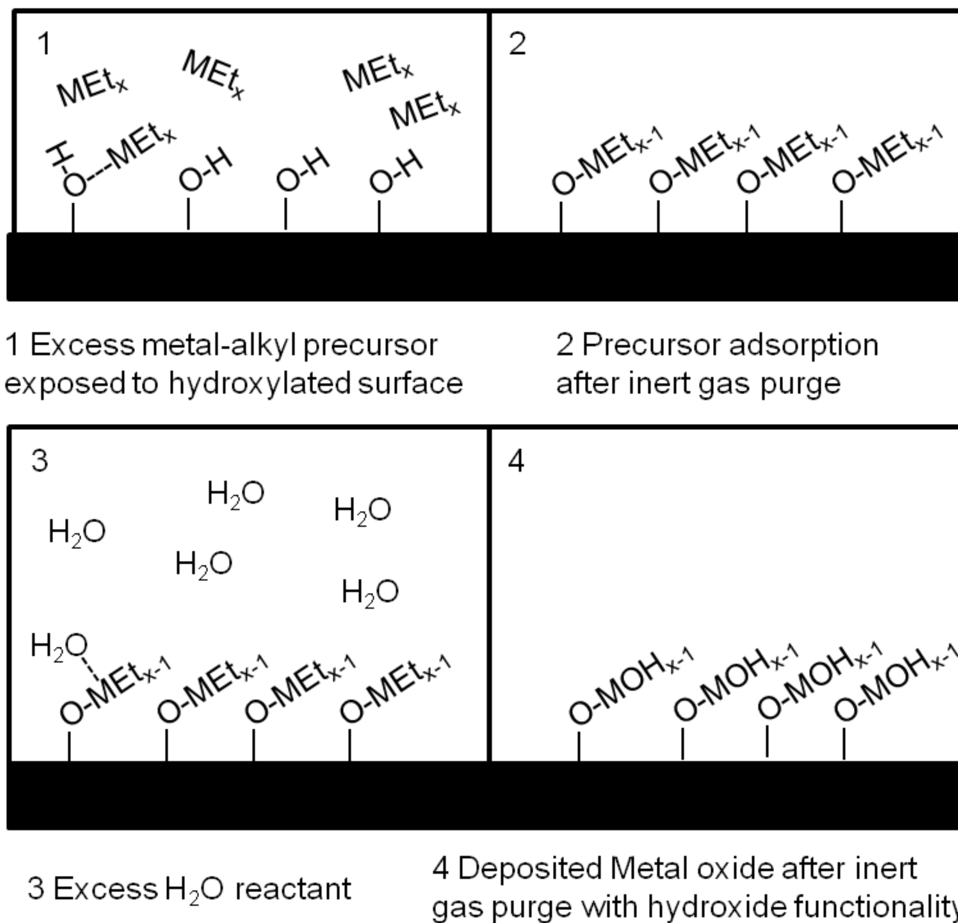

Figure 1.3 Representative ALD of metal-alkyl (MEt_x) with water where the self limiting nature of ALD materials is achieved by sequential reaction of precursor and reactant following inert gas purges.

One of the primary challenges in ALD is the design of precursors. The precursors must be volatile to enter the gas phase as well as thermally stable so as not to decompose resulting in an inhomogeneous growth rate. The precursor surface chemistry is vital to the ALD process in that the precursor must interact strongly with the surface functional groups in order to bind effectively. Hydroxyl functional groups have been reported to be important for MOx ALD.[16-18] The overall reaction chemistry of the precursor with the surface functional groups should ideally have a strong thermodynamic driving force with large negative ΔG values.[16]

1.2.2 ALD precursors for zinc oxide

Zinc oxide has successfully been deposited by ALD using diethylzinc or dimethylzinc with various oxygen sources including water, hydrogen peroxide, and ozone.[19-21] The overall reaction of the alkyl zinc precursors with the surface hydroxyl groups and water has been shown to result in the formation of zinc oxide and ethane (1.1).[22,21]

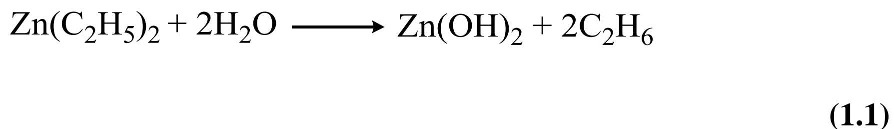

$$Zn(C_2H_5)_2 + 2H_2O \longrightarrow Zn(OH)_2 + 2C_2H_6$$

(1.1)

The overall reaction scheme supports a mechanism where the alkyl zinc adsorbs onto the hydroxyl followed by an elimination of an alkane. Water is then introduced in the gas phase to remove the other alkyl ligand resulting in a surface bound zinc

hydroxide. The reaction can then be repeated with another equivalent of diethylzinc resulting in layered growth of zinc oxide. This mechanism has been proposed for a similar reaction involving trimethyl aluminum with water.[23]

Ozone with diethylzinc has been shown to be an effective oxygen source for depositing zinc oxide films by ALD.[24,20,25] The mechanism involving the reaction of diethylzinc with ozone is more involved than the reaction with water. Experimental evidence as well as computational data support an overall reaction that eliminates acetaldehyde and rehydroxylates the surface for further ALD reactions (1.2).[26]

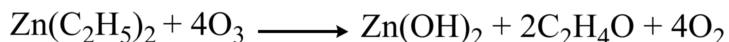

$$Zn(C_2H_5)_2 + 4O_3 \longrightarrow Zn(OH)_2 + 2C_2H_4O + 4O_2 \quad \textbf{(1.2)}$$

Alkylzinc precursors have been shown to be effective ALD precursors with multiple oxygen sources. Typical deposition temperatures for zinc oxide ALD have been shown to be between 50 °C to 300 °C for both water and ozone, with ozone having larger deposition rates at higher temperatures.[27,22] In both deposition chemistry the ALD growth rate was reported to be approximately 0.18 nm/ ALD cycle which is consistent with ALD and less than the theoretical maximum of a monolayer of ZnO in the wurtzite phase oriented about the c-axis.[28]

1.2.3 ALD precursors for SnO_2 tin oxide

Tin oxide has been deposited by ALD utilizing both tetraethyl and tetramethyltin precursors with N_2O_4, tin tetrachloride and H_2O/ H_2O_2, cyclic amide tin derivatives, and tetrakis(dimethylamido)tindimethylaminotin with H_2O_2 (Figure 1.4).[29-32] The ALD temperature windows for the various precursors were shown to be between 50 °C and 430 °C. The cyclic amide N^2,N^3-di-tert-butyl-butane-2,3-diamido-tin(II) ($C_{12}H_{26}N_2Sn$)/H_2O_2 and the tetrakis(dimethylamido)tin(IV)/ H_2O_2 had the lowest reported ALD window starting at 50 °C with a deposition rate of 0.18 nm/cycle and 0.14 nm/cycle, respectively.[33,32]

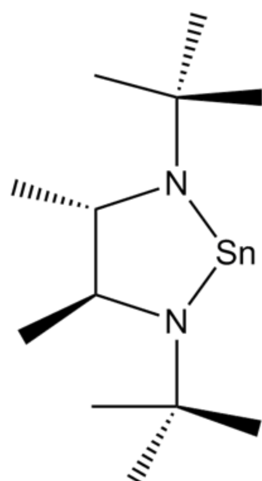

N[2],N[3]-di-tert-butyl-butane-2,3-diamido-tin(II)

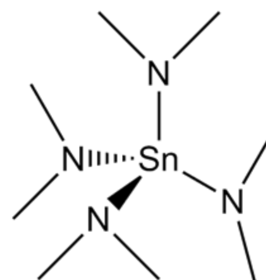

Tetrakis(dimethylamido)tin(IV)

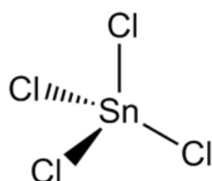

Tin tetrachloride

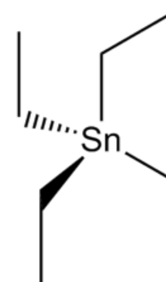

Tetraethyltin

Figure 1.4 Tin precursors for ALD of SnO_X films.

Tin tetrachloride and the tetralkyl tin precursors had the highest reported deposition temperature for the ALD window of the precursors mentioned. Tin tetrachloride had a deposition region between 300 °C and 600 °C for water and 150 °C to 430 °C for hydrogen peroxide. Tetraethyltin had a processing window between 250 and 300°C with the N_2O_4 oxygen source. Deposition rates for the tin tetrachloride ALD

chemistry were shown to be approximately 0.07 nm/ ALD cycle while the tetraethyltin was higher at 0.24 nm/cycle.[31]

All of the tin precursors mentioned are tetravalent molecules with a four coordinate geometry save the cyclic amide which is divalent.[33] It is interesting to note that the lowest processing temperatures for tin oxide ALD are with the amido ligands and highest processing temperatures for the alkyl and halogenated precursors. The ligand effect on processing temperature is complicated as one could expect weaker metal ligand bonds resulting in higher reactivity, however this is not the case with the tin precursors where the tin bond strength increases in the order of $C<Cl\approx N$.[34, 35] If this were the case, one could expect the ALD window to be shifted to lower thermal energy with alkyl and halogen ligands to compensate for the weaker ligand to tin bonds, however the opposite is observed.

One of the benefits of the alkyltin precursors, even though they have higher temperature ALD windows than the amido derivatives, are that they are highly volatile, stable, non-corrosive, and commercially available.[16,32] The alkyl tin precursors are toxic and must be handled carefully, but they remain a valuable precursor option when depositing tin oxide films.

1.2.4 Depositing mixed metal oxides by ALD

Atomic layer deposition can be used to deposit mixed metal oxides or doped metal oxides. Since ALD deposits materials in a sequential fashion, the deposition

sequence can be modified to deposit alternating layers of different metal oxides. This layered approach utilizes supercycles where each supercycle comprises n M^1O_X and m M^2O_X cycles where M^1 and M^2 represents the metal in the different oxides (Figure 1.5). This approach has been used successfully in depositing nanolaminates such as aluminum zinc oxide.[36]

The deposition of materials using sequential ALD can encounter significant barriers to film growth where a one to one ratio of sequences in the supercycle does not result in the sum of the individual deposition rates of each material. This phenomena can be observed in both the total film thickness, as well as the elemental composition.[36] In AZO films, a suppression of zinc oxide growth rate has been observed, whereas nanolaminates of alumina silicates and hafnium oxide silicates have shown a marked 3200% increase in deposition rate of silica from tris(tert-butoxy)silanol.[37, 38]

The suppression of one precursor by another does not always occur with some materials such as zinc tin oxide deposited by diethylzinc and a cyclic amide of Sn(II).[39] In the sequential deposition mode, the nanolaminate ZTO material showed little change in overall experimental film deposition rate and overall film density compared to what was expected from the sum of the individual metal oxides.[39]

A second option available for depositing mixed metal oxides by ALD is to co-inject both MO_X precursors simultaneously. The precursors will compete for surface functional groups which should result in a more mixed metal oxide. This method has effectively been used to introduce phosphorous and aluminum dopants in zinc oxide .[25,28] The film composition is usually more homogenous with this method, however this

method can be more challenging as the film stoichiometry is controlled by the concentration of the individual precursors and competition for active hydroxyl sites.[25]

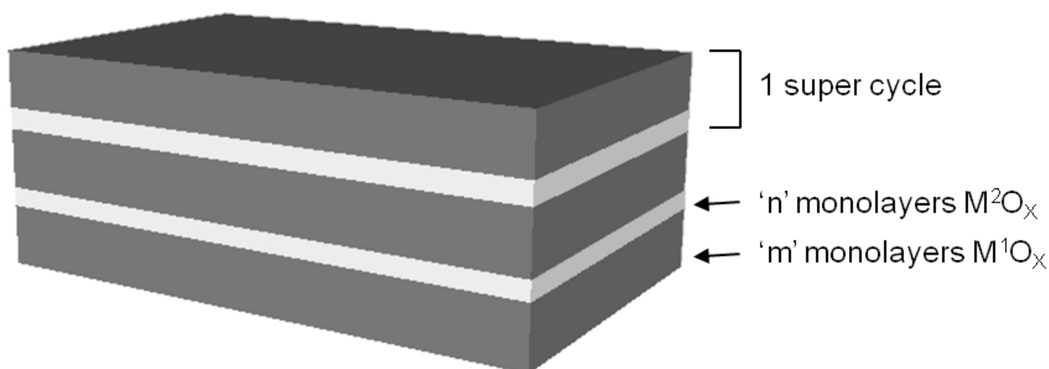

Figure 1.5 Nanolaminate film from sequential ALD process

1.3 Theoretical ALD mechanisms

Atomic layer deposition has been researched from a theoretical perspective to gain fundamental knowledge of the ALD reaction chemistry. Computational chemistry can be used for precursor design, understanding adsorption characteristics, and predicting byproducts. This level of theory increases our understanding of and can play a key role designing new ALD precursor chemistry.

The reactivity of water with precursors such as trimethylaluminum and aluminum trichloride has been studied computationally as well as experimentally with the B3LYP

functional.[23, 40, 41] The reaction of water with either trimethylaluminum or aluminum trichloride results in the elimination of methane or HCl and a hydroxyl terminated aluminum. From the computations the energy barrier for the methane elimination versus the HCl elimination indicates that the methane ligand elimination is 26 kcal/mol more favorable. The reduced energy barrier for trimethylaluminum indicates that aluminum oxide can deposit at lower temperatures than the aluminum trichloride, an observation which has been observed in deposition chemistry.[40]

Other precursor chemistry such as the interaction of ozone with TMA for producing aluminum oxide films has recently been modeled using DFT using gas phase singlet oxygen atoms.[42] The computations suggest that an oxygen atom dissociates from ozone and inserts itself in either a carbon hydrogen bond forming an alcohol ($Al-CH_2OH$) or between the metal carbon bond forming a methoxide ($Al-OCH_3$).[42, 43]

The rehydroxylation of the surface, after atomic oxygen exposure to the aluminum ligands, can proceed through two mechanisms. In the alcohol case, ethene is predicted to eliminate from two adjacent $Al-CH_2OH$ groups leaving behind the hydroxylated surface.[42] In the methoxide case, two adjacent methoxides ($Al-OCH_3$) have simultaneous hydrogen transfers to the oxygen and eliminating ethane.

In ZnO ALD with diethylzinc, ozone is proposed to insert between the metal-ligand bond resulting in a trioxide that rapidly decays to form a zinc ethoxide. A second equivalent of ozone is required to react with the ethoxide eliminating acetaldehyde and forming a hydroxide.[26] In either case the actual mechanism of ozone interaction with alkyl metal precursors is not as well understood as the interaction with water.

CHAPTER TWO

Experimental Procedures and Characterization Techniques

The discussion in this chapter pertains to the treatment of the substrates, the precursors, and the ALD reactor for depositing the metal oxide films. Characterization techniques for determining film properties, as well as theoretical resources will also be discussed.

2.1 ALD precursors and substrates

2.1.1 Glass and silicon substrate treatments

Both soda lime glass (SLG) and silicon substrates Si (100) were used for all depositions. The SLG substrates were cut from slides and measured approximately 1cm x 2cm. Silicon substrates were also broken into postage stamp substrates approximately 1cm x 1cm. The glass substrates were rinsed with ethanol and subsequently dried under a nitrogen stream. Silicon substrates were placed in a piranha solution consisting of a 70:30 solution of sulfuric acid with 30% hydrogen peroxide for 1-2 hours after which they were rinsed in DI H_2O and soaked in 30% HF for approximately 10 minutes followed by a final DI H_2O rinse. The substrates were then placed on a glass slide using furnace tape to adhere the substrates and immediately inserted into the hot wall ALD reactor which was subsequently evacuated.

2.1.2 Precursors, vessels, and handling

All tin oxide films and zinc tin oxide films (ZTO) were deposited using alkyl tin derivatives as the tin source and diethylzinc as the zinc source. Zinc tin oxide materials utilized for the tunnel junction devices were exclusively deposited using tetraethyltin $Sn(C_2H_5)_4$, ozone O_3, and diethylzinc $Zn(C_2H_5)_2$ precursors. Tetramethyltin $Sn(CH_3)_4$, tri-n-butyltin chloride $Sn(C_4H_9)_3Cl$, and tri-n-butyltin hydride $Sn(C_4H_9)_3H$ were used as alternative tin sources to understand the tin precursor ALD chemistry. All tin and zinc precursors were commercially available and purchased from Sigma Aldrich.

Stainless steel precursor vessels were used for all chemical precursors as a safety precaution. The precursor vessels had approximately 50 cm^3 of headspace and were connected to a manual bellows valve using vcr™ fittings (Figure 2.1). The precursors had sufficient volatility such that a carrier gas was not needed to introduce the precursor into the reactor chamber.

Care was maintained to avoid any rout of exposure to the alkytin precursors which have considerable toxicity.[44] All transfers of alkyl tin compounds to the precursor vessels were carried out in a fume hood. For safety reasons not more than 5ml of organotin precursor were loaded into the precursor vessel at a time. After a precursor transfer, the manual bellows valve was closed and the vessel was immediately attached to the ALD reactor.

Diethylzinc is a pyrophoric liquid that can ignite on contact with air or water. The zinc precursor was loaded into the precursor vessel with the aid of a glovebox which

provided an inert nitrogen atmosphere. Additionally, only 5-10 ml of diethylzinc was transferred to the precursor vessels for fire safety reasons.

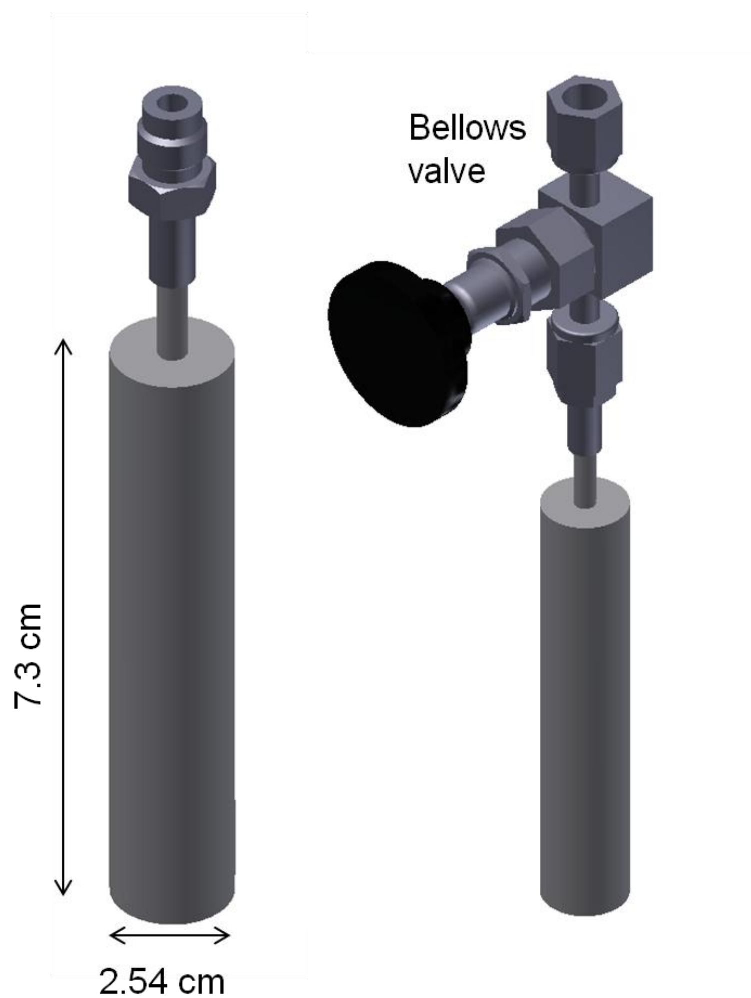

Figure 2.1 Stainless steel precursor vessels for ALD reactor

Ozone was produced by an oxygen-supplied ozone generator producing 2-3% O_3 in oxygen. The ozone was generated in a fume hood and supplied to the ALD reactor using inert PTFE tubing.

2.2 Deposition Reactor

All ALD deposited films were deposited in a custom built hot wall reactor (Figure 2.2).

The precursors, as well as inert nitrogen purge pulse, were introduced into the ALD reactor through a set of computer controlled pneumatic valves. Depending on the volatility of the precursor, either cold baths utilizing a cryo-cool chiller or hot baths utilizing mineral oil and a variac controlled heater were utilized to alter the vapor pressure of the precursors. In all cases an alcohol thermometer was used to measure and record the bath temperature. All lines leading from the precursor vessel could be heated using heating tape to prevent condensation of low volatility precursors.

The region of film deposition occurs in the hot zone of the ALD reactor which comprises a one inch quartz tube inside a Lindberg tube furnace. The precursors flow into the quartz tube and deposit on the silicon or SLG substrates in the hot zone. The flow through the reactor is provided by a Leybold Trivac D25 mechanical vacuum pump which exhausts the reactor effluent to the lab's air handling system.

Substrates were loaded and unloaded by a bolted steel flange on the effluent side of the tube furnace. The flange was face sealed via a rubber o-ring to the quartz tube furnace, which provided an adequate seal for vacuum pressures in the low mtorr. The base pressure of the reactor was 20 mtorr but during deposition, reactor pressures were in the 1 torr range.

The reactor was also equipped with a thermocouple pressure gauge; however accurate in-situ pressure measurements were not reliable as the gauge would experience deposition from the ALD precursors resulting in false higher pressure readings. A new gauge could initially be used to accurately measure precursor vapor pressures for determining quantitative precursor dosage.

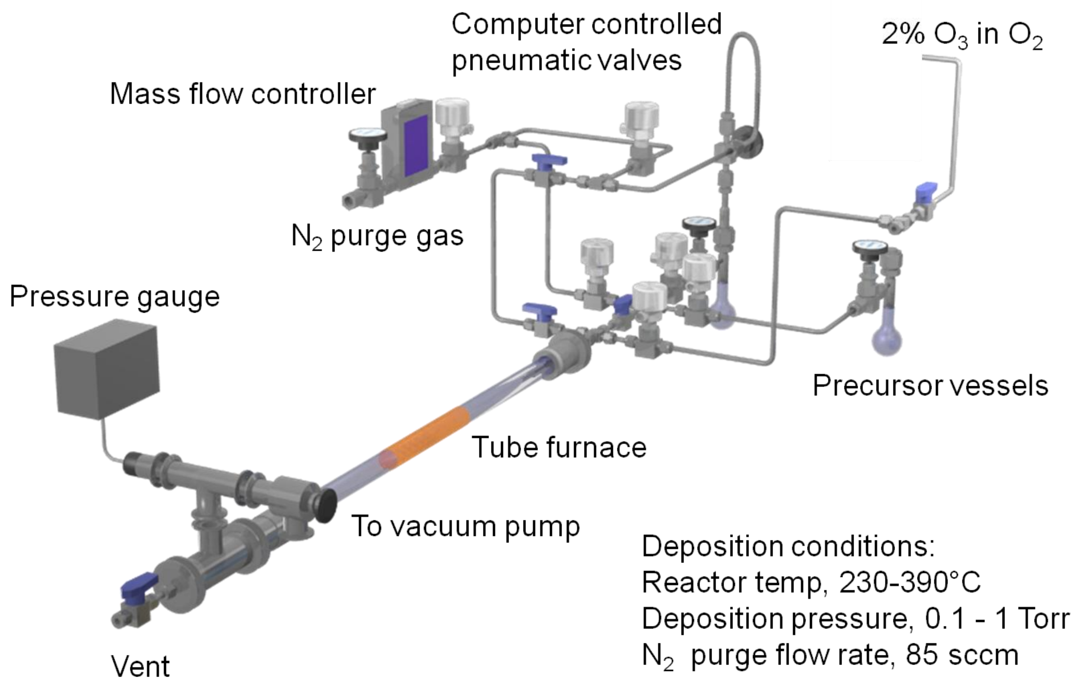

Figure 2.2 ALD reactor schematic showing the design of the deposition tool

High purity nitrogen (99.999%) was used as a purge gas to separate the pulses of precursor and the oxygen source. The flow rate of the nitrogen was maintained by a UFC 1660 mass flow controller with a URS-100 control box and kept at 80 sccm for all

depositions. Industrial grade oxygen was supplied to the ozone generator which produced a flow of 5 liters/minute of 3% O_3 in oxygen at atmospheric pressure. The flow of O_3 was fed into the reactor through a T joint connected to manual bellows valve and computer controlled pneumatic valve. During normal operation the flow of ozone was continually vented to the air handling system. Ozone could be introduced into the reactor by opening the computer controlled pneumatic valve relying on the bellows valve to throttle the amount of O_3 introduced to approximately 100 sccm based on the reactor pressure of 1 torr during the ozone pulse.

2.3 Characterization and theoretical techniques for tin and zinc tin oxide films

In order to understand the properties of the tin oxide and ZTO films, characterization techniques need to be employed to quantify film thickness, composition, and structure as well as film properties pertaining to their opto-electronic behavior.

Various techniques were employed to study the films and are summarized in the Table 2.1.

Table 2.1 Characterization techniques used for analyzing ALD films

Technique	Characterized Property	Special Notes
Spectroscopic Ellipsometry	Film thickness, index of refraction	Requires a computer model for data analysis
X-ray diffraction	Film structure, crystallinity, preferred orientation	
Rutherford backscattering spectrometry	Film elemental analysis, film density	Requires a computer model for density analysis
Atomic force microscopy	Film topology including surface roughness	
Electron microscopy	Cross sectional film thickness, elemental analysis, surface imaging	Time intensive technique requiring sample prep
Hall effect measurements	Film carrier concentration and carrier mobility	
Density functional theory	Predict most physical observables of chemicals and reactions including ▪ Energy (ΔG, ΔH,$\Delta G^{\ddagger}$) ▪ IR (vibrational spectra) ▪ NMR	Computational, computer intensive

2.3.1 Spectroscopic ellispsometry

Spectroscopic ellipsometry utilizes UV-visible light to non-destructively analyze a transparent film on a reflective substrate. During a typical characterization, linearly polarized light of a specific wavelength is reflected off a sample at an angle to a detector. The wavelength of light can be scanned from the UV to the near IR region during the characterization.

Light is an electromagnetic wave where the electric field is composed of two oscillating sinusoidal waves. The sinusoidal electric field vectors have two components, one perpendicular to the plane ε_s and one parallel to the plane ε_p. In linearly polarized monochromatic light, the electric fields of the light waves are all aligned in one direction giving an incident ε_{is} and ε_{ip} polarization. Upon reflection at an angle, the light wave experiences a phase shift Δ in the electric field component of the electromagnetic wave and an amplitude change Ψ resulting in a ε_{rs} and ε_{rp} polarization. The reflected light has become elliptically polarized and the change in polarization can be detected (Figure 2.3).

Psi and Δ are related to the ratio of reflectance where R_p and R_s come from Fresnel's equations and are dependent on the index of refraction (film and substrate), incident angle, and refracted angle and film thickness.[45]

A Cauchy model can be used to determine film thickness and the index of refraction for films where the value is unknown. All equations must be solved iteratively until a fit is produced and the film thickness can be determined. The basic equations governing ellipsometry are summarized in Table 2.2.

Table 2.2 Equations for measuring and fitting films by ellipsometry

Ellipsometry measurable (Ψ,Δ)	**Cauchy model** ***n*****= index of refraction**	**Thickness (*d*)**
$\tan\Psi \times e^{i\Delta} = \frac{R_P}{R_S} = \frac{\varepsilon_{rp}/\varepsilon_{ip}}{\varepsilon_{rs}/\varepsilon_{is}}$ $\frac{R_P}{R_S} = \frac{\frac{r_{1p} + r_{2p}e^{-i4\pi(\frac{d}{\lambda})N\cos\Phi}}{1 + r_{1p}r_{2p}e^{-i4\pi(\frac{d}{\lambda})N\cos\Phi}}}{\frac{r_{1s}+r_{2s}e^{-i4\pi(\frac{d}{\lambda})N\cos\Phi}}{1 + r_{1s}r_{1s}e^{-i4\pi(\frac{d}{\lambda})N\cos\Phi}}}$	$n(\lambda) = A + \frac{B}{\lambda^2} + \frac{C}{\lambda^4}$	$d = \frac{n_0\lambda}{2n_1\cos\theta}$

Film thicknesses were determined on a J.A. Woollam Co. V-VASE HS-190 spectroscopic ellipsometer. Scans were taken at 60 and 75 degree angles between 300 and 800 nm on ALD deposited silicon substrates. A Cauchy model was used to fit the data and obtain film thicknesses

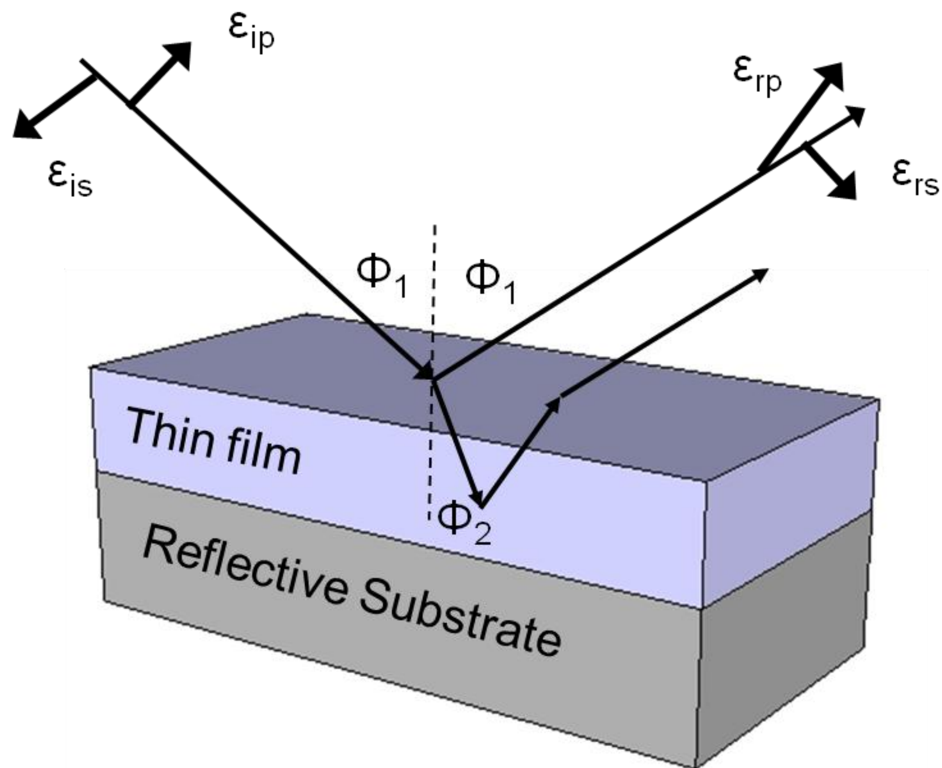

Figure 2.3 Ellipsometry measurement indicating a phase shift and amplitude change in the reflected light versus incident light

2.3.2 X-ray diffraction

X-Ray diffraction is used to determine a materials structure from radiation wavelengths that are close to an atomic bond length (CuKα radiation: 1.54Å).[46] The X-ray enters into a material where it is scattered off the electron clouds of the atoms in the

material. Most of the scattering results in destructive interference of the X-ray beam and no net signal is observed. Depending on the material and the angle, the scattered X-ray waves can add constructively resulting in observed XRD peaks. When XRD peaks are observed, the material being analyzed has long range order and is crystalline in nature. Amorphous materials have no long range order and do not have discrete XRD reflections but are generally characterized by an "amorphous hump" in the pattern.

Crystalline materials possess long range order where the atoms are arranged in plains and the spacing between plains is known as the d-spacing. The d-spacing can be determined from Braggs law, $2d\sin\theta=n\lambda$, where d is the distance between atomic planes, θ is the scattering angle, and λ is the x-ray wavelength. Bragg's law uses a geometric model where the two reflected X-ray beams (I&II) can only add constructively if they are in the same phase. Since X-ray II travels farther than X-ray I, a pattern is only observed when the distance traveled by X-ray II is an integer of the X-ray wavelength. In this case distance 1-2-3 = $n\lambda$. In most cases, the distance between the atom planes is of interest in characterizing the material and if the incident angle of the X-ray beam is known, distance 1-2-3 can be rewritten as $2d\sin\theta$ thereby deriving Bragg's law(Figure 2.4).[47] Based on the measured value of 2θ and peak intensity, a match can be found between the material and a powder diffraction file resulting in identification of the material.[45]

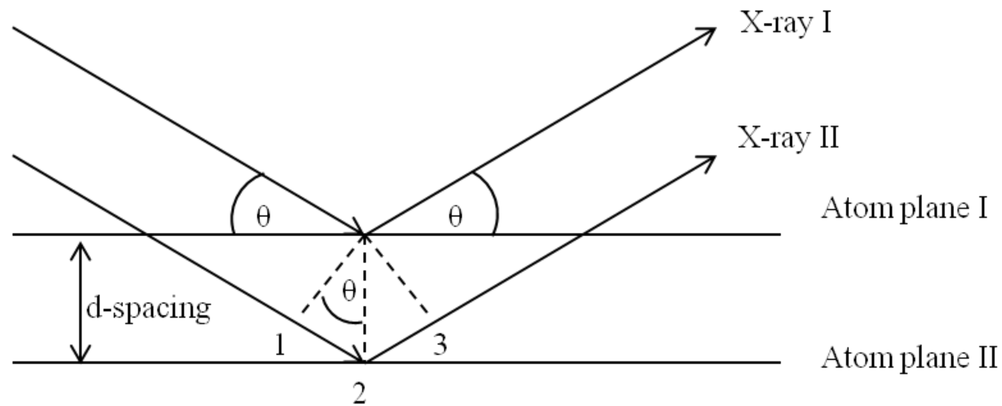

Figure 2.4 Gemetric model for determining d-spacing in Bragg's law

2.3.3 Rutherford backscattering spectrometry

Elemental analysis (EA) of thin films is a basic requirement for determining the composition of the material being deposited. Rutherford backscattering spectrometry (RBS) is a quantitative EA technique that does not require any reference standards of the materials being deposited. Rutherford backscatter spectrometry relies on elastic collisions between an accelerated ion (typically He^+) and the target (sample) to determine the material composition.[45]

A typical RBS instrument requires an ion source to generate the He^+ beam, a voltage differential to accelerate the ions which imparts a set amount of kinetic energy (k_e)to the ion where k_e is equal to the ion charge multiplied by the accelerating voltage, and a detector which measures the energy of the backscattered He^+ ions. In a simplified

one dimensional case, the mass of the target atom can be determined by observing that for an elastic collision to occur, both momentum (P) and energy (E) are conserved.

In a simple 1D collision, the mass of the target atom can be determined by manipulating the P and E equations. In the 1D case the two unknowns are m_2 and v_4, however v_4 can be solved for in terms of m_2 from the momentum equation and substituted into the energy equation. From the initial conditions, both m_1 and v_1 are known from the k_e of the He^+ ions. The detector measures the backscattered energy which gives the v_3 term and allows for the target mass (m_2) to be determined (Figure 2.5).

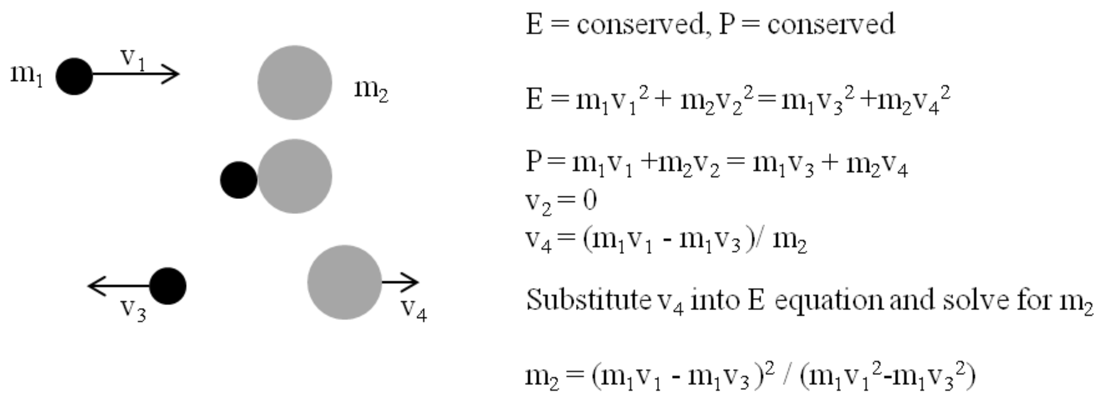

Figure 2.5 Physics behind 1d elastic collisions which allow for the target mass to be determined from conservation of energy and momentum

In the non-idealized case, the He^+ ions backscatter off the nucleus of the target sample at an angle. The change in energy of the backscattered He^+ ion is measured

$E=kE_0$, where k is the kinematical factor which is a value dependant on the scattering angle θ, the mass of He^+ (m_1), and target atom (m_2).[45] The energy from the ion beam E_0 and backscattered beam E are known from the previous discussion of the 1 D case.

$$k = \left(\frac{m1 \cos\theta \pm \sqrt{m_2^2 - m_1^2 \sin^2\theta}}{m1 + m2} \right)^2 \tag{2.1}$$

Based on the difference in energy of the scattered He^+ ion, the mass of the target atom can be determined resulting in elemental analysis. Complications can arise as the material in the film becomes thicker and the He^+ ions impact sample atoms on the way back to the detector. These other impacts result in a distribution of backscattered He^+ energies which causes peak broadening in the experimental spectrum.

The relative concentrations of elements within the film can be determined by integrating the peaks corresponding to the elements of interest and adjusting for the difference in atom cross-section. Larger atoms have a higher probability of scattering a He^+ ion than a smaller atom and the sensitivity is proportional to the square of the atomic number (Z^2).[45] For example, the relative concentrations of Sn to O in a tin oxide film can be determined by integrating the Sn and O signals and normalizing by their respective atomic numbers. In this case the signal for tin is enhanced by a factor of 40 over oxygen as a result of its larger cross-section.

$$\frac{C_{Sn}}{C_O} = \frac{\int Sn/Z_{Sn}{}^2}{\int O/Z_O{}^2} \tag{2.2}$$

Modeling software also exists for determining the elemental composition of the films as well as film density (for films with known thickness). Useful programs for modeling thin films include Quark, SIMNRA, and RUMP.

2.3.4 Atomic force microscopy (AFM)

Atomic force microscopy is a surface technique usually used to obtain topographical information such as film roughness and step heights. In thin film processes, film roughness can be important for determining the mechanism of growth by identifying the nucleation events which can lead to large island formations (rough films) or ALD type uniform nucleation which leads to smooth films. Step heights can also be used as a physical method for determining film thickness.

The AFM instrument comprises a piezo-electric stage that the sample mounts to, and a finely tipped probe that is rastered across the surface of the film. The probe is attached to a cantilever which is governed by Hook's law. When the probe moves in the z direction, from changes in the film topography, the cantilever is deflected. The change in deflection is measured by a laser which reflects off the cantilever and gets detected by a photo-diode. Based on the amount of deflection, the z-height of the stage can be moved

by applying voltage to the piezo-electric stage. The movement of the piezo-electric stage prevents cantilever damage and maintains a constant tip to film distance (Figure 2.6).[48]

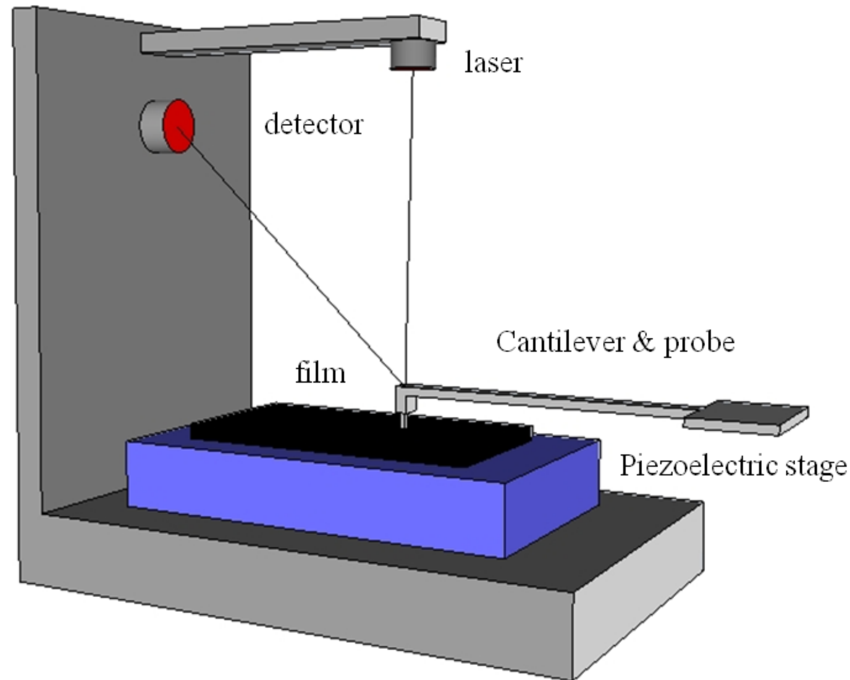

Figure 2.6 Schematic of an AFM device indicating key components for measuring film roughness or step heights

The fundamental principles that govern AFM operation do originate from Hook's law for several reasons. The cantilever spring should have a force constant k(c) that is less than the force constant that exists between atoms K(a). If k(c) were larger than K(a), displacement of surface atoms would occur during topographical imaging.[45] The required k(c) for AFM can be approximated by determining K(a) using the harmonic

oscillator equation where m is the atom mass of the material and ν is the vibrational frequency.

$$2\pi\nu = \left(\frac{K(a)}{m}\right)^{1/2}$$

(2.3)

Once the K(a) for the material is known, a cantilever with k(c)<K(a) can be designed based on classical mechanics, where the deflection of a cantilever with defined length (*l*) and width (*w*) can be determined from the following equation where Y is Young's modulus and *t* is thickness.

$$k(c) = \frac{Ywt^3}{4l^3}$$

(2.4)

From the k(c) equation, it is possible to make k(c) small by increasing *l* relative to *w* and *t*, resulting in long, thin cantilevers for minimizing displacement of surface atoms.[45]

2.3.5 Electron microscopy

Electron microscopy has similarities to AFM in that it is used to generate topographical images of samples. Unlike AFM, scanning and transmission electron microscopy (SEM &TEM) can also be used to obtain elemental analysis on samples from

X-rays generated by the interaction of the electron beam with the sample. In basic operation electron beams are focused through magnetic lenses where they reflect off the sample's surface and are detected giving an image.

Electron beams, depending on their acceleration voltage, have much smaller wavelengths than visible light. In general, objects to be imaged need to be larger than the probing wavelength. The wavelength (λ) of the electron beam can be determined from the de Broglie equation where h is plank's constant and m and v are the respective mass and velocity of the beam.[49]

$$\lambda = \frac{h}{mv} \tag{2.5}$$

The velocity of the electron can be determined from the charge of the electron (e) multiplied by the accelerating voltage (V) and set equal to the kinetic energy of the electron where m_e is the electron mass. If the accelerating voltage is large, relativistic corrections have to be applied to obtain the correct electron velocity.

$$eV = \frac{1}{2} m_e v^2 \tag{2.6}$$

Under typical acceleration voltages of 10kV, the electron wavelength is approximately 12 pm or an order of magnitude smaller than Cu Kα X-ray radiation. The

wavelength of the electron beam is comparable to the atomic radii of most elements potentially allowing for imaging of individual atoms.

Focusing the electron beam requires the use of a magnetic lens which can bend the beam. The lens works by applying a magnetic field (B) to the moving charged electrons. In an applied B field a charged particle (q) in motion (v) will experience a force perpendicular to the field. The perpendicular force is known as the Lorentz force (L_f) which can be used to focus the electron beam.

$$L_f = qv \times B \tag{2.7}$$

In SEM, the electron beam interacts with the sample and the beam penetrates up to approximately one micron. As the electrons escape the interaction volume, they are classified into backscattered electrons and secondary electrons. The secondary electrons are emitted from the near surface and possess relatively low energy. The secondary electrons are captured by a scintillator/photomultiplier detector and are used primarily to give images of the materials surface. Backscattered electrons, in comparison have significantly more energy and are usually not used for topographical imaging, however, because the electrons are scattered elastically, they can provide Z contrast within the sample with heavier atoms appearing brighter.

In addition to imaging, the SEM can produce elemental analysis data from X-rays generated by the interaction of the electron beam with the sample. The characterization technique is known as X-ray energy dispersive analysis (EDX). If the electron beam

possesses sufficient energy, a core electron of an atom in the sample can be ejected creating a temporary ion. An electron in a higher orbital relaxes to fill the vacant orbital resulting in the emission of an X-ray.

The X-ray emission energy is usually specific to the atom resulting in elemental characterization. In some cases, certain elements can have overlap in the EDX spectrum which could result in a misleading analysis. For quantitative elemental analysis with EDX, standards should be used for calibration.

2.3.6 Hall effect measurements

The electrical properties of films can be characterized through the utilizing the Hall effect with the Van der Pauw method.[50] The Hall effect can be used to determine a films electrical conductivity by measuring the total number of carriers (electrons or holes) in the film, as well as the carrier mobility (ability to move with an applied electric field).

To determine the number of carriers in a film, an electrical current is passed through the length of the film. As the electrons flow through the film, an applied magnetic field (B) causes a Lorentz force resulting in electrons drifting to one side of the film, and the holes to the opposite side of the film (Figure 2.7). The separation of charge in the film creates an electric field which can be measured as a voltage (V_H) and is equal to the product of the electric current (I) and the magnetic field (B) divided by the number of carriers (n), film thickness (t) and the fundamental particle charge (e).[50]

$$V_H = -\frac{IB}{nte}$$

(2.8)

If the films conductivity (σ) is known from a 4-point probe measurement or IV profile, the carrier mobility (μ_e) can be determined.

$$\sigma = ne\mu_e$$

(2.9)

Typically film mobility can be improved by increasing the film's crystallinity, which allows for easier charge migration through the film by avoiding grain boundaries. When film crystallinity is improved, a decrease in carrier concentrations is also usually observed as the film contains fewer atom defects which are responsible for carrier generation.

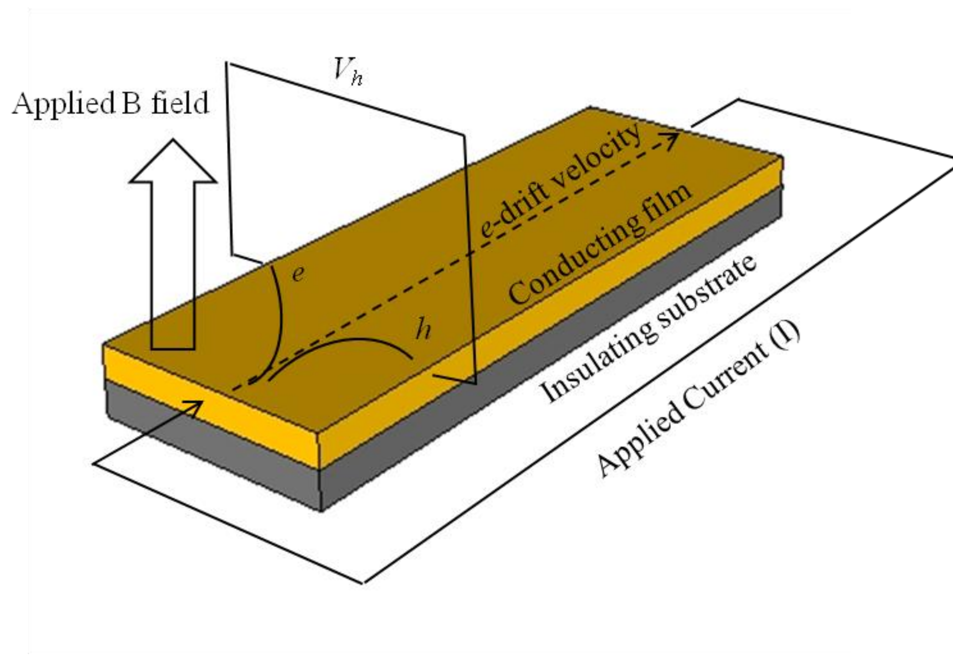

Figure 2.7 Hall effect measurement illustrating the movement of carriers (*e*&*h*) with respect to an applied magnetic field and current

2.3.7 Quantum mechanical methods for computational chemistry

Computational chemistry covers a wide field of techniques, but for ALD purposes, the two most commonly used methods are density functional theory DFT and force field methods. Density functional theory is extremely useful in predicting the activation energy barriers for transition state structures as well as spectroscopic information which in turn allow for mechanistic insight and kinetic information.[23, 51-53] Force field techniques are useful for surveying conformational space on large structures

and can be used to geometrically relax surfaces of ALD materials providing information related to film density and surface hydroxyl coverage.[54]

Density functional theory is computationally efficient compared to other *ab initio* methods (Hartree Fock theory (HF) and Møller Plesset 2nd order perturbation theory (MP2)) and scales as the number of basis functions raised to the third power or N^3.[55]

The foundation of *ab-initio* methods begins with the Schrödinger equation where the energy of a one electron system could be determined by the Hamiltonian operator (*H*) operating on a wave function (Ψ) equation (2.10). Unfortunately the Schrödinger equation cannot be solved for a poly electron system. This limitation resulted in the formation of HF theory which uses a mean field approximation to calculate the electron-electron repulsion term.

The basic principle behind DFT is to reformulate the quantum mechanical formalism to utilize a physical observable (electron density) instead of the intractable wave function Ψ.

$$H\Psi = E\Psi \tag{2.10}$$

The concept of using electron density in place of a wave function can best be understood by looking at the Hamiltonian operator for a polyatomic system. The quantum mechanical operator for energy, the Hamiltonian (*H*) generally comprises at least five energy terms, a kinetic energy term for the electrons and the nuclei, the

columbic attraction between the electrons and nuclei, and the inter nuclear and inter electronic repulsion equation (2.11).[55]

$$H = -\sum_{i}\frac{\hbar^2}{2m_e}\nabla_i^2 - \sum_{k}\frac{\hbar^2}{2m_k}\nabla_k^2 - \sum_{i}\sum_{k}\frac{e^2Z_k}{r_{ik}} + \sum_{i<j}\frac{e^2}{r_{ij}} + \sum_{k<l}\frac{e^2Z_kZ_l}{r_{kl}}$$

(2.11)

From the Hamiltonian equation (2.11), where ħ is Planck's constant, ∇ is the Laplace operator m_e and m_k are the respective masses of the electron and nucleus, Z are atomic numbers, r is the distance between particles, and *i* and *j* are the index of summation for electrons with *k* and *l* representing the summation index for the nuclei, it is apparent that the Hamiltonian depends on the atomic positions of the nuclei as well as the total number of electrons. Because the total number of electrons can be defined as the integral over all space of the electron density, and the positions of the nuclei as point charges can be modeled as centers of electron density maxima, the Hamiltonian can be redefined to depend on electron density. Thus given a known electron density, the redefined Hamiltonian could be used to solve the Schrödinger equation for the energy eigenvalues.[55]

Density functional theory builds off the electron density relationship by defining an energy functional for non-interacting electrons that is dependent on the electron density (ρ(r)) where T_{ni} refers to the non-interacting kinetic energy of the electrons, V_{ne} the electron nuclear interaction, V_{ee} the electron-electron repulsion, ΔT correction of the kinetic energy for interacting electrons, and ΔV_{ee} correction for non-classical electron

interactions (.[55] The Energy functional can be defined using orbital expressions (χ_i) as the electron density can be defined as a Slater-determinantal wave function (2.13) The Hamiltonian can then be expressed as a sum of one-electron operators known as the Kohn-Sham operator (2.14). The energy equation ((2.12) can be minimized by finding the correct X_i, and used with the KS operator, can satisfy the Schrödinger equation for the energy pseudoeigen value (2.15).

$$E[\rho(r)] = T_{ni}[\rho(r)] + V_{ne}[\rho(r)] + V_{ee}[\rho(r)] + \Delta T[\rho(r)] + \Delta V_{ee}[\rho(r)]$$

(2.12)

$$\rho = \sum_{i=1}^{N} \langle X_i | X_i \rangle$$

(2.13)

$$h_i^{KS} = -\frac{1}{2}\nabla_i^2 - \sum_{k}^{nucli} \frac{Z_k}{|r_i - r_k|} + \int \frac{\rho(r^i)}{|r_i - r'|} dr' + V_{xc}$$

(2.14)

$$h_i^{KS} X_i = \varepsilon_i X_i$$

(2.15)

As the name computational chemistry would suggest, significant computer resources are required for optimizing molecular geometries, calculating vibrational

frequencies, and searching for transition state structures with density functional theory. Gaussian© has created a software suite that conveniently allows for parallel processing of computational chemistry problems.[56] In general a DFT functional needs to be chosen that best describes the chemistry.[57] This is important as some functionals have been shown to be more accurate than others at modeling inorganic vs organic molecules. In addition to the functional, a basis set (mathematical description of the orbitals) must also be chosen so that an accurate description of the molecular orbitals can be constructed.

CHAPTER THREE

Atomic Layer Deposition of Zinc Oxide: Understanding the Reactions of Ozone with Diethylzinc

3.1 Introduction

The use of ozone in atomic layer deposition of metal oxide films is becoming increasingly widespread. Ozone has the advantage of being more reactive than water, the most widely used source of oxygen for ALD processes, and this becomes important when using less reactive metal precursors such as β-diketonates. Ozone is also easier to purge from the reactor than water, which can decrease the time needed for each deposition cycle. Unlike the situation with water, however, there is little in the way of fundamental organometallic chemistry known about the reactivity of ozone with metal complexes. This makes it difficult to choose among existing precursor molecules and hampers the design of new precursors. This paper is part of an effort to develop an understanding of ozone reactions in ALD processes.

The direct reaction of dimethyl- and diethylzinc with ozone in the gas phase at atmospheric pressure produces a flame with temperatures above 1300 K that has been studied by Lee and Zare.[58] Their work established that ozone initially reacts at the zinc and inserts an oxygen atom into the Zn-C bond. Formaldehyde was unambiguously identified in the Me_2Zn reaction and evidence of acetaldehyde formation was found in the Et_2Zn case. More recently, Varma and Ault reacted Me_2Zn and O_3 in the gas phase and trapped the products in a solid argon matrix.[2] Using infrared spectroscopy they identified the methoxy methyl zinc complex, Me-Zn-OMe. In addition they observed a precursor that converts to Me-Zn-OMe in the Ar matrix upon UV irradiation.

George and coworkers reported that Me_3Al and O_3 can be used to deposit Al_2O_3 above 300°C.[59] Below this temperature the films were contaminated with carbon that was found to be present as formate and carbonate. Mass spectrometric studies of the effluent from ALD reactions using ozone to produce Ir (or IrO_2), Al_2O_3 and HfO_2 using $Ir(acac)_3$, $AlMe_3$ and $Hf(NMeEt)_4$, respectively, found CO_2 and H_2O as the prominent products during the ozone pulse.[60,61] Finally, Elam and coworkers reported that formaldehyde was observed during the ALD of Ga_2O_3 using Me_3Ga and O_3.[62]

This paper details a combined computational and experimental approach to elucidate the reaction mechanisms of the steps involved in the ALD of ZnO. Quantum chemical density functional calculations were used to investigate the reactions involved in a complete ALD cycle, i.e., both the chemistry involved in the ozone pulse and that involved in the Et_2Zn pulse. The two models used for the surface bound species are shown in (Scheme 3.1), and all reactions for both steps of the ALD cycle have been determined to be thermodynamically favorable. All 298 K activation free energies $\Delta G^{\neq}$ were less that 10 kcal/mol, except that for the elimination of ethane in the Et_2Zn addition step. Experimentally, we focus on identifying the condensable organic products generated during the ozone pulse of the ALD cycle. Modification of an ALD reactor allowed trapping of acetaldehyde, which was identified using NMR spectroscopy.

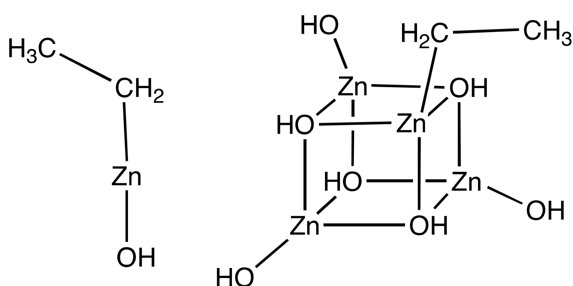

Scheme 3.1 Models of an ethyl group bound to a ZnO surface.

3.2 Experimental

3.2.1 Computational Studies

All structures were fully optimized at the density functional level of theory using the M06-L functional and the 6-31+G(d,p) basis set.[63],[64] Analytic frequency calculations were employed to establish the nature of all stationary points as either minima or transition-state (TS) structures, to compare to available infrared data, and to compute thermal contributions to 298.15 K molecular partition functions employing the ideal-gas (1 atm), rigid-rotator, harmonic-oscillator approximation.[65]

Composite free energies were computed by summing the thermal contributions to free energy computed at the M06-L level with single-point electronic energies computed with the M06 functional and the 6-311+G(2df,p) basis set.[66,64]

All calculations were performed using the Gaussian 09 software suite.[67]

3.2.2 Trapping the Organic Products Formed During ALD

Organic products from the ALD reactor were isolated using a custom built cold trap that was attached to the reactor exhaust. During normal operation, all manual valves on the reactor remained open and precursors were introduced into the reactor through a set of computer controlled pneumatic valves. The reactor exhaust can be directed to the vacuum pump or through a cold trap using valves labeled 1, 2 and 3 in (Figure 3.1). This design allowed collection of the organic products while avoiding the condensation of large amounts of unreacted DEZ.

All atomic layer depositions were performed using literature procedures.[68,69,] Films were deposited at 290°C (reactor temperature), and the ALD sequence and pulse times were DEZ (4 s), N_2/vacuum (15 s), O_3 (6 s) and N_2 (5 s). The longer N_2 purge following the DEZ pulse included a 5 s evacuation, followed by a 5 s N_2 pulse and a final 5 s evacuation.

This additional set of evacuations before and after the N_2 purge served to minimize the acetaldehyde contamination from one deposition to another. Diethylzinc (Aldrich) was introduced into the ALD reactor without a carrier gas from a precursor vessel cooled to -20 °C (ethylene glycol/dry ice slurry). The purge gas was high purity N_2 (99.99%, Air Products). Oxygen (Matheson) was directed through an ozone generator (SR-32, Ozone Solutions) to yield a mixture of 2 - 4% O_3 in O_2. During the ozone pulse, the reactor effluent was directed through a trap cooled to –78°C using an ethanol/dry ice bath. This temperature was chosen to avoid condensing ozone (bp = –112°C) along with

the organic products. During the DEZ and N_2 pulses, the reactor effluent bypassed the trap.

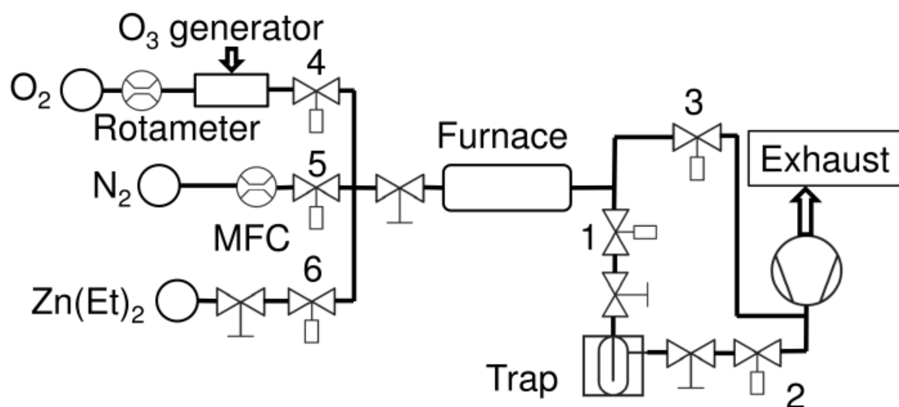

Figure 3.1 ALD reactor schematic showing diethylzinc and ozone precursors with nitrogen purge gas. Square and round valves denote manual and computer controlled valves. Valves 1 and 2 controll the precursor pulse entering into the trap, and valve 3 controls all precursor pulses that bypass the trap

Extraction and characterization of the trapped byproducts following a deposition consisted of closing the manual valves on either side of the trap and removing the trap from reactor line and connecting it to Schlenk line. While the trap contents were still cold and under N_2, the second manual valve was removed and $CDCl_3$ (1 mL) was injected into the trap. The contents were warmed to room temperature and removed to an NMR tube via syringe. The NMR tube contained 1,4-dibromobenzene as an internal

standard. A condensate background of the reactor was also obtained where the above procedure was followed except N_2 replaced the O_3 pulse.

3.3 RESULTS AND DISCUSSION

The reactivity of ozone with organic compounds is well established, and the selective cleavage of alkenes using ozone (to produce aldehydes, ketones, or carboxylic acids depending on the work-up procedure) is widely used in organic synthesis. In contrast, little is known about the reactions of ozone with organometallic compounds, despite the emerging interest in the use of ozone in atomic layer deposition of thin metal oxide films.[24] To improve our understanding of this chemistry, we have undertaken a combined computational and experimental study of the reactions of ozone with organometallics used in ALD processes.

Several reports have appeared describing the ALD of zinc oxide using diethylzinc and ozone as the two reagents.[24, 68, 69] As noted in the Introduction, the reaction of dimethyl- or diethylzinc with ozone in the gas phase has been reported. In high temperature flames (>1300 K), CO_2 and H_2O are formed, but definitive rotational-vibrational spectral evidence was found for the production of formaldehyde ($H_2C{=}O$) from dimethylzinc.[58] By quickly trapping the products from the reaction of dimethylzinc with ozone in a solid argon matrix at 20K, Varma and Ault identified MeZnOMe in which an oxygen atom was inserted into the zinc-carbon bond and observed vibrational spectroscopic changes consistent with the steps shown in (Scheme 3.2).[2]

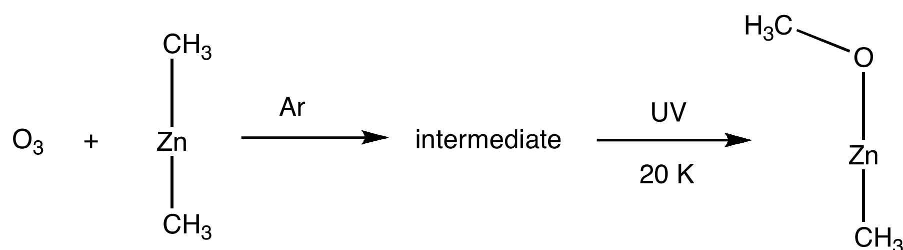

Scheme 3.2 Reaction of ozone with dimethylzinc in an argon matrix

3.3.1 Design of Model Systems and Comparison to Known Structures

Atomic layer deposition involves two reaction steps in which the substrate surface is sequentially exposed to the two reactants.[70] The reactant doses are separated by time and an inert gas purge step. In our previously reported studies involving the deposition of n- or p-doped ZnO using ozone as the oxygen source, the ALD process began with a five-second dose of DEZ. This was followed with a five-second N_2 purge, a five-second exposure to ~2% O_3 in O_2, and a final N_2 purge. During this complete cycle the total pressure in the hot-wall ($T_{reactor}$ = 150-300°C) reactor is typically 2 Torr, and a 1.6Å layer of crystalline ZnO is formed.[68,69] The cycle is repeated to achieve the desired film thickness. The presence of the N_2 purges prohibits direct, gas-phase reaction of DEZ and O_3, and thus the ozone must react with surface-adsorbed ethylzinc groups. The two molecules shown in (Scheme 3.1) were chosen to serve as models of an ethylzinc unit bound to an oxide surface. Although neither structure has been isolated as a pure

compound, both are structurally similar to known zinc organometallics. The HO-Zn-Et compound is related to dialkylzincs and our computational results agree well with analogous DFT results reported by Varma and Ault for MeZnOMe using the B3LYP functional.[2]

Compounds having the formula, R'Zn(OR) are known to exist as tetrameric solids, which have been used in CVD as single-source precursors to ZnO.[71]
The structure of $[R'Zn(OR)]_4$ is presumably a cubane similar to those found in $[(ZnOMe)_2\bullet(EtZnOMe)_6]$ and *N*-[salicylidenethanolaminatoZn(II)]$_4$.[72,73] Table 3.1 compares selected bond distances and angles of $[(HO)_7Zn_4(Et)]$ to the experimental values of related compounds.

Table 3.1 X-ray crystal data for zinc tetramers analogous to the DFT model compound $[(HO)_7Zn_4(Et)]$.

Geometry	**$[Zn(OMe)_2\bullet(EtZnOMe)_6$**	**N-[Salicylidenethanol-aminatoZn(II)]**	**$[(HO)_7Zn_4(Et)]$**
Zn-O (Å)	2.06	2.140 (0.25)	2.116 (0.03)
Zn-C (Å)	2.07		1.960
Zn-O-Zn (°)	97.0	97.7 (7.56)	97.76 (0.90)
O-Zn-O (°)	82.5	81.46 (6.12)	80.03 (0.23)

In the following sections structures **1** through **9** and transition states **TS 1** through **TS 5** outline the chemical events for a complete ALD cycle involving HO-Zn-Et (Figures 3.1, 3.3, 3.5). Figure 3.3 shows the steps involved in the ozone insertion into the Zn-Et bond of the cubane starting compound (structures **10** through **13** and **TS 6** and **TS 7**), and structures **14** - **16** and **TS 10** and **TS 11** detail the reactions involved in adding diethylzinc to $Zn_4(OH)_8$ in (Figure 3.6).

3.3.2 Step 1. Oxygen Atom Insertion Into the Zn-Et Bond

We find the reaction of HO-Zn-Et (**1**) with ozone to require two equivalents of O_3 to replace the ethyl substituent with a hydroxyl group. The mechanism of this reaction begins with formation of a metal-ozone complex (**2**) in which both of the terminal oxygens of the ozone chelate to the zinc. This reaction is exergonic by -9.6 kcal/mol and is followed by a still more exergonic reaction (-48.1 kcal/mol) involving ethyl migration to one of the terminal oxygens of the coordinated ozone (**TS 1**) to form an ethyltrioxide ligand bound to zinc (**3**). The calculated activation free energy for the migratory insertion is only 1.7 kcal/mol. As illustrated in (Figure 3.2), the structure of HO-Zn-OOOEt (**3**) has a short (1.85Å), alkoxide-like bond involving the terminal oxygen and a long (2.33Å) bond to the carbon-bound oxygen. In the last step in this sequence, the non-carbon-bound O_2 unit within the trioxide twists and dissociates as singlet oxygen (**TS 2**) as the ether-like oxygen transforms into an ethoxide ligand (**4**). In **TS 2**, the dihedral angle, Zn-O-O-O, is 51°. The reaction is exergonic by 20.4 kcal/mol (before accounting

for the additional energy gain associated with subsequent spin crossing of O_2 to its triplet ground state), and the activation free energy is small (4.0 kcal/mol).

Some precedent for this proposed reaction scheme does exist. The decay of organic hydrotrioxides, RC(O)OOOH, to singlet oxygen has been observed for aldehyde ozonolysis resulting in the ultimate formation of carboxylic acids.[74]

Additionally, metal alklytrioxides such as $(t\text{-BuO})_{n-1}M(O_3\text{-}t\text{-Bu})$ where n is 3 or 4 for metals aluminum and titanium, respectively, have been proposed as intermediates that undergo loss of singlet oxygen resulting in metal alkoxide species.[75]

An IR frequency calculation at the M06-L/6-31+G(d,p) level was performed on both the ethyltrioxide and the ethoxide complexes. The ethyltrioxide (**3**) IR spectrum exhibited a vibrational frequency of 873 cm^{-1} corresponding to an O-O stretch that matches a feature at 869 cm^{-1} in the unidentified complex/cage pair species trapped from a twin jet matrix isolation experiment of $ZnMe_2$ and O_3 reported by Varma and Ault.[2] This stretch was also reported to *decrease* upon UV irradiation of the matrix with subsequent formation of MeZnOMe.[2]

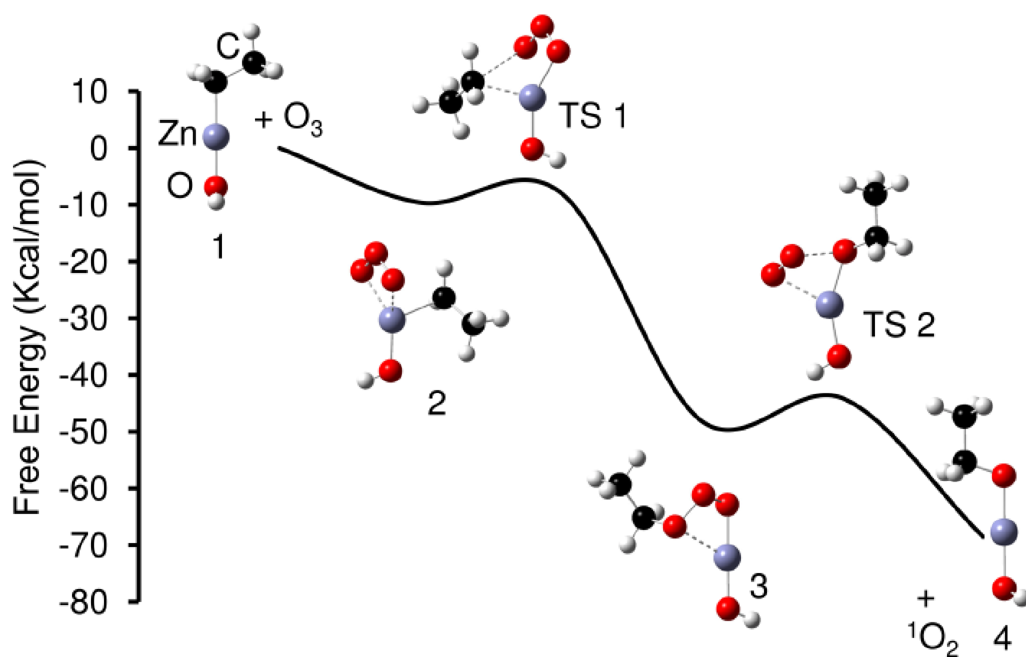

Figure 3.2 Reaction coordinate showing the insertion of ozone into the Zn-Et bond of the (HO)ZnEt. Hydrogen atoms are white, carbon atoms gray, oxygen atoms red and zinc atoms are slate blue. Lines connecting stationary points are provided for viewing convenience.

To investigate more directly the possibility that the intermediate identified by Varma and Ault was the corresponding methyltrioxide complex of ZnMe, calculations were performed on MeZnOOOMe and MeZnOMe for a direct comparison of the vibrations to the species observed in the matrix isolation experiments.[2] The calculated vibrational spectrum for the methyltrioxide complex and that reported for the complex/cage pair over the range from 600 to 1200 cm^{-1} are presented in Table 3.2. The

spectral match, especially the presence of the O-O vibration at 869 cm^{-1}, strongly suggests that the observed species was the methyltrioxide complex. All four IR frequencies are due to either vibrations of the ozonide itself or vibrations of the ozonide coupled with the methyl group. The disappearance of these frequencies upon UV irradiation of the matrix supports the proposed loss of oxygen and formation of MeZnOMe.[2] For MeZnOMe itself, our calculated structure and vibrational spectrum agree well with those from earlier work (Table 3.3 and Table 3.4). The most intense IR vibration in the experimental spectrum occurs at 1090 cm^{-1} and is assigned to an asymmetric Zn-O-Me stretch based on the M06-L calculations. This vibration was *not* observed in the calculated spectrum of the methyltrioxide complex, further supporting the hypothesis that the observed intermediated is MeZnOOOMe.

Table 3.2 Measured and calculated IR absorptions assigned to the complex/cage pair formed in an Ar matrix from the reaction of Me_2Zn and O_3. The first column lists the experimental values[2] and the second column lists the predicted absorptions for $MeZnO_3Me$ calculated using the M06-L DFT functional and the 6-31+G(d,p) basis set.

Complex/cage pair cm^{-1}	**Methyltrioxide cm^{-1}**	**Assignment**
638	651 (0.87)	O_3 asymmetric
869	892 (0.30)	O_3 symmetric
975	990 (0.72)	CH_3-O coupled O_3 symmetric
1175	1190 (0.20)	CH_3-O rock coupled to O_2

Table 3.3 Bond lengths and angles for MeZnOMe as calculated by Varma and Ault with B3LYP[2] and compared to M06-L calculations used in this study.

Geometry	B3LYP [MeZn(OMe)]	M06-L [MeZn(OMe)]
Zn-O (Å)	1.789	1.781
Zn-C (Å)	1.935	1.912
C-H (Å)	1.09	1.10
C-Zn-O (°)	174.7	174.1
Zn-O-C (°)	131.3	127.5

Table 3.4 Measured and calculated IR absorptions assigned to matrix isolated MeZnOMe.

Methoxide experimental[2] cm^{-1}	**Methoxide B3LYP[2] cm^{-1}**	**Methoxide M06-L cm^{-1}**	**Assignment**
526	494 (0.036)	509 (0.033)	Me-Zn-O symmetric
1090	1109 (1)	1132 (1)	Zn-O-Me asymmetric
1195	1186 (0.073)	1187 (0.116)	Zn-O stretch Me-O rock
1452	1480 (0.09)	1473 (0.118)	Me-O stretch umbrella
2815	2957 (0.52)	2959 (0.717)	C-H symmetric Me-O
2895	3028 (0.219)	3064 (0.290)	C-H stretch
2932	3107 (0.033)	3171 (0.030)	C-H stretch
2948	3109 (0.033)	3174 (0.032)	C-H stretch

In the cubane model **10** in(Figure 3.3), the ethyl group is attached to a four coordinate zinc ion, which is probably closer to the situation found for a surface bound ethylzinc group. At the M06-L/6-31+G(d,p) level, stationary points corresponding to an ozone-bound intermediate (**11**) and a TS structure (**TS 6**) for ethyl migration were located with the latter predicted to be only 0.2 kcal/mol above the former in free energy. Adding thermal contributions to single-point electronic energies at the M06/6-311+G(2df,p) level, by contrast, predicts **TS 6** to be 0.9 kcal/mol LOWER in free energy than the

preceding intermediate. The two stationary points are shown in (Figure 3.3) but it is evident that the nature of the potential energy surface in that region of the reaction coordinate is quite flat such that the ethyl migration reaction may be regarded as proceeding effectively without any barrier. The activation energy for the elimination of $^{1}O_2$ from **12** through **TS 7** is 12.7 kcal/mol, which is slightly higher than that found for the two-coordinate zinc compound. Evidently, the greater rigidity of the cubane structure adds energetic constraints that increase the activation energy. The conversion from **12** to **13** is exergonic by 20.7 kcal/mol.

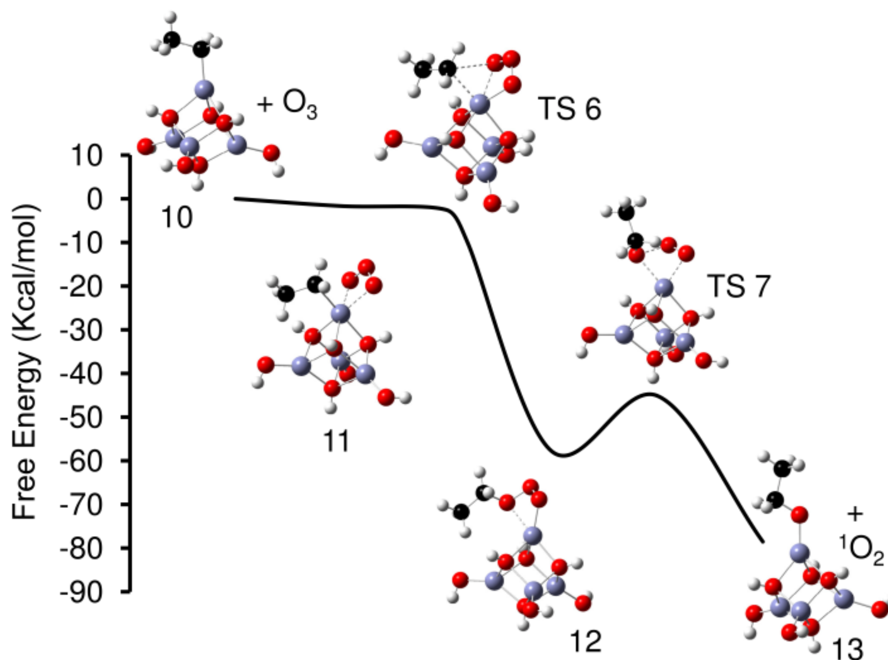

Figure 3.3 Reaction coordinate showing the insertion of ozone into the Zn-Et bond of the $(HO)_7Zn_4Et$.

3.3.3 Step 2. Reaction of the Second Equivalent of Ozone with Zinc Ethoxide

With the transformation of the original ethyl group into a stable ethoxide ligand, a second equivalent of ozone must be required to complete the ligand transformation to hydroxide, leaving a layer that can serve as the starting point for subsequent reaction with $ZnEt_2$ in the second stage of the ALD process. To clarify, we exclude from consideration the hydroxyl ligand that was present in (HO)ZnEt from the beginning because it served as a surrogate for the zinc oxide surface.

As shown in (Figure 3.4) ozone reacted with (HO)ZnOEt to form a complex (**5**) more stabilized than that found for the ethylzinc compound. In the absence of an ethyl into which the ozone can insert, complex **5** undergoes a β-hydrogen abstraction via **TS 3** resulting in a hydrotrioxide (**6**) with concomitant elimination of acetaldehyde. The hydrotrioxide decays in a fashion similar to that of the ethyltrioxide and results in a hydroxyl ligand (**7**), which is a necessary requirement for ALD growth of metal oxides.[70] The decay of the hydrotrioxide is again analogous to the aforementioned aldehyde/metal ozonide chemistry.[74,75] The overall thermodynamics of Step 2 are also favorable with the free energy change being exergonic even for the production of singlet oxygen.[76]

The mechanism is similar when the reaction of O_3 with the cubane complex bearing the ethoxide ligand (**13**) is considered. Once again, the initial O_3 adduct does not appear as a minimum. In addition, there is virtually no activation barrier for the concerted β-hydrogen abstraction that leads to acetaldehyde and the hydrotrioxide ligand. The $\Delta G^{\neq}$ for the elimination of $^1O_2$ is 7.5 kcal/mol, which is similar to that found for

(HO)Zn(OOOH), **6**. The final zinc product produced from 2 equivalents of ozone is the fully hydroxylated cubane, $Zn_4(OH)_8$ (**14** in Figure 3.6).

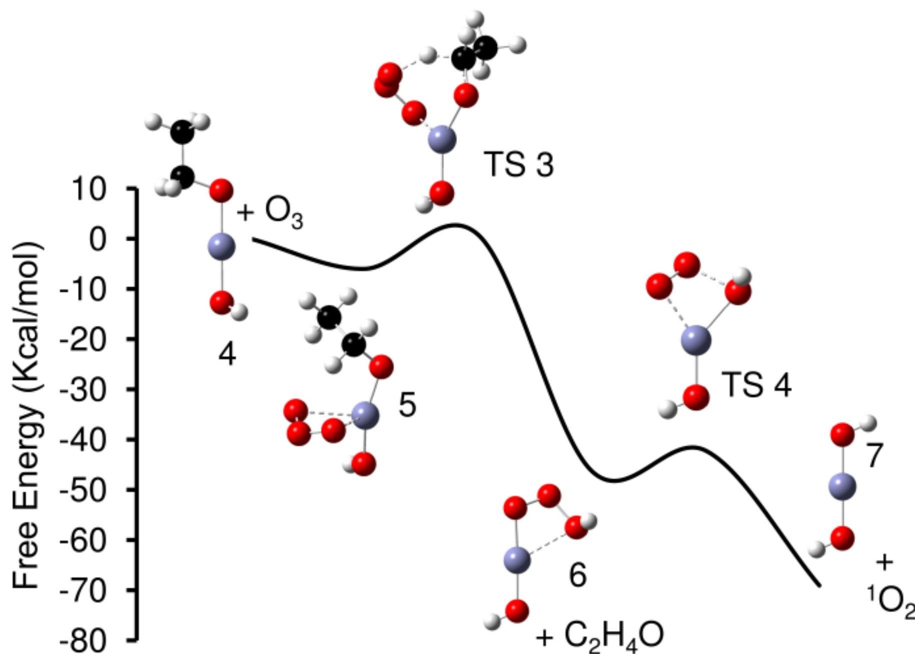

Figure 3.4 Reaction coordinate for the second ozone reaction leading to the elimination of acetaldehyde

3.3.4 Diethylzinc Additions to Zinc Hydroxyl Ligands

Although the focus of this study is on the ozone chemistry, using computational methods we also examined the mechanistic details of the steps involved in the *second* part of the ALD process, i.e., the reaction of diethylzinc with a surface hydroxyl. Being electron deficient, $ZnEt_2$ is a Lewis acid that forms a donor-acceptor bond with a lone

pair of electrons of a hydroxyl group on either $Zn(OH)_2$, **7**, or $Zn_4(OH)_8$, **14**. In both models, the formation of the new Zn-O bond occurs without an activation barrier, and the product has a lower free energy than the separated reactants by 5.6 and 3.0 kcal/mol, respectively, for $Zn(OH)_2$ or $Zn_4(OH)_8$.

These intermediates can undergo a thermodynamically favorable 1,2-elimination of ethane through a four-membered transition state illustrated in (Figure 3.5 and Figure 3.6.)

The activation energies for the formation of (HO)ZnOZnEt, **9**, and $(HO)_7Zn_4(OZnEt)$, **16**, were 25.8 and 34.4 kcal/mol, respectively. Considering the well-known facility of the reaction of the first ethyl group in $ZnEt_2$ with water or alcohols at room temperature and below, these values of $\Delta G^{\neq}$ seem somewhat high.[77] It is likely that the strain associated with the four-membered-ring TS structure (**TS 8**) contributes to the higher barrier. The presence of additional hydroxyl groups in the cubane model, however, allowed us to probe the effect of involving a non-adjacent hydroxyl in the ethane elimination. As illustrated in (Figure 3.6), using a non-adjacent hydroxyl leads to a less-strained, six-membered cyclic structure, **TS 9**. The activation free energy calculated for this 1,4-ethane elimination is 6.1 kcal/mol lower than that found for the 1,2-elimination. In the 1,4-elimination, the subsequent hydrogen transfer required to reform the -OH of the cubane core is expected to be facile. In addition to the more favorable geometric consideration alluded to above, the removal of the hydrogen from a μ_3-hydroxyl may be easier as a result of stabilization of the resulting μ_3-oxo.

In computational studies of Al_2O_3 deposition by ALD, several groups have reported high values for the 1,2-elimination of methane from trimethylaluminum bonded to a surface hydroxyl, thiol, or amine group.[78-85] Recently, Delabie *et al*. examined the methane elimination that occurs when trimethylaluminum reacts with a more complex cluster having four hydroxyls, $Si_7H_8(OH)_4$, and found higher activation barriers for methane elimination from the more remote hydroxyls. Specifically, the activation energies ($\Delta E^{\neq}$) for 1,5- and 1,6-eliminations were 13.8 and 18.8 kcal/mol, respectively, compared to 11.2 kcal/mol for the 1,2-elimination.[82]

Bearing in mind that these two studies differ by the precursor, they highlight the critical impact that surface structure can have in ALD.

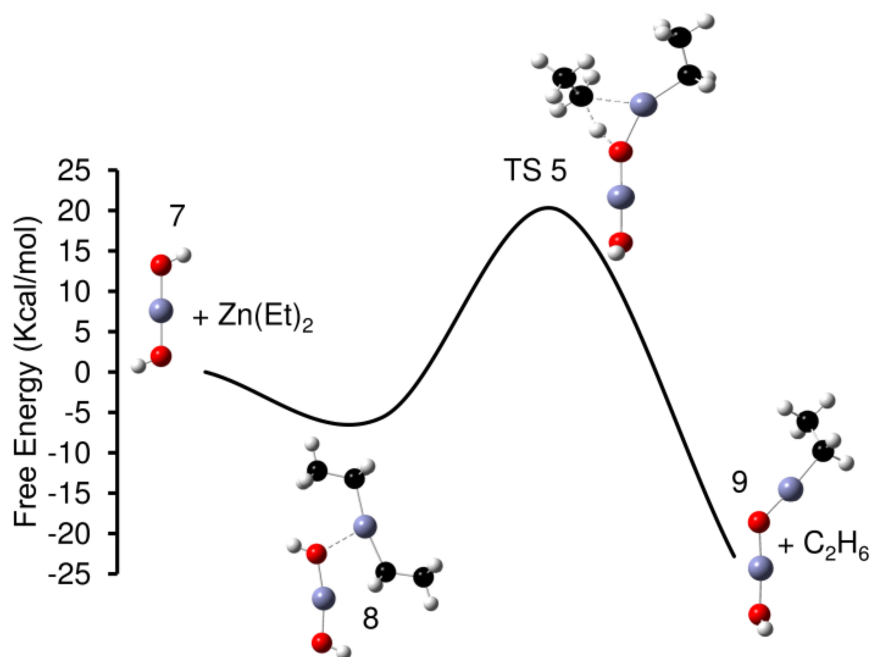

Figure 3.5 Reaction coordinate for the 1,2-elimination of ethane upon addition of $ZnEt_2$.

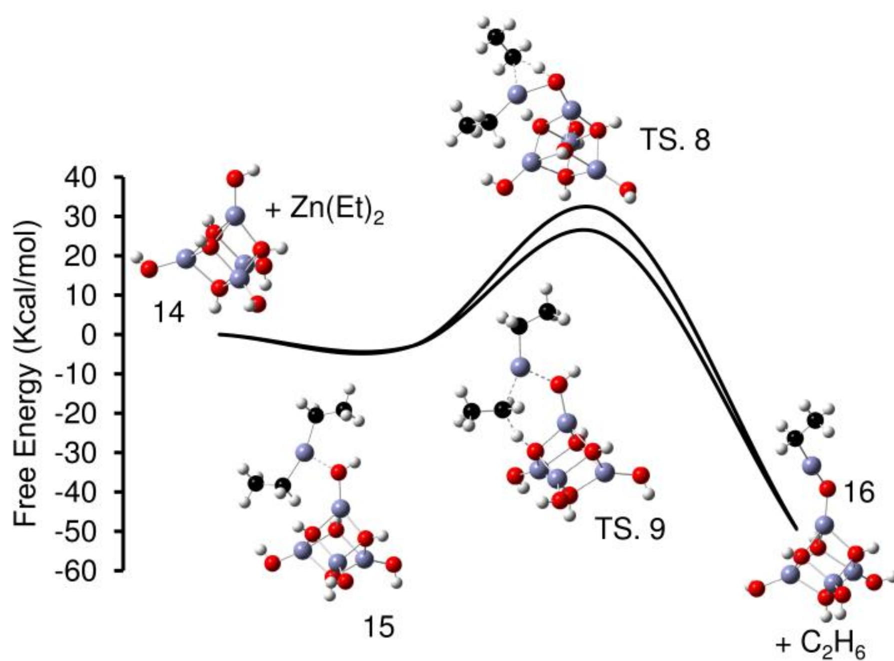

Figure 3.6 Reaction coordinate for the 1,2- and 1,4-elimination of ethane from the cubane-like model.

3.3.5 Detection of Acetaldehyde

Based on our computational work, the overall deposition chemistry can be summarized as in eq. 3.1.

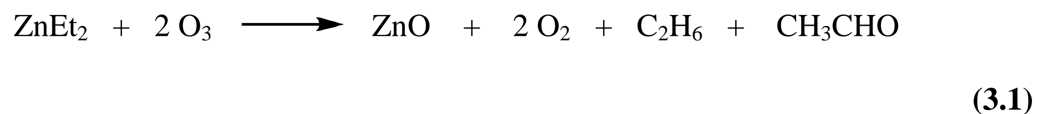

$$ZnEt_2 + 2\,O_3 \longrightarrow ZnO + 2\,O_2 + C_2H_6 + CH_3CHO \quad \textbf{(3.1)}$$

This is consistent with reports of the gas phase chemistry of dialkylzincs and ozone as well as with observations in the ALD of Ga_2O_3 using O_3 and $GaMe_3$.[58,62] Equation 3.1 does not take into account possible further oxidation of the organics ultimately to CO_2 and H_2O. To determine if acetaldehyde was formed during the ozone pulses of the ALD reaction, we equipped our reactor with a cold trap to collect the condensable products. To avoid co-condensing diethylzinc with the products, only during the ozone pulse was the reactor effluent diverted through the trap. As an additional safety precaution, the trap was maintained at a temperature (–78°C) that avoided ozone condensation (bp = –112°C). This precaution reduced the trapping efficiency for condensable organics.

The ^{1}H NMR spectra of the trap contents for ALD cycles involving O_3 indicated acetaldehyde production by resonances observed at δ 9.8 (1H, q) and 2.2 (3H, d) ppm. More importantly, acetaldehyde production versus the number of ALD cycles was found to increase linearly, which is consistent with acetaldehyde resulting from the reaction of O_3 with a chemisorbed ethylzinc intermediate (Figure 3.7).

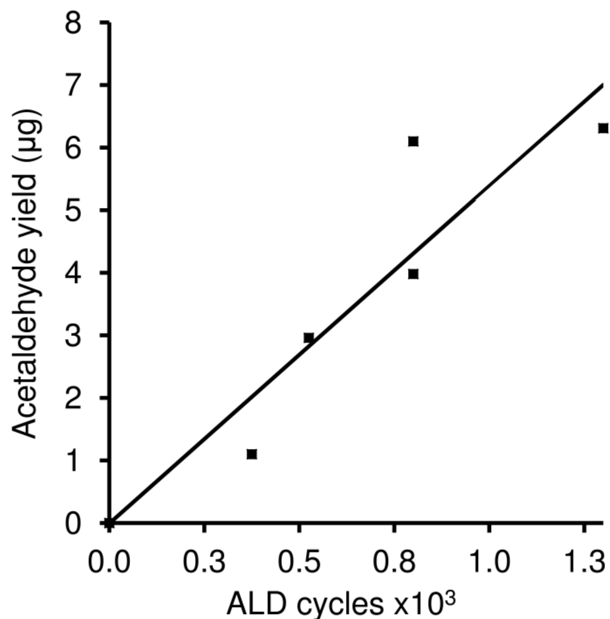

Figure 3.7 Graph correlating the quantity of acetaldehyde and the number of ALD cycles

3.3.6 Does Atomic Oxygen Play a Role?

At room temperature ozone will slowly react to form oxygen, and the kinetics and mechanism of this reaction has been studied since the early 1900s.[86,87] Both higher temperatures and higher ozone concentrations lead to more rapid decay. The mechanism (eqs. 3.2 and 3.3, where M can be N_2, O_2, O_3, or any other gas molecule) involves the

intermediacy of atomic oxygen, which raises the question as to whether oxygen atoms are the active species in ozone-based ALD.[42]

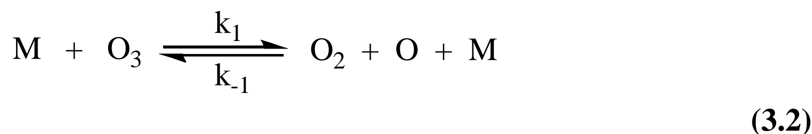

(3.2)

(3.3)

Based on the following analysis, we conclude that free O atoms are not a factor. It is true that O atoms would be expected to react rapidly with species on the surface. The reactions of ozone described earlier, however, are also barrierless or nearly so. Therefore, the competition between O atoms and O_3 in reactions with surface species would be dominated by the relative concentrations of O and O_3 in the gas phase. Using the three known rate constants in eqs. 3.2 and 3.3, we can integrate the rate expression to determine the ozone concentration as a function of time, O_3 concentration, total pressure, and temperature.[86] Starting from a 2% O_3 mixture in O_2 maintained in a sealed system at 250°C with a total pressure of 1 Torr, one-half of the ozone is consumed in 53 s. The residence time in our ALD reactor is estimated to be 0.15 s, which suggests that the amount of ozone lost by thermal conversion to O_2 will be small during each ozone pulse.

The above analysis does not exclude the possibility of involving surface-bound atomic oxygen as an intermediate. Infrared studies of ozone reactions with strong Lewis

acid sites of metal oxides provide evidence for the intermediacy of oxygen atoms in the oxidation of CO to CO_2.[88, 89] In our computational studies, we were unable to force the removal of O_2 from a coordinated ozone in HO-Zn(O_3)-Et without observing simultaneous migration of the ethyl group to produce the ethoxide. All stages of this process occurred at higher energies than the intermediates and transition states shown in (Figure 3.2).

3.4 Conclusions

A mechanism has been identified that rationalizes the ALD reaction between diethylzinc and O_3 using computational model systems involving either a 2-coordinate zinc complex, HO-Zn-Et, or a 4-coordinate zinc that is part of a cubane-like precursor,[$(HO)_7Zn_4(Et)$]. Ozone is found to produce an intermediate ethyltrioxide after reaction with surface-bound ethyl zinc. The ethyltrioxide subsequently decomposes to form an ethoxide in both model systems.

The addition of a second O_3 to the intermediate ethoxide results in a β-hydrogen abstraction that ultimately generates an ALD active hydroxylated zinc oxide surface and produces acetaldehyde. The acetaldehyde byproduct has been observed by ^1H NMR in ALD effluent, which supports this computationally derived mechanism for ALD growth of zinc oxide.

3.5 Acknowledgement

This research was supported by a grant from the Department of Energy (USDOE/DE-EE0005319), funds from the University of Minnesota Institute for Renewable Energy and the Environment, and the National Science Foundation (CHE-0952054).

CHAPTER FOUR

Atomic Layer Deposition of Tin Oxide and Zinc Tin Oxide for Photovoltaic Applications

4.1 Summary

Tin oxide (SnO_2) has been deposited using atomic layer deposition (ALD) with a novel precursor combination incorporating tetraethyltin (TET) and ozone (O_3). This precursor combination was also successful in sequential ALD of zinc tin oxide (ZTO) with diethylzinc (DEZ) being utilized as the zinc source.

The ZTO film properties were consistent with transparent conducting oxides, having an optical bandgap of approximately 3.5 eV and carrier concentrations in the 10^{18} to 10^{19} range. The films had lower than expected density which may be the result of an amorphous 4-coordiante tin oxide. The low density tin oxide material was modeled using both computational chemistry with density functional theory (DFT) and the empirical densities of known IV-VI materials. The density of the modeled 4-coordiante SnO_2 material was in close agreement with the observed density for the SnO_2 in the ZTO films.

In addition to depositing and characterizing the ZTO, a broken gap tunnel junction was fabricated using the ALD deposited ZTO (n-type material) with a sputtered cuprous oxide (p-type) material. The junction demonstrated an ohmic contact indicative of a tunnel current and has applications in multi-junction photovoltaic cells where optical transparency and conductivity are essential.

4.2 Introduction

Tin oxide (SnO_2) is an n-type transparent conducting oxide (TCO) with a wide bandgap of approximately 3.8-4.2 eV.[90] Tin oxide films are industrially important materials as a result of their high conductivity, optical properties, and stability. Common applications for tin oxide and doped tin oxide materials include photovoltaics, oxidation catalysts and gas sensors.[91] Tin oxide has been deposited in thin films by metal organic chemical vapor deposition (MOCVD), sputtering, sol-gel, pulsed laser deposition, molecular beam epitaxy and from atomic layer deposition (ALD).[32,92]

Deposition of SnO_2 and doped SnO_2 films by ALD has specific advantages in coating high aspect ratio surfaces, or in cases where thin uniform coatings are a requirement such as electrical contacts on rough surfaces. Tin oxide has successfully been deposited by ALD using various tin precursors with an oxygen source including $SnCl_4/H_2O$, tetrakisdimethylaminotin, cyclic amide's of $Sn(II)/H_2O_2$, and alkyl tin compounds such as tetramethyl and tetraethyltin/N_2O_4.[32,33,29, 93] The alkyl tin precursors are of interest because their commercial availability and high vapor pressure make them suitable for an ALD process.

In addition to tin oxide, interest in depositing zinc tin oxide (ZTO) by ALD has increased as a result of ZTO electronic properties. Zinc tin oxide has similar applications as tin oxide and can be used in photovoltaics as anode materials for dye sensitized solar cells and also for its photocatalytic activity.[94] Additionally the n-type material may have the correct band structure for use in fabricating tunnel junctions for tandem solar cells.

Zinc tin oxide films have been deposited by ALD using tetrakisethylmethylamino tin and diethylzinc with O_2 plasma as well as cyclic amides of Sn(II) and diethylzinc with H_2O_2.[95,39] The diethylzinc precursor used for depositing ZTO films is a common zinc precursor used in ALD for depositing zinc oxide and can be used with multiple oxygen sources including H_2O, H_2O_2 and O_3.[27,96,25]

In this paper we demonstrate the deposition of tin oxide and ZTO material using tetraethyltin (TET) and ozone precursors. Tin oxide has previously been deposited using TET with N_2O_4 and it was believed that ozone would have similar reactivity to the alkyl metal bond and result in formation of the metal oxide.[26]

Deposition of the ZTO material utilized a sequential deposition method where alternating angstrom thick layers of ZnO and SnO_2 were deposited from TET/O_3 and DEZ/O_3 where the number of SnO_2 and ZnO cycles controlled the film composition. In addition to fabricating and characterizing these materials, the ZTO films were used as an n-type semiconductor to fabricate a tunnel junction device for applications in a multi-junction solar cell.

4.3 Experimental

Silicon (100) substrates were cleaned by immersion for 1 h in a solution consisting of 70% H_2SO_4 diluted to 100% with H_2O_2(30%). The substrates were removed and immersed for 10 min in 30% HF to remove the native oxide and produce a hydrophobic surface. Soda lime glass substrates used for electrical and optical characterization were

rinsed with ethanol and dried under a nitrogen stream. After cleaning, the substrates were immediately loaded into a hot wall ALD reactor, which was then evacuated prior to deposition.

The metal oxide films were deposited using diethylzinc (DEZ) as the zinc source (Sigma-Aldrich), and tetraethyltin (TET) as the tin source (Sigma Aldrich). Both metal precursors had sufficient volatility to be used without a carrier gas and were introduced into the reactor by vapor pressure draw from stainless steel precursor vessels with 50 cc of head space. The vapor pressure was controlled by a circulating water bath around the TET which maintained the temperature between 21 to 22 °C and a chilled ethylene glycol/ water solution around the DEZ which maintained a -20 to -15 °C with a commercial cryocool™ chiller.

The oxygen source (O_3) was delivered to the reactor at 2-4% O_3 in oxygen by a Dwyer ozone generator connected to an oxygen tank. The purge pulse separating the metal precursor and ozone pulses was high purity nitrogen supplied at 100 sccm. All precursors and purge pulses were introduced into the reactor via a set of pneumatically controlled valves.

Characterization of both SnO_2 and ZTO film thicknesses for calculating deposition rate were determined by a J. G. Woollam VASE® spectroscopic ellipsometer. Elemental analysis was determined by Rutherford Backscattering Spectroscopy (RBS) using signal integration as well as Quark© and SIMNRA© fitting software with a MAS 1700 pelletron tandem ion accelerator (5SDH) equipped with charge exchange RF plasma source by National Electrostatics Corporation (NEC).

STEM EDX line scans of selected film cross sections were also used for elemental and thickness comparisons. Film structure was characterized by XRD using a Bruker-AXS Microdiffractomater. Optical properties were measured on an Ocean Optics UV-Vis spectrometer and electrical properties were determined from hall measurements on a Quantum Design Model 6000 PPMS.

4.4 RESULTS AND DISCUSSION

4.4.1 ALD of SnO_2 with TET and Ozone

The deposition of SnO_2 films using TET and ozone was studied as a function of precursor pulse times and substrate temperature. The self-limiting nature of ALD deposited tin oxide was determined by depositing films at 300 °C and incrementally increasing the pulse time of TET while keeping all other purge and oxidant pulses at 8s. Tetraethyltin was also tested for ALD with H_2O (3.5s) and O_2 (8s) as the oxygen source with negligible deposition observed at 290 °C for 150 cycles. Tetraethyltin had sufficient volatility that it could be introduced into the reactor without the use of a carrier gas. At 21 °C the vapor pressure was determined to be 390 mtorr from the Antoine equation which was in close agreement with a measured value of approximately 300 mtorr when TET was allowed to saturate the reactor chamber.[97] The reactor pressure during a TET pulse for ALD depositions was measured to be 70 mtorr.

Initial depositions were performed using a 50 cm^3 headspace glass precursor vessel which reached a self limiting saturation in film deposition rate of 0.2 nm/cycle in 4s. For safety concerns, the glass precursor vessel was replaced with a stainless steel vessel (35 cm^3 head space). Films deposited using the stainless steel precursor vessel were observed to require increased TET exposure time of 6s to obtain the self-limiting deposition rate of 0.2 nm/cycle.

The reduced headspace of the stainless steel verses glass vessel was the most likely reason for the observed increase in TET exposure time required for self-limiting deposition. The difference in thermal conductivity between stainless steel and glass was determined to not have an effect on the TET saturation time as the increased thermal conductivity of the stainless steel vessel would be expected to have shorter TET saturation times instead of the observed longer pulse times.

The saturation profile for the stainless steel vessel indicated that the deposition rate increased linearly from 0.1 nm/cycle for a 1s TET pulse up to 0.2 nm/cycle for 6s TET pulse, after which the film deposition rate leveled off and plateaued through 12s of TET exposure (Figure 4.1).

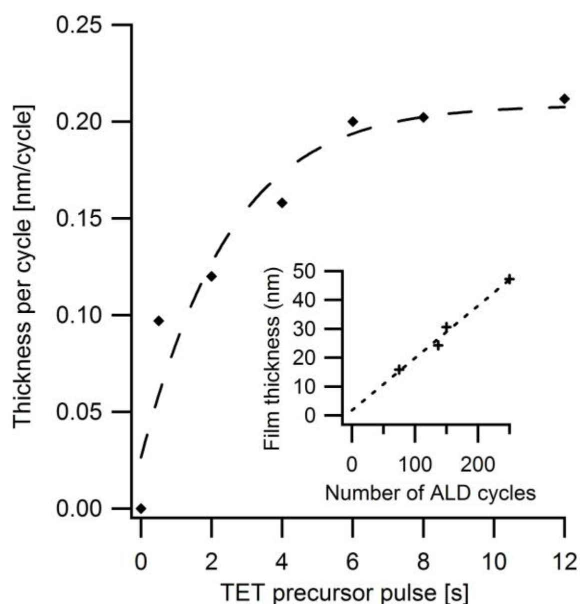

Figure 4.1 The saturation curve for SnO_2 deposition as a function of TET pulse time versus deposition rate.

The temperature window for ALD of tin oxide was determined by varying the deposition temperature from 250 °C to 390 °C and measuring film thickness as a function of ALD cycles (Figure 4.2). The pulse sequence used for determining the ALD window was N_2(8s), TET(8s), N_2(8s), O_3(8s) for 150 cycles. Although it appeared that the temperature dependence of the deposition rate displayed a nonlinear increase between 250 °C and 390 °C, careful examination of multiple depositions indicated a narrow region where the film deposition rate was constant. The plot of deposition rate vs. deposition temperature showed a linearly increasing film growth rate between 250 °C and 290 °C which plateaued within a narrow region between 290 °C to 320 °C where a linear

growth rate of 0.2 nm/ cycle was observed. This narrow ALD temperature window has previously been observed for the ALD of SnO_2 with TET and N_2O_4 between 250 °C and 290 °C.[29]

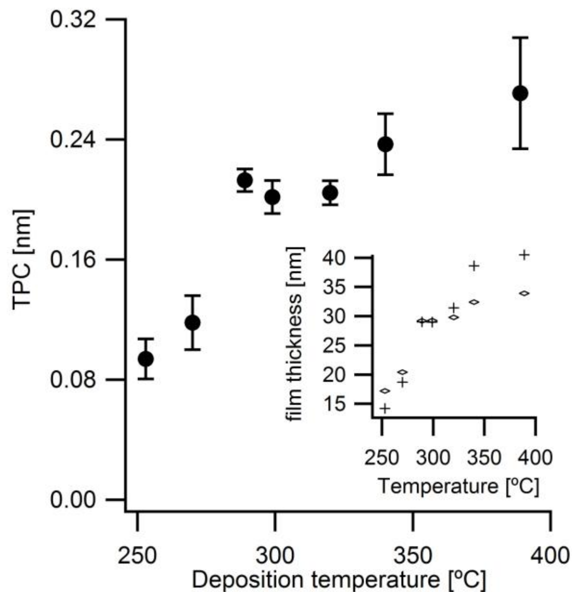

Figure 4.2 ALD window for SnO_2 deposition using TET and O_3 precursors each data point corresponds to the average deposition rate of 3 films and the error bars indicate the standard deviation between these films. The inset indicates the observed thicknesses for films deposited close to the hot zone inlet and close to the hot zone outlet.

As the deposition temperature increased beyond 320 °C, the growth rate increased above a monolayer /cycle. In addition to the increased growth rate, a large thickness gradient appeared in deposited films with those nearest the hot zone inlet appearing

substantially thicker than those near the hot zone outlet indicative of precursor depletion, a trend which is reflected in the large standard deviation of film thicknesses deposited at temperatures greater than 320 °C and illustrated in inset (Figure 4.2).

Elemental analysis of films deposited within the ALD window on silicon substrates by Rutherford backscattering spectrometry revealed SnO_x films (Figure 4.3).

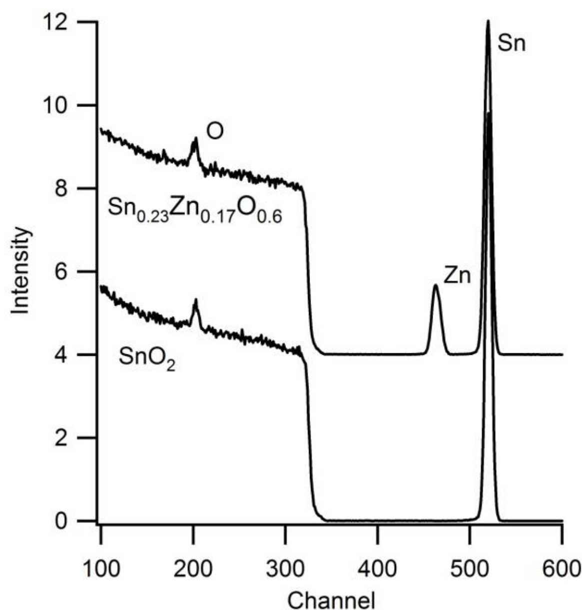

Figure 4.3 Representative RBS spectrum of ZTO and tin oxide films deposited on silicon substrates using TET&O_3 within the ALD window.

Further analysis of the representative RBS spectrum revealed a film stoichiometry of $SnO_{1.98}$ for the as deposited film.[98] Film densities were determined to be 5.4 g/cc (~80% bulk rutile SnO_2) using Quark© RBS software with thicknesses provided by spectroscopic ellipsometry.

Analysis by XRD indicated as deposited films were amorphous with the rutile SnO_2 phase appearing in post annealed (1hr at 700 °C) films. The films were optically transparent at wavelengths greater than 400 nm and had 4 point probe resistivities in the $2x10^{-3}$ Ω•cm range. Hall measurements were conducted at 300 °K with magnetic field sweeps from 0 to 20,000 Oe on SnO_2 films deposited on glass substrates. The carrier concentrations and mobilities from the Hall measurements were determined to be $1x10^{21}$ $cm^{-3}$and 3 $cm^2V^{-1}s^{-1}$ for a 30 nm film. The observed electrical properties for the ALD SnO_2 films were similar to sputtered SnO_2 films as well as ALD tin oxide films deposited by Gordon et al with cyclic amides of Sn(II) as the tin precursor.[93, 99]

4.4.2 Sequential Deposition of ZTO Films

Zinc tin oxide films were deposited using supercycles consisting of (n)SnO_2 cycles followed by one ZnO cycle where n was varied from 1 to 10 for all depositions. All films deposited for the ZTO materials were deposited in the tin oxide ALD window at 290 °C with TET pulses equal to 8s, N_2 purge pulse 8s, and O_3 pulse 8s.

The deposition rate of tin oxide on zinc oxide was reduced compared to depositing tin oxide on pure tin oxide (Figure 4.4). The initial growth rate of SnO_2 dropped from 0.2 nm/cycle to 0.08 nm/cycle. This reduced growth rate was observed for 4 TET pulses per supercycle corresponding to 0.8 fraction of TET per supercycle, in (Figure 4.4) before gradually increasing, and required more than 1nm of SnO_2 deposited before the deposition rate improved to the intrinsic deposition rate of 0.2nm/cycle.

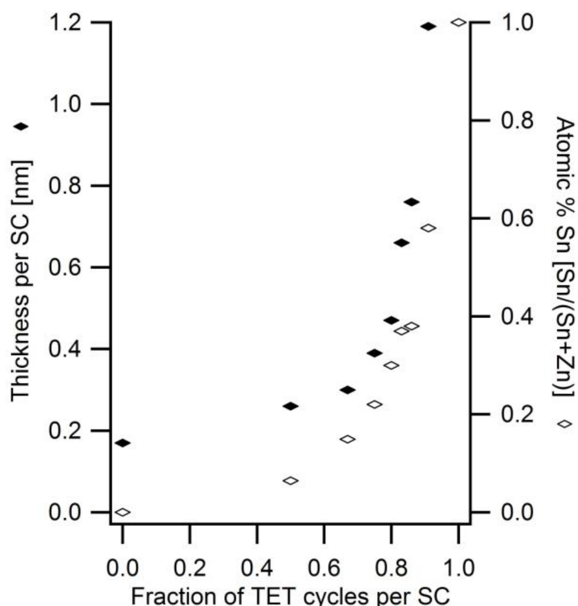

Figure 4.4 Deposition rate of ZTO as a fraction of tin cycles per super cycle plotted on the left axis. Film composition as measured by RBS is plotted on the right axis.

The slow recovery of the SnO_2 deposition rate has been observed for TET/N_2O_5 ALD when depositing on alumina and silica. It has also been observed that the growth rate SnO_2 was not impacted when depositing on TiO_2 and CrO_2.[29] The deposition rate's dependence on the substrate has been attributed to the ability of the substrate metal center to change its oxidation state. Substrates where the metal center could change oxide state showed an unaffected SnO_2 deposition rate whereas metal centers that could not change oxide state show a reduced SnO_2 ALD growth rate which suggested a redox reaction occurs between the precursor and the substrate.[29] The reduced deposition rate of SnO_2

from TET/O_3 on ZnO is consistent with prior observations in that zinc oxide exists solely in the Zn(II) oxide state unlike TiO_2 and CrO_2.[29]

Elemental analysis of the ZTO films was determined by RBS using integration and Quark© software to determine composition and density with thickness data obtained from spectroscopic ellipsometry. A representative ZTO RBS is shown in (Figure 4.3). The elemental analysis reflected the reduction in SnO_2 deposition rate on ZnO indicating that significantly more TET/O_3 pulses per DEZ/O_3 pulse were required to achieve spinnel (Zn_2SnO_4) and illmenite ($ZnSnO_3$) stoichiometries (Figure 4.4).

To determine the SnO_2 density in the ZTO films, the RBS composition data was fit using the deposition rate of ZnO (DR_{ZnO}), the number of ZnO cycles per super cycle (C_{ZnO}), the density of ZnO bulk material (ρ_{ZnO}), the film area (A), the molecular weights of SnO_2 and ZnO, and the total film thickness (T_{th}) while varying the density of SnO_2 (γ) to achieve the observed Sn/(Sn+Zn) ratio. The theoretical density of the ZTO films using this model indicated a low density SnO_2 oxide with an average density of 53% bulk rutile SnO_2 (4.1).

$$\left(\frac{Sn}{Sn+Zn}\right)=\frac{A*T_{SnO_2}*\rho_{SnO_2}*\gamma\Big/_{Mw_{SnO_2}}}{\left(A*T_{SnO_2}*\rho_{SnO_2}*\gamma\Big/_{Mw_{SnO_2}}+A*T_{ZnO}*\rho_{ZnO}\big/_{Mw_{ZnO}}\right)}$$

$$T_{SnO_2}=\ T_{th}-C_{ZnO}*DR_{ZnO}$$

$$T_{ZnO}=C_{ZnO}*DR_{ZnO}$$

(4.1)

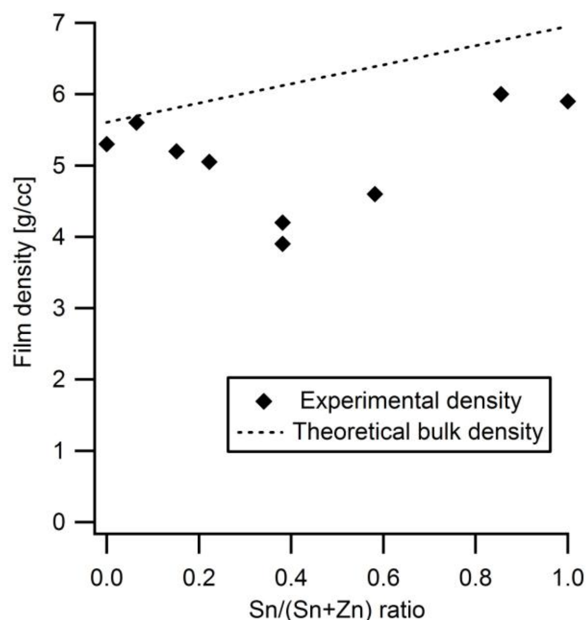

Figure 4.5 ZTO film densities as measured by RBS and calculated using a theoretical bulk density model.

The observed density from RBS measurements indicated lower than expected film densities of approximately 4.5g/cc for the ZTO films approaching the illmenite stoichiometry Figure 4.5 As the tin concentration in the films increased, the film density decreased to a minimum at approximately 40% tin. Beyond the ilmenite stoichiometry, the film density also increased reaching a maximum of 80% bulk rutile for SnO_2 films. This observed dip in density was in contrast to the expected density for ZTO films where a linear increase in specific gravity corresponding to the increasing density of tin oxide was anticipated and shown as the theoretical bulk density fit in (Figure 4.5).

The same density model used to fit the composition data in (Figure 4.4) suggested that a low density SnO_2 of approximately 37% of bulk was responsible for the reduction in film density at 40% SnO_2 concentration. The index of refraction as measured by spectroscopic ellipsometry at 560nm also declined from 2.05 with increasing SnO_2 cycles to a minimum of 1.85 at 80% SnO_2 cycles per supercycle before increasing back to 1.98 at 90% $SnO_2/(SnO_2+ZnO)$ cycles. The trend in refractive index lends support to an initial low density SnO_2 film on ZnO that eventually relaxes after a minimum thickness is achieved to form a more dense material.

Transmission electron microscopy was applied to a ZTO film cross-section to validate the spectroscopic ellipsometry measurement used in determining film thickness and density. In addition to the TEM images, STEM HAADF EDX line scans were collected for elemental composition to compare to the RBS measurements (Figure 4.6). The film thickness as measured by TEM indicated a ZTO layer of 38 nm which is in good agreement to the 38.3 nm measured by spectroscopic ellipsometry. The EDX elemental analysis of 62 at.% tin for this film was also in close agreement with the 67 at.% tin as measured by RBS. The TEM analysis provides important corroboration of film density by closely reproducing both the film composition as well as film thickness.

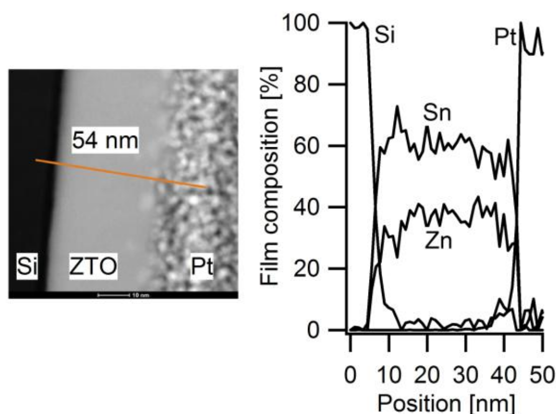

Figure 4.6 Cross section of ZTO film measured by TEM, including STEM HADDF EDX (55 nm) line scan for elemental analysis.

It was hypothesized that an initial amorphous 4-coordinate tin oxide could be responsible for the reduction in SnO_2 densities. Quartz phases of IV-VI materials namely SiO_2, GeO_2, and GeS_2 are well established where the metal is 4-coordiante. Tin oxide (also a IV-VI) material is known to form the 6-coordinate rutile structure in place of a 4-coordiante quartz phase. If a quartz phase of tin-oxide existed, it would most likely have a lower density than the corresponding 6 coordinate rutile.

Computational modeling was employed to quantify the change in density between 4-coordiante and 6-coordinate tin oxide. The as deposited films were amorphous by XRD, and it was determined that optimization of the 4-coordinate tetrahedron geometry could effectively predict the amorphous metal oxide density. This model effectively relies on a semi-empirical solution where a ratio of computed tetrahedral densities between SnO_2 and $IV(VI)_2$ (IV=Si, Ge; VI= O, S) tetrahedral densities is multiplied by

the known $IV(VI)_2$ density. Density Functional Theory (DFT) was employed for optimizing tetrahedrons of 4-coordinate IV-VI materials using the M06 functional and the 6-31+G(d,p) with SDD basis set for Sn and Ge metals (Figure 4.7). All calculations were performed using the Gaussian 09 software suite.[56]

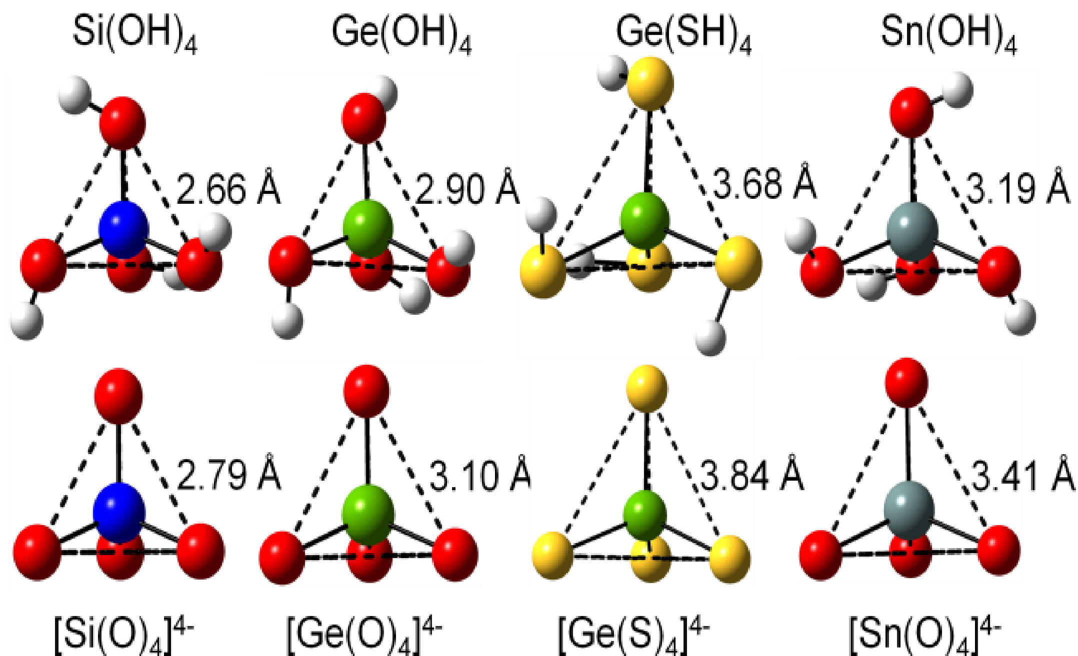

Figure 4.7 Optimized geometries of tetrahedral IV-VI materials used for calculating densities of amorphous quartz phase materials and predicting the density of 4-coordiante tin oxide.

Two tetrahedral models were used for optimizing the geometry of the metal oxides. The first model used a neutral $IV(VI\text{-}H)_4$ tetrahedron whereas the second model used a charged $[IV(VI_4)]^{4-}$ tetrahedron. The $[IV(VI_4)]^{4-}$ model resulted in an unstrained

tetrahedral geometry with bond angles corresponding to 109.47°. The neutral $IV(VI\text{-}H)_4$ model had strained geometries where the bond angles were slightly distorted. The bond lengths of the neutral model were in better agreement with literature values than the charged model (Table 4.1).

Table 4.1 Bond length and density for empirical and computed tetrahedral IV-VI materials.

	$IV(VI\text{-}H)_4$ bond length (Å) & density (g/cc)	**$[IV(VI_4)]^{4-}$- bond length (Å) & density (g/cc)**	**4-coordinate bond length (Å) & density (g/cc)**
SiO_2	1.64, 2.62	1.71, 2.39	1.615[3], 2.65
GeO_2	1.77, 5.03	1.90, 4.74	1.72[5] , 4.28[6]
GeS_2	2.26, 2.97	2.35, 2.51	2.19[7] , 3.01[7]
SnO_2	1.96, 6.10	2.09, 5.75	1.949[8]

The volumes of the tetrahedrons were calculated from the optimized dimensions. The mass contained within the tetrahedrons allowed for a theoretical density of the GeO_2, GeS_2, and SnO_2 tetrahedrons to be determined which were then normalized by the SiO_2 tetrahedron density and multiplied by the bulk crystalline SiO_2 density to give a semi-empirical density for the crystalline tetrahedral networks (Table 4.1). Even though the as deposited films were amorphous, the crystalline α quartz SiO_2 density was used for

comparison purposes, as more density data existed for the crystalline quartz phases of GeO_2 and GeS_2 materials.

The model was in close agreement with literature values for bulk crystalline SiO_2, GeO_2, and GeS_2 and predicted a crystalline 4-coordinate SnO_2 density of approximately 80% of the rutile phase.[6] When the model incorporated the lower amorphous SiO_2 density reported for ALD SiO_2 films, a predicted amorphous SnO_2 density of 4.5-5 g/cc was achieved.[100] The predicted amorphous SnO_2 density and the experimentally deposited ALD film density are within ~80% agreement, suggesting that a 4-coordinate SnO_2 is a possible explanation for the observed decrease in density of SnO_2 deposited on zinc oxide.

A four-coordinate phase of SnO_2 may result from the ozonolysis of the tin alkyl bond. The tetraethyltin is initially 4-coordinate to begin with and it has been reported that two equivalents of ozone are required to replace an alkyl zinc bond with a hydroxide.[26] If a similar mechanism occurs with tetraethyltin, the 4 ethyl ligands would be replaced with 4 hydroxide ligands resulting in an initial 4-coordinate tin hydroxide. The 4-coordinate tin oxide could grow to a threshold thickness before a relaxation occurs to the rutile phase. This would explain the observed initial decrease in film density as tin oxide composition is increased followed by a reversal in that trend as the tin oxide concentration passes 40% (Figure 4.5).

The XRD patterns of as deposited and mild annealed films at 450 °C overnight revealed amorphous films with a slight hump at $2\theta = 33.6°$ (Figure 4.8). There is some conflict in the literature regarding the phase of crystalline $ZnSnO_3$ materials. It has been

reported that the ilmenite phase of $ZnSnO_3$ has been synthesized from an ion exchange reaction from Li_2SnO_3 and $ZnCl_2$.[4] A high pressure phase of $ZnSnO_3$ with a $LiNbO_3$ phase has also been reported with an XRD pattern that has significant overlap with the ilmenite phase.[101] In addition, theoretical research has been used to determine the most stable polymorph of $ZnSnO_3$ and both the ilmenite and LN phase were determined to be thermodynamically stable at zero pressure although the Helmholtz energy as a function of increasing temperature favored the ilmenite phase.[102]

The deposition of ZTO by ALD occurs at high temperature which should favor the formation of the ilmenite phase as opposed to the LN phase. Structural information of ALD deposited films becomes apparent after an 800 °C anneal for 1.5 h indicating ZnO wurtzite in low tin concentrations and SnO_2 rutile in high tin concentrations (Figure 4.8). A willemite phase Zn_2SiO_4 or possibly Zn_2SnO_4 also appears present in all ZTO films. The spinel Zn_2SnO_4 phase does have a strong reflection at 41.684 2θ which was also observed as a miner peak in zinc rich films. No significant reflections could be assigned to illmenite $ZnSnO_3$ except for the peak at 34° 2θ which also has significant overlap with spinel Zn_2SnO_4, rutile SnO_2, ZnO wurtzite and willemite.

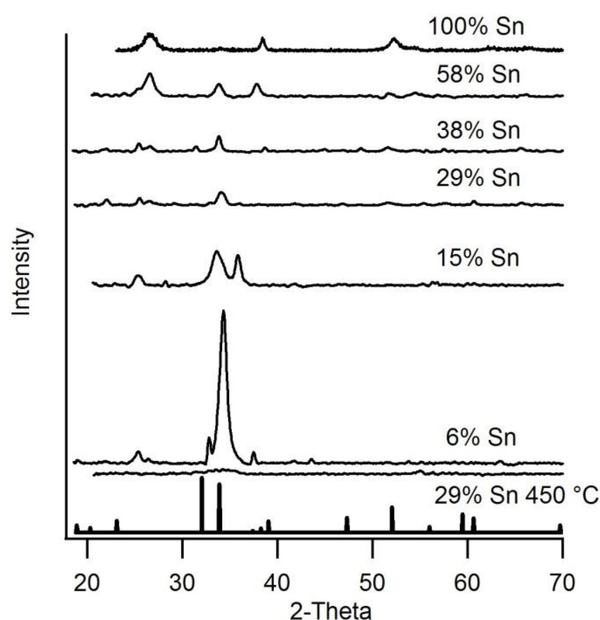

Figure 4.8 X-ray diffraction of ZTO films from 3:1 TET/O_3 to DEZ/O_3 to 8:1 TET/O3 to DEZ/O_3 including an annealed SnO_2 film and a 450 °C annealed 4:1 TET/O3 to DEZ/O_3. In addition to the XRD patterns, the Ilmenite $ZnSnO_3$ (PDF 52-1381) is included on the x-axis.[4]

Zinc oxide has XRD reflections at 36.25, 34.42, and 31.77 degrees 2θ which can be observed in zinc rich films corresponding to 6% Sn/(Sn+Zn).

The XRD reflections that overlap with the SnO_2 rutile phase at 26.14 , 38.42, and 52.3 degrees 2θ are most likely tin oxide because the peak intensities at these values of 2θ increase in intensity as the films increase in tin concentration. The XRD results of annealed ZTO films with compositions corresponding to $ZnSnO_3$ indicate a mixed metal oxide of Zincite (ZnO), rutile (SnO_2), and a willemite phase (Zn_2SiO_4) which could be an

artifact of annealing the ZnO material on silicon, or it could potentially be a ZTO phase where Sn could hypothetically substitute for Si producing a willemite phase ZTO material.[103] The following table assigns peak intensities in 38% Sn/(Sn+Zn) annealed films with corresponding PDF files of the aforementioned phases. 5305143403

Table 4.2 2-Theta values of 38% Sn/(Sn+Zn) correlated to various material phases of zinc oxide, tin oxide and zinc silicate.

Willemite Zn_2SiO_4 PDF 8-0492	Wurtzite ZnO PDF 36-1451	Rutile SnO_2 PDF 46-1088	38%Sn
22.0608			22.10
25.5318			25.46
		26.579	26.62
31.5434	31.770		31.42
34.0086	34.422		33.86
38.8181		37.769	38.70
44.9971			44.98
48.9524			48.82
		51.756	51.66
57.6134			57.54
65.6766			65.62

As deposited ZTO films showed high resistivity (2.2 Ω•cm) which was mainly a result of low mobility (4.1 $cm^2V^{-1}s^{-1}$), but also lower carrier concentrations ($6.8x10^{17}/cm^3$) than similar films that were processed at 450 °C for 12h. Hall measurements performed on 450 °C annealed ZTO films indicated carrier concentration improved slightly with increasing tin concentration. Film carrier concentrations for ZTO films were between 7 x 10^{17} and 3 x 10^{18} carriers/cm^3 for films with a 0.2 to 0.3 Sn/(Sn+Zn) ratio. The trend showed an exponential increase in carrier concentration

reaching a maximum of 1 x 10^{21} carriers/cm^3 for pure SnO_2 corresponding to a Sn/(Sn+Zn) ratio of 1(Figure 4.9).

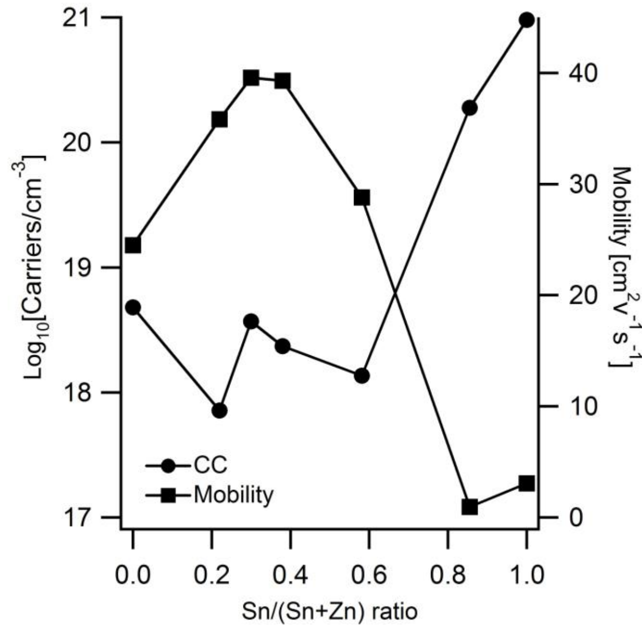

Figure 4.9 Carrier concentration and electron mobility as a function of film tin concentration in 450 °C annealed ZTO films.

Electron mobility followed a similar trend where mobilites increased from 36 to 39 $cm^2V^{-1}s^{-1}$ for Sn/(Sn+Zn) ratios ranging from 0.2 to 0.4, however the mobility dropped to 3 $cm^2V^{-1}s^{-1}$ as the stoichiometry approached SnO_2. The large electron mobility in amorphous ZTO films has been observed before and has been theorized to be a result of spherically symmetric ns orbitals from the heavy metal cation elements which form the conduction band resulting in more overlap with adjacent orbitals.[12]

The ZTO film resistivity also decreases with increasing tin concentration resulting in films with resistivities in the $5x10^{-2}$ Ω•cm for Sn/(Sn+Zn) ratios of 0.3. This trend continues to the pure SnO_2 films which have the lowest resistivity approximately $2x10^{-3}$ Ω•cm. The increase in carrier concentration for the SnO_2 film more than compensates for the lower electron mobility resulting in overall more conductive films in the pure SnO2 material when compared to the ZTO films.

The optical properties of the films were determined from UV-Vis transmittance spectrum of 30 nm ZTO films which were then plotted as $[\alpha h\nu]^2$ vs photon energy in eV (Figure 4.10). The absorption coefficient (α) was determined using –ln(%T) x 1/d where T was transmittance and d was thickness.[104] The intersection of the constant slope line with the x-axis determined the direct band to band transition. The Tauc plot indicated that the films are transparent with bandgaps that increase as the SnO_2 concentration is increased. The bandgaps for films corresponding to 37% Sn had a 3.40 eV band gap which increased to 3.77 eV for films corresponding to 85% tin. The results from the Tauc plot indicate that these ZTO films are wide bandgap materials and are within the expected bandgaps for the pure materials 3.23 eV for ZnO, 3.95 eV for SnO_2 films and 3.75 eV for a mixed metal oxide film of 25% Zn:Sn .[105,106]

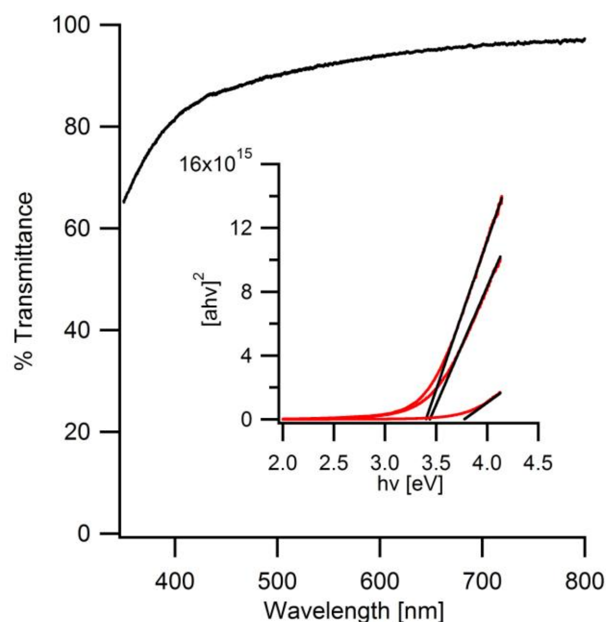

Figure 4.10 Optical transmission of 58 at.% Sn ZTO film Tauc plot (inset) for bandgap as a function of film composition 3.40, 3.42, 3.77 eV for 37, 58, 85 at.% tin.

4.4.3 Fabrication of a Tunnel Junction Device

A tunnel junction was fabricated using a device stack of Au/AZO/ZTO/Cu_2O/Au on ITO-on-Glass substrate. The ITO/glass is more representative of the rough surface of a thin film absorber layer and the AZO is a likely solar window layer simulator which was deposited by ALD for 110nm. ZTO was deposited with composition corresponding to 50.2 at. % tin involving 27 super cycles of a 8:1 pulse sequence of tin and zinc on masked AZO resulting in 40 nm thick ZTO films.[107] Cuprous oxide was deposited on top

of the ZTO material using RF magnetron sputtering of a ceramic Cu_2O target. Power was 200W for one hour of deposition with substrate-to-target separation approximately 12.5cm, argon flow at 40sccm, chamber pressure of 5mTorr, and substrate heated at 300°C. The resulting Cu_2O thickness was 220nm. Gold contacts were deposited for a 3 point measurement on the stack for IV characterization using a separate mask (Figure 4.11). The resulting IV profile was linear with voltage sweeping +/- 2v. The linear profile indicates ohmic behavior suggesting a tunnel current is the dominant form of carrier transport in the stack.

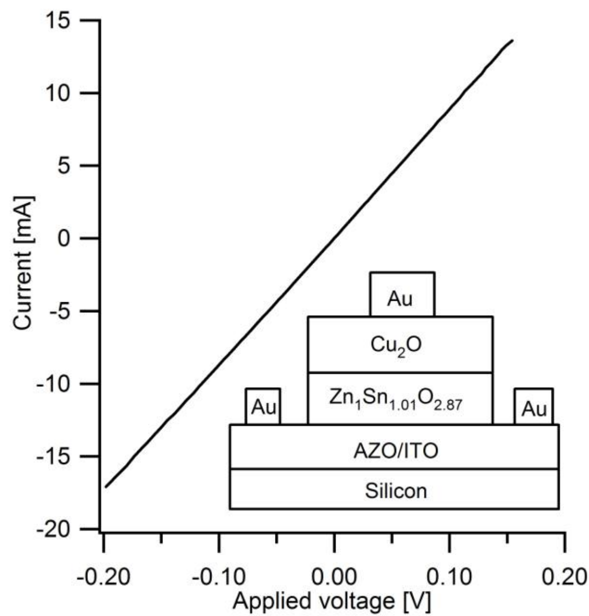

Figure 4.11 Current vs. Voltage (IV) profile of a tunnel junction device composed of sputtered Cu_2O and ALD deposited $ZnSnO_3$ on an AZO/ITO coated glass substrate.

4.5 Conclusions

Both tin oxide and zinc tin oxide have been deposited using a novel TET/O_3 precursor. The deposition of tin oxide within the ALD window appears to have self limiting growth equivalent to 0.2nm/cycle. A reduction in deposition rate and a reduction in SnO_2 density was observed when depositing the SnO_2 on Zinc oxide for the ZTO material. A possible explanation for the observed low growth rate and low density is a kinetically trapped 4-coordinate tin oxide sandwiched between two ZnO layers.

Computational chemistry was employed to determine the density of an amorphous network of 4-coordinate SnO_2 film by employing known 4-coordinate structures of SiO_2, GeO_2 and GeS_2. The predicted density from the computations suggests that the 4-coordinate tin oxide would have a 20% lower density than the bulk rutile SnO_2 which gives reasonable agreement to our observed film densities. Structural characteristics from XRD show amorphous films as deposited which remain amorphous up to 450 °C. Further anneals up to 800 °C indicate mixed metal oxides of ZnO and SnO_2 with a willemite phase of Zn_2SiO_4, with a possibility of tin substituting for silicon creating a willemite Zn_2SnO_4 material.

The ZTO materials showed high optical transmission beyond 400nm and electrical properties showed high electron mobility and 10^{18} carrier concentrations which were indicative of TCO type films. A tunnel junction device was constructed using the ZTO film and a sputtered cuprous oxide which showed ohmic behavior indicative of a tunnel current. These devices can be applied as the tunnel junction material in

multijunction solar cells. Further applications of these materials also exist anywhere optically transparent devices are required.

4.6 Acknowledgements

Minnesota supercomputing institute, Greg Haugstad (University of Minnesota characterization facility), and the DOE SunShot initiative for funding

CHAPTER FIVE

Alkyl Tin Precursor Development for Tin Oxide Atomic Layer Deposition

5.1 Introduction

Tin oxide is an important IV-VI transparent conducting oxide (TCO) and has applications in the electronic industry for gas sensing and liquid crystal displays.[90, 107] The high optical transmittance of tin oxide is a result of its wide bandgap between 3.8 and 4.2 eV.[89] In addition to its large bandgap, un-doped SnO_2 films typically have low resistivity in the 1-5 x 10^{-3} Ω•cm range.[98] Both the optical and electrical properties of tin oxide make the material suitable for constructing optoelectronic devices.

Tin oxide films have been deposited by various techniques including sputtering, chemical vapor deposition (CVD), atomic layer deposition (ALD), and evaporation.[33, 98, 108] In both CVD and ALD, chemical precursors are used to deposit the tin oxide in a reactor. The ALD process has some benefits over CVD in that it is a self-limiting process where the oxygen source and precursor are separated in time, resulting in conformal coverage of the substrate.[14] For CVD and in particular for ALD, precursor chemistry can be challenging and a significant focus is placed on developing new precursors for different processes.

Precursor design has primarily been performed through experimentation by exploring different ligands that bind to the tin metal and provide adequate reactivity and volatility. For tin oxide deposition, ligands are typically amino derivatives, alkyl groups, or halides.[29, 30, 99] Theoretical models utilizing density functional theory (DFT) for understanding the fundamental reaction chemistry for ALD precursors are being developed to aid in precursor design.[26, 109] The DFT models, when used in tandem with

experimental processes, can provide mechanistic insight which is beneficial for understanding the deposition process and modifying precursors or surfaces.

5.2 Experimental

Potential tin ALD precursors, tetramethyltin ($SnMe_4$ 95%), tributyltinchloride ($SnBu_3Cl$ 96%), tributyltinhydride ($SnBu_3H$ 97%), and tetraethyltin ($SnEt_4$ 97%) were purchase from Sigma Aldrich. Diethyl zinc ($ZnEt_2$, Sigma Aldrich) was also utilized as a zinc oxide source for testing substrate effects on SnO_X deposition. In a fume hood, the precursors were loaded in 5 ml quantities into 50 ml stainless steel precursor vessels resulting in approximately 45 ml of headspace for the precursor's vapor pressure to saturate.

The precursor vessels were then attached to the valve assembly of the custom built hot wall ALD reactor. The precursors had sufficient vapor pressure that they could be introduced into the reactor under vacuum without the aid of a carrier gas. The vapor pressure of the precursor was maintained by using a temperature bath surrounding the precursor vessel. For the $SnMe_4$ precursor, an ethanol bath cooled to -40 to -45 °C by a cryocool™ chiller was used to maintain the vapor pressure. The $SnBu_3Cl$ and $SnBu_3H$ were heated by a stirred oil bath to 65 °C by using a hot wire and variac to provide the necessary temperature. In order to prevent condensation of the $SnBu_3Cl$ and $SnBu_3H$ en route to the reactor, all lines and valves were wrapped with heating tape and heated with a variac to between 60 and 80 °C.

Ozone was utilized as the oxygen source for all depositions and was provided as 2-4% O_3 in O_2 by a Dwyer ozone generator supplied by industrial grade oxygen. The ozone was generated in situ during depositions in a fume hood and carried to the reactor valve assembly via PTFE tubing. During an ozone pulse, the reactor pressure was measured to increase from a base pressure of 30 mtorr to 1 torr. All ozone and reactor effluent were continually exhausted through the lab air handling system.

High purity nitrogen 99.999% was used as the purge gas separating the precursor and ozone pulses. The nitrogen purge was metered at 100 sccm through a mass flow controller. During purge, the base pressure of the reactor increased by approximately 1 torr.

Postage stamp pieces (1 cm^2) of silicon (Si) and soda-lime glass (SLG) were used as substrates for the deposition. The sample prep consisted of soaking the Si in piranha solution (70% H_2SO_4 diluted to 100% with H_2O_2 (30%)) for 1h, followed by a DI H_2O rinse, a 10 min 30% HF soak, and a final DI H_2O rinse. The SLG samples were rinsed under ethanol and dried under a nitrogen stream. Both the SLG and Si samples were attached to a different SLG slide by furnace tape which served as a sample holder. After sample prep, the substrates were immediately loaded into the hot zone of the ALD reactor and subsequently pumped down to vacuum.

The characterization of all films included using a J. G. Woollam VASE® spectroscopic ellipsometer (SE) for providing film thickness as well as index of refraction data. Rutherford backscattering (RBS) spectrometry using a MAS 1700 pelletron tandem ion accelerator (5SDH) equipped with charge exchange RF plasma source by National

Electrostatics Corporation (NEC) was used for the elemental analysis using integration and Quark© and SIMNRA© fitting software. Film structure was determined by XRD using a Bruker-AXS Microdiffractometer. Optical properties were measured with an Ocean Optics UV-Vis spectrometer, and electrical resistivity was measured by 4-point probe.

5.3 Results and Discussion

5.3.1 ALD of SnO_2 with $SnMe_4$ and Ozone

Tetramethyltin has been used as a CVD precursor with O_2 gas for depositing SnO_2 films, as well as an ALD precursor with N_2O_4 oxidant gas, however the deposition process of $SnMe_4$ with O_3 has not been previously reported.[29, 108] The deposition temperatures for the CVD and ALD process were reported to be between 350 and 420 °C, which was chosen as the initial temperature regime to study the $SnMe_4$ and O_3 chemistry.

Tetramethyltin was introduced into the ALD reactor with a hot zone temperature of 350 °C and exposure times varying from 1 s to 6 s. The ALD sequence at 350 °C comprised a variable $SnMe_4$ exposure, 8 s N_2 purge, and 8 s O_3 pulse. At 350 °C, the thickness per cycle (TPC) as a function of precursor pulse time was found to plateau to 0.1 nm/cycle between 2 s and 3 s. The plateau was indicative of a self-limiting ALD process where the substrate surface became saturated beyond a 2 s $SnMe_4$ pulse. The O_3

pulse times were varied at 2.5 s, 10 s, and 16 s at 380 °C to determine the O_3 exposure's affect on film TPC with no significant effect on TPC observed (Figure 5.1).

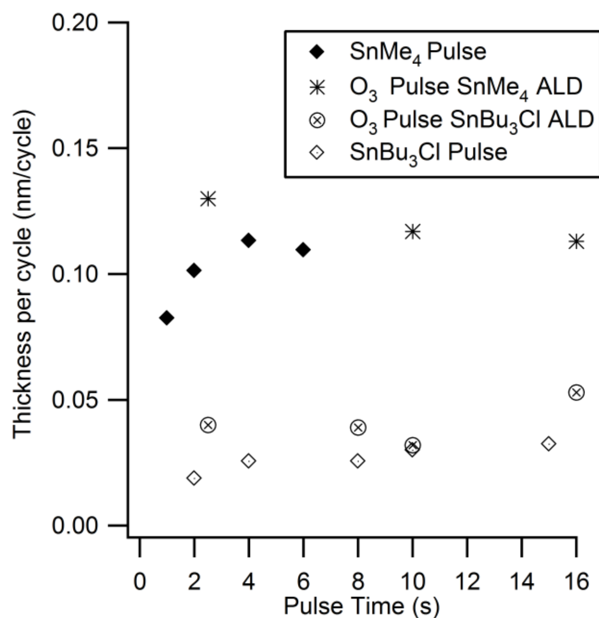

Figure 5.1 Thickness per cycle (TPC) of SnO_X deposition as a function of increasing O_3 and $SnMe_4$ exposure times at 350 and 380 °C respectively and SnO_X TPC as a function of increasing O_3 and $SnBu_3Cl$ exposure at 290 °C.

The characterization of the ALD window for $SnMe_4$ and O_3 was performed by measuring the TPC as a function of deposition temperature. A region of near constant TPC was found to exist between 330 °C and 400 °C. Beyond this plateau, the TPC experienced a significant increase suggestive of a CVD type process (Figure 5.2).

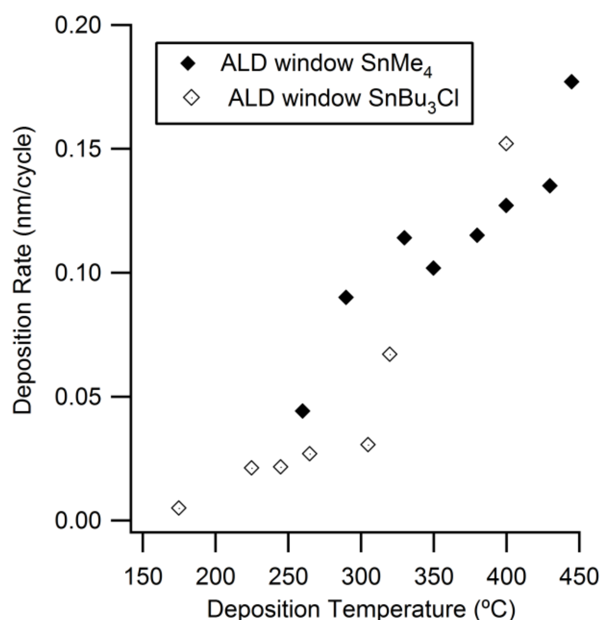

Figure 5.2 ALD window for $SnMe_4$ and O_3 SnO_X ALD and $SnBu_3Cl$ and O_3 SnO_X ALD. Precursor exposure times were 2 s ($SnMe_4$), and 15 s ($SnBu_3Cl$)

The ALD of $SnMe_4$ with O_3 differed from the ALD of $SnMe_4$ with N_2O_4 in that the observed TPC for O_3 was approximately half that reported for the N_2O_4 precursor. In addition, the ALD window of uniform deposition was observed to be both slightly larger and cooler in the O_3 case than the N_2O_4 oxidant.[29] The most surprising result of using O_3 in place of N_2O_4 seems to be the reduced TPC ratio. The implication suggests that an ozonated surface of the SnO_2 possesses fewer hydroxyl groups or active sites than the surface exposed to N_2O_4, which reduces the density of chemisorbed $SnMe_4$ molecules.

Elemental analysis of $SnMe_4/O_3$ films on Si substrates was performed by RBS and indicated large oxygen to tin ratios (approximately 5 to 1) in thinner films (20 nm)

deposited at lower temperatures (230-320 °C). The large amount of oxygen present in these films is indicative of a SiO_2 interface between the substrate and the SnO_x film. This SiO_2 interface is believed to be a result of redox chemistry at the Si SnO_2 interface, where SiO_2 is thermodynamically preferred over tin dioxide.[110] The SiO_2 interface was determined to be approximately 12 nm thick using Quark © RBS fitting software and the SE measurements for total thickness. The SnO_2 film was also observed to increase in density with increasing deposition temperatures as well as total film thickness as measured by the film's refractive index.

The $SnMe_4$ / O_3 precursor system was also tested for substrate selectivity. It had been observed that both $SnMe_4$ and $SnEt_4$ with N_2O_4 had TPCs that were suppressed on substrates which could not readily be reduced such as Al_2O_3 and SiO_2, but the TPC was unaffected on SnO_2, TiO_2 and CrO_2 substrates.[29]

The $SnMe_4/O_3$ ALD process was tested for the substrate TPC suppression affect by depositing alternating layers of ZnO and SnO_2 to form a nanolaminate. The supercycle for depositing nanolaminate ZTO comprised of one deposition of ZnO followed by n depositions of tin oxide. The ZTO films corresponding to a 1:1 ZnO:SnO_2 and a 1:2 ZnO:SnO_2 supercycle were found to have low tin concentrations of 6 and 11 atomic % tin for the 1:1 and 1:2 films. The atomic percent of Sn in the ZTO films deposited with $SnMe_4$ as a function of tin cycles agrees closely with the atomic percent of Sn deposited using $SnEt_4$ for the 1:1 and 1:2 films (Chapter 4). The agreement in ZTO film composition between the two precursors suggests that similar substrate suppression in TPC occurs with the $SnMe_4$ precursor.

As deposited films were found to be polycrystalline rutile SnO_2 phase with no preferred orientation (Figure 5.3). The as deposited crystallinity of SnO_2 films deposited by $SnMe_4$ was in contrast to SnO_2 films deposited by $SnEt_4$ and $SnBu_3Cl$ with ozone both of which were amorphous. The crystallinity of SnO_2 deposited using $SnMe_4$ precursor has been observed in films deposited via CVD and may be a result of the molecule's smaller steric bulk allowing for closer packing during adsorption as well as higher deposition temperature.[108]

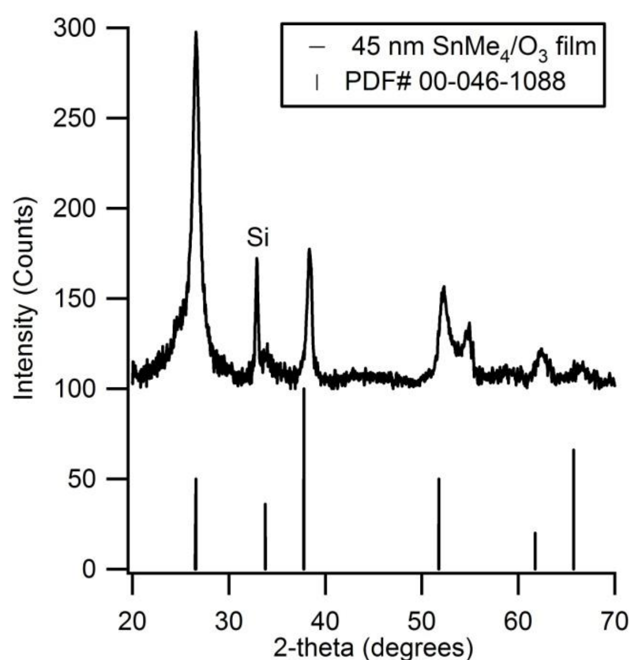

Figure 5.3 X-ray diffraction of as deposited $SnMe_4/O_3$ ALD film at 380 °C compared to a reference CVD film made from $SnCl_2$ and O_2 precursors.[1]

Characterization of the opto-electronic properties of films grown within the processing window indicated that the films were transparent between 400 to 900 nm and had conductivities within the reported range for SnO_2 films Table 5.1.[33, 111] The optical bandgaps were determined from tauc plots of $(\alpha h\nu)^2$ vs $h\nu$ and extrapolating the linear region. The absorption coefficient (α) was determined by the equation –ln(%T) x 1/d where %T was percent transmittance and d was film thickness.[103]

Table 5.1 Opto-electronic properties of SnO_X films deposited using $SnMe_4$ and $SnBu_3Cl$ precursors with ozone.

Precursor	Temperature (°C)	Film Thickness (nm)	Specific Resistance (Ω•cm)	Optical bandgap (eV)
$SnBu_3Cl$	290	21.3	1.69×10^{-2}	3.52
$SnBu_3Cl$	290	20.7	6.31×10^{-2}	3.59
$SnMe_4$	380	45.0	2.12×10^{-1}	3.63
$SnMe_4$	400	23.3	3.33×10^{-2}	3.69

5.3.2 ALD of SnO_2 with $SnBu_3Cl$, $SnBu_3H$ and Ozone

Tributyltinchloride has not previously been used as an ALD precursor. The $SnBu_3Cl$ is of interest as it is a modified alkyltin derivative and a hybrid between the

alkyl tin precursors and the tin halide precursors which have been used in ALD for depositing tin oxide films.[29, 112] The chloride functionality presented an alternative ligand for Brønsted elimination between the precursor and surface hydroxyl of zinc oxide.

Tributyltinchloride was analyzed for self-limiting ALD deposition by varying the precursor dosage to the substrate from 1 s to 25 s at a deposition temperature of 290 °C (Figure 5.1). The TPC was observed to plateau beyond 10 s at this temperature. In addition, the hot zone temperature was varied between 200 and 425 °C, where a region of uniform TPC was observed between 250 and 325 °C corresponding to the ALD window for the $SnBu_3Cl$ precursor (Figure 5.2). The effect of ozone exposure on the TPC was also explored with no significant increase in film TPC observed beyond 8 s (Figure 5.1). At an ozone exposure of 2.5 s, the observed index of refraction decreased markedly from 1.7 to 1.4, indicative of a lower density film, however the TPC did not decrease substantially at this lower O_3 exposure.

The maximum TPC observed for the $SnBu_3Cl$ corresponded to 0.05 nm/cycle, which was consistent with TPCs of tin halides with hydrogen peroxide under similar conditions.[112, 113] The similar TPC of the $SnBu_3Cl$ within the ALD window of the tin halides implies that the chloride functional group of the $SnBu_3Cl$, rather than the butyl groups, were interacting with the hydroxylated surface of the substrate eliminating HCl and forming a surface bound tributyltin.

As the deposition temperature increased beyond the ALD window, a marked increase in the TPC was observed for the $SnBu_3Cl$ precursor (Figure 5.2). This marked

increase in TPC has not been observed for tin halides and the TPC has usually been observed to decrease with increasing deposition temperature, corresponding to dehydration of hydroxyl sites.[112] At these higher temperatures, pyrolysis of the butyl ligands of the $SnBu_3Cl$ precursor is likely, resulting in a CVD type deposition.[114] The deposition at temperatures beyond the ALD window was also marked by rougher films as measured by AFM corresponding to RMS values of 1.5 nm as opposed to 0.3 nm for films within the ALD window.

The $SnBu_3Cl$ precursor was tested for substrate suppression effects by depositing a nanolaminate ZTO film. The hypothesis for using the $SnBu_3Cl$ was to provide a different functional group, the chloride, which would interact with zinc hydroxyl sites differently than the alkyl ligands. Super cycles consisting of 1:1 $ZnO:SnO_2$ were deposited with the $SnBu_3Cl$ ligand. Elemental analysis from RBS indicated that the atomic % Sn incorporated in the ZTO films was 0.7% for the 1:1 case. The atomic % Sn incorporated in the ZTO film was approximately an order of magnitude less than the $SnMe_4$ precursor. Adjusting for differences in ALD tin oxide TPCs between the $SnBu_3Cl$ and $SnMe_4$ precursor, the chloride functional group appeared to adversely affect the adsorption of $SnBu_3Cl$ on the ZnO surface when compared to the $SnMe_4$ and $SnEt_4$ precursors (Chapter 4).

Characterization of the opto-electronic properties of films grown within the ALD window indicated that the films were transparent between 400 to 900 nm and had conductivities within the reported range for SnO_2 films Table 5.1.[33, 111]

The $SnBu_3H$ was also tested for ALD properties, however it was found to decompose at temperatures in excess of 65 °C consistent with the known chemistry of tin hydrides.[115] Although tin oxide films were deposited, the films did not appear to be self limiting and the subsequent contamination of the heated ALD reactor lines prevented further research into this precursor.

5.3.3 Reduced Temperature ALD of $SnEt_4$ and Ozone

The ALD of SnO_2 with alkyltin precursors has been hypothesized to proceed via a pyrolysis of the alkyltin bond and formation of radical Sn species that are chemisorbed onto the substrate surface causing a reduction in the substrate's oxidation state from IV to II.[29] This mechanism was proposed to explain the substrate suppression effect observed when depositing SnO_2 on different substrates. The pyrolysis mechanism could be plausible as a result of the high deposition temperatures of 250-290 °C and 400-450 °C for the $SnEt_4$ and $SnMe_4$ precursors, however, most MO_x ALD has been observed to be hydroxyl promoted and it is possible that observed substrate effects correlate to differences in hydroxyl surface sites rather than redox reactions in the substrate.[116, 117]

To test this hypothesis, ALD of SnO_2 and ZTO using $SnEt_4$ and O_3 were attempted at significantly reduced temperatures in order to starve the pyrolysis mechanism of thermal energy. The thermal decomposition at 5 torr of $SnEt_4$ has been reported to occur at approximately 300 °C, and slowly (over 40 minutes) at 270 °C in the presence of oxygen.[114] A temperature of 200 °C was chosen for the low temperature

depositions as it appeared to be well below reported decomposition temperatures of the $SnEt_4$ precursor.

To compensate for the reduced thermal energy, the concentration of $SnEt_4$ was greatly increased during the deposition by throttling the vacuum pump valve. For these depositions, the pressure of $SnEt_4$ in the reactor was measured to be 300 mtorr, a factor of 4-5 increase over the un-throttled reactor configuration. In addition, long N_2 purge cycles consisting of 30 s were used to separate the $SnEt_4$ and O_3 pulses and an additional 10 s of vacuum was used after the O_3 pulse to separate the two precursors preventing CVD type reactions.

Low temperature SnO_2 was deposited using $SnEt_4$ and O_3 with deposition temperatures of 200 °C. The TPC of low temperature SnO_X was determined using SE with a Cauchy model incorporating 4 nm SiO_2 and dividing by the total number of cycles. The TPC for the throttled configuration was determined to be 0.24 nm/cycle, nearly identical to the TPC observed at 300 °C for the $SnEt_4$ and O_3 in the un-choked configuration (Table 5.2). An un-choked ALD run was also performed at 200 °C resulting in a TPC of approximately 0.01 nm/cycle which highlighted the importance of increasing the $SnEt_4$ concentration to compensate for the reduced thermal energy. Elemental analysis by RBS using oxygen enhancement at 3.065 MeV indicated a film stoichiometry of $SnO_{2.3}$.

Table 5.2 Low temperature deposition of SnO_2 and ZTO.

Film	**SnOx**	**SnOx**	**ZTO 1:1**	**ZTO 2:1**
$SnEt_4$ precursor pressure (mtorr)	300	70	300	300
Deposition temperature (°C)	200	200	200	200
ALD cycles	100	200	50	30
Film thickness (nm)	24.8	2.7	13.3	9.3
Film stoichiometry	$SnO_{2.3}$	N/A	$ZnSn_{0.13}O_{0.76}$	$ZnSn_{0.2}O_{0.75}$

Additional ZTO films were deposited at 200 °C using sequential deposition of ZnO and SnO_2 corresponding to supercycles (SC) of 1:1 and 2:1 N_{Sn}:N_{Zn} deposition cycles. These nanolaminate films were deposited to ascertain the effect of reduced temperature on the suppression affect observed for SnO_2 deposition on ZnO. The supercycle consisted of N(30 s N_2, 10 s $SnEt_4$, 30 s N_2, 15 s O_3, vacuum 10 s):1(30 s N_2, 8 s $ZnEt_2$, 30 s N_2, 15 s O_3, 10 s vacuum) where "N" was varied. A total of 50 and 30 supercycles were deposited for the 1:1 and 2:1 films.

The ZTO films were characterized by SE and RBS elemental analysis at 3.065 MeV and were found to be 13 nm thick for the 1:1 film with 11.6 atomic % Sn (Sn/(Sn+Zn) and 9 nm thick for the 1:2 film with 17 atomic % tin. The oxygen content for the ZTO appeared lower than expected based on the composition of the much thicker

SnOx film deposited at 200 °C and reported values for ZnO ALD with ozone, however the films are thin such that the signal to noise for the oxygen is quite low, likely leading to an underreported oxygen content (Table 5.2).[27]

From the low concentration of Sn in the ZTO, it was observed that the films showed similar substrate suppression of SnO_2 deposition on ZnO at the reduced temperature. The observation that $SnEt_4/O_3$ ALD is suppressed on ZnO at both 300 °C and 200 °C suggests that a pyrolysis mechanism and corresponding redox of the substrate is not responsible for the observed film growth. The suppression behavior does, however, appear to be related to a surface adsorption step which is less favorable on some substrates than others.

5.3.4 Suppression of $SnEt_4$ in ternary oxides

Curvature in the stoichiometry vs. number of precursor cycles per supercycle ($M^1/(M^1+M^2)$ vs $C_1/(C_1+C_2)$) has been observed in ALD deposited $M^1_XM^2_{1-X}O_Y$ ternary oxides.[118] A simple combustion model, as well as a Brønsted elimination model have been developed which suggest that the cation charge of the precursor is instrumental in determining the amount of curvature in the composition vs cycles plot.[118]

The combustion model assumes that precursors molecularly adsorb onto the surface of a film and the ligands are combusted by an oxygen source following the purge pulse. The limit of precursor adsorption occurs when the surface is saturated in precursor ligands the surface saturation is defined as θ_{ligand}. To determine how many metal atoms

can be adsorbed onto a surface during the precursor pulse, the θ_{ligand} is divided by the metal cation charge (q) so that the number of metal atoms incorporated in a pulse is equal to θ_{ligand}/q. When this model is utilized for ternary metal oxides, the composition of the film $M^1/(M^1+M^2)$ can be determined from a ratio of θ_{ligand}/q of the two precursors where *n* is the number of precursor pulses, and *q* is the cation charge of the precursors (5.1). If the ligands are the same, equation (5.1) simplifies to be equal to just the ratio of precursor pulses (*n*) to precursor cation charge (*q*).

$$\frac{M^1}{(M^1+M^2)} = \frac{n_1 x(\theta_{ligand}/q_1)}{\left[\left(n_1 x\left(\theta_{ligand}/q_1\right)\right) + \left(n_2 x\left(\theta_{ligand}/q_2\right)\right)\right]} \tag{5.1}$$

The Brønsted elimination model assumes that a surface hydroxyl is required to adsorb the precursor and a hydrogen transfer event occurs between the ligand and the hydroxide resulting in the elimination of a protonated ligand from the precursor and formation of a precursor-oxygen bond. The combustion model is reformulated to include a ratio of active hydroxyls (*f*) where the film stoichiometry is obtained from equation (5.2). The Brønsted elimination model can be fit to the experimental data by varying f_1 and f_2 using a least squares method.

$$\frac{M^1}{(M^1+M^2)} = \frac{n_1 x(\theta_{ligand}/q_1)x(f_1+1)}{\left[\left(n_1 x\left(\theta_{ligand}/q_1\right)x(f_1+1)\right) + \left(n_2 x\left(\theta_{ligand}/q_2\right)x(f_2+1)\right)\right]} \tag{5.2}$$

Utilizing these models, both $SnEt_4$ and $Sn(NMe_2)_4$ have the same cation charge, both should have the same theoretical composition of tin in the ZTO for a given supercycle. When $SnEt_4$ is used in a 1:1 ZTO supercycle utilizing the same deposition parameters optimized for SnO_2 ALD, the concentration of Sn incorporated into the ZTO was 7-10 atomic%, significantly less than that obtained for $Sn(NMe_2)_4$ and the 33% predicted based on cation charge.[118, 119]

Increased $SnEt_4$ precursor pulses were used to increase the dosage of tin precursor to the ZnO surface in an attempt to find the maximum surface saturation of $SnEt_4$ precursor. It was found that in 1:1 (precursor pulse ratio) ZTO films that the TPC increased by a linear 0.041 Å/s during $SnEt_4$ exposure, saturating at a TPC of 0.4 nm/SC after a 64 s exposure (Figure 5.4).

The TPC of SnO_2 on ZnO using $SnEt_4$ was found to increase at a 460% slower rate than $SnEt_4$ on SnO_2 substrates for the same deposition temperature (chapter 4). Elemental analysis confirmed a 28 atomic % tin in the 64 s exposure which is in close agreement with ZTO films deposited utilizing 1 s exposures of $Sn(NMe_2)_4$ and the predicted value for tetravalent tin on divalent zinc.[119] It was, however, found that given enough time, the composition of the 1:1 ZTO film approaches the steady state composition as predicted suggesting that the ZnO surface has a higher kinetic barrier to $SnEt_4$ adsorption than the corresponding SnO_2 surface. In addition, $SnEt_4$ showed a significant reduction in deposition rate on ZnO (time required to achieve steady state TPC) when compared to the $Sn(NMe_2)_4$ precursor.

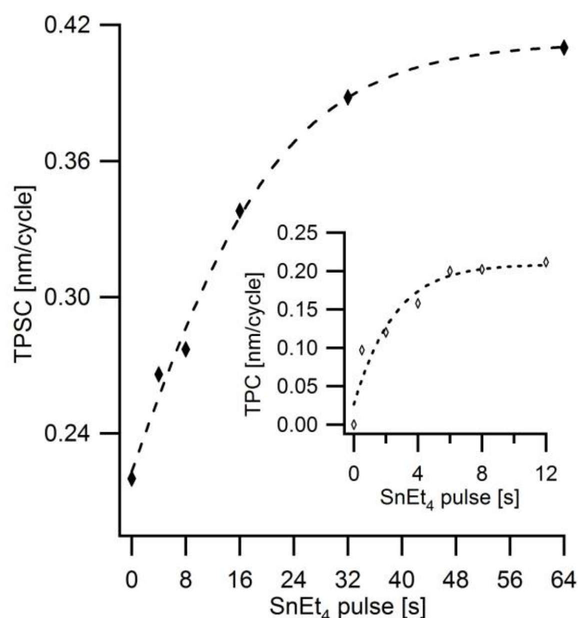

Figure 5.4 Thickness per supercycle (TPSC) and TPC comparison between SnO_2 deposited on itself and ZnO utilizing $SnEt_4$ and varying the precursor pulse time. Atomic % tin reported as a function of increasing $SnEt_4$ exposure on ZnO.

Zinc tin oxide films were also deposited under saturating $SnEt_4$ pulses (34 s) to determine if a combustion only mechanism or combustion and partial Brønsted elimination of the ethyl ligand correctly models the reaction of $SnEt_4$ with ZnO surface.[118] Films were deposited using supercycles corresponding to a 1:3, 1:1, 2:1, 3:1, 4:1 and 6:1 N_{Sn}:N_{Zn} exposure and characterized by RBS for elemental composition. A non-linear trend was established for the composition vs. supercycle implying a partial Brønsted elimination was an active pathway for $SnEt_4$ adsorption (Figure 5.5). The fraction of active hydroxyls on SnO_2 and ZnO (f) was varied using a least squares

method to obtain a fit to the experimental results and indicated that the ratio of $(f_{Sn}+1)/(f_{Zn}+1)$ was 0.56 implying that Sn ethyl ligands are less active toward Brønsted elimination than Zn ethyl ligands.

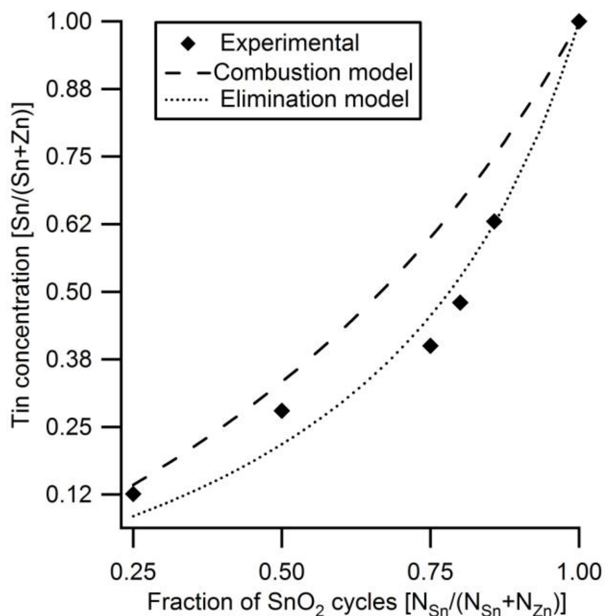

Figure 5.5 Composition of ZTO films as a function of Sn pulse ratio.The fits to the experimental data include a simple combustion model and a Brønsted elimination model with a $(f_{Sn}+1)/(f_{Zn}+1)$ ratio of 0.56.

5.3.5 Computational Studies of $SnEt_4$ with Ozone

To determine if hydroxide generation is possible for $SnEt_4/O_3$ chemistry, the interaction of $SnEt_4$ with O_3 was studied computationally using density functional theory

(DFT). Gaussian 09 with the M06 functional was chosen for modeling the organomettalic chemistry with a SDD basis set for the Sn atoms and 6-31+G(d,p) for the ligands and ozone atoms.[55, 56] The reaction coordinate for the interaction of $SnEt_4$ with O_3 was produced from geometry optimizations of stationary points and performing frequency calculations to obtain the Gibb's free energy contribution to the total molecular energy by computing the thermal contributions to 298.15 K molecular partition functions employing the ideal-gas (1 atm), rigid-rotator, harmonic-oscillator approximation.[64] Transition states were obtained by performing transition state searches followed by frequency calculations to obtain the imaginary frequency corresponding to the bond-breaking and bond-formation step as well as the Gibb's free energy contribution to the total energy.

Two reaction mechanisms were identified computationally for the interaction of ozone with the ethyl-tin bond. Both pathways were exergonic and the largest free energy activation barriers for both pathways were within 0.8 kcal/mol of each other suggesting that both pathways may be active routes for ozonolysis of tetraethyltin.

The ozonolysis reactions were modeled by using a triethyltinhydroxide ($SnEt_3OH$) as a chemisorbed $SnEt_4$ with the OH group approximating the surface metal oxide. The ozone interaction was than studied with each of the ethyl ligands (L_1-L_3) resulting in a final $Sn(OH)_4$ product.

The first ozonolysis mechanism was an identical reaction pathway as identified for the $ZnEt_2$ and O_3 interaction resulting in the insertion of ozone between the tin-ethyl bond forming an ethoxide intermediate (Figure 5.6).[26] A second equivalent of ozone

could then abstract a β-hydrogen from the ethoxide ligand resulting in the elimination of acetaldehyde and formation of the hydroxide functional group (Figure 5.7).

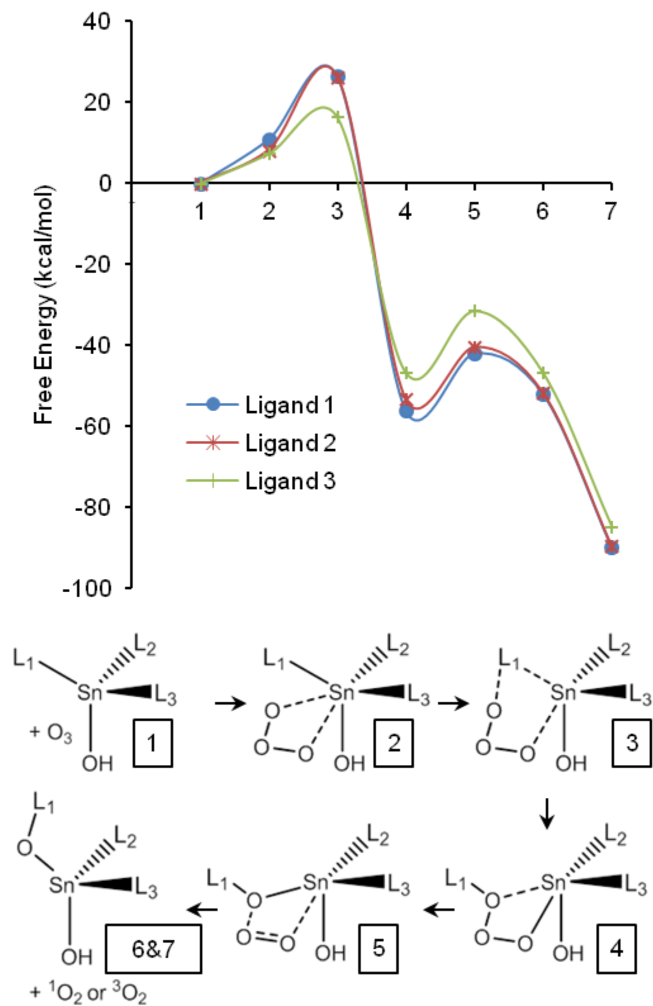

Figure 5.6 Mechanism 1. Reaction coordinate and scheme for first ozonolysis of an ethyltin ligand resulting in an ethoxide intermediate. The reaction coordinate follows the conversion of all ethyl ligands to their corresponding ethoxides.

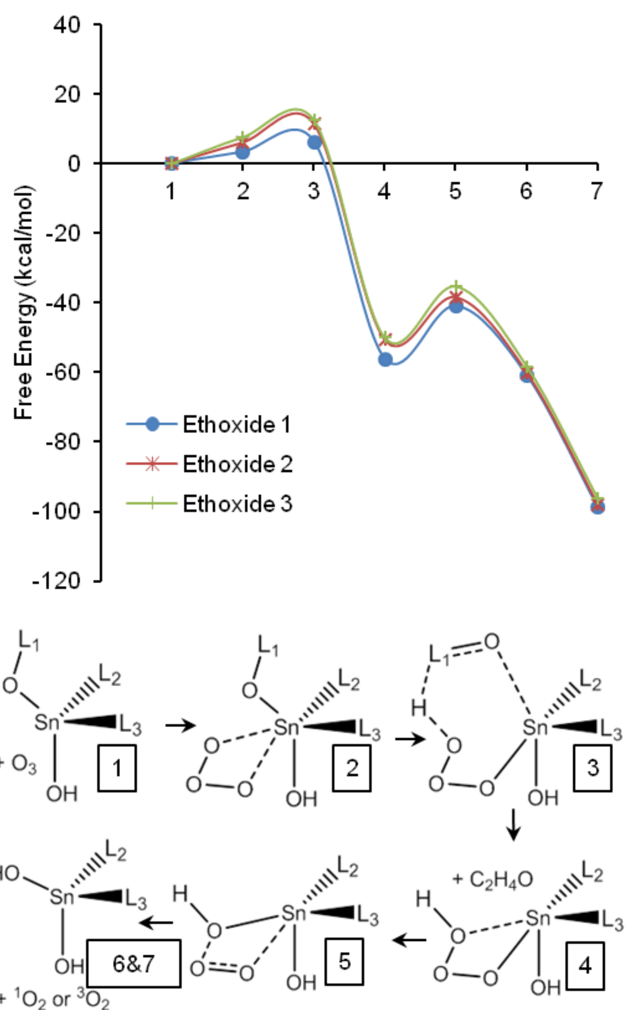

Figure 5.7 Mechanism 1. Reaction coordinate and scheme for second ozonolysis resulting in the elimination of acetaldehyde and formation of hydroxide functional group. The reaction coordinate follows the conversion of all ethoxides to their corresponding hydroxides.

In mechanism one, two equivalents of ozone are required per ethyl ligand to generate the hydroxide. The rate limiting step appeared to be the insertion of ozone

between the tin alkyl bond with a $\Delta G^{\ddagger}$ of 26.4 kcal/mol. Interestingly the activation barrier for the ozone insertion into the L_3 of the diethoxide tin hydroxide was 9.8 kcal/mol lower in energy than for either L_1 or L_2.

The second ozonolysis with the ethoxide groups would be facile in comparison as the activation barrier for acetaldehyde elimination was found to be 12.5 kcal/mol. In addition, the elimination of $^1O_2$ from the ethyltrioxide and hydrotrioxide were found to be approximately 15 kcal/mol which is slightly higher than $^1O_2$ elimination from similar trioxides attached to zinc.[26]

In mechanism two, ozone abstracted a hydrogen from the ethyl ligand resulting in the formation of a tin attached hydrotrioxide and elimination of ethylene (Figure 5.8). This hydrogen abstraction would be consistent with observed ozonolysis of organic molecules, where hydrogen abstractions from C-H bonds have been proposed as mechanisms, specifically in the ozonolysis of t-butanol resulting in butane-2-one.[120, 121]

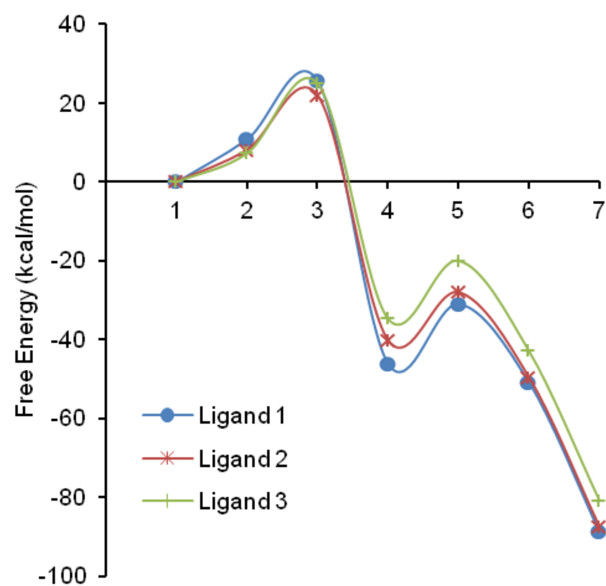

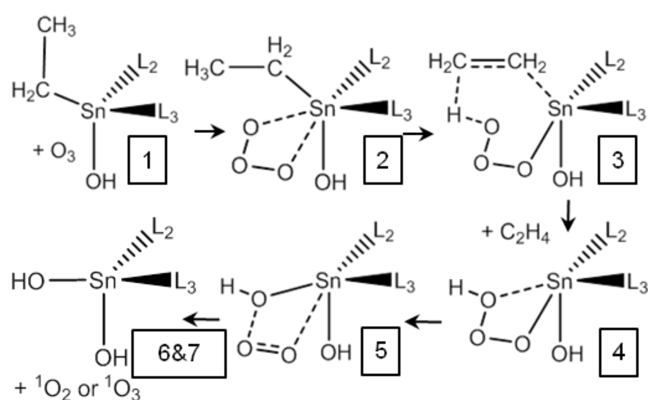

Figure 5.8 Mechanism 2. Reaction coordinate and scheme for ozone abstraction of ethyl ligand hydrogen resulting in ethene elimination and formation of hydroxide functionality. The reaction coordinate follows the conversion of all ethyl ligands to their corresponding hydroxides.

Mechanism two was found to have a lower rate limiting barrier $\Delta G^{\ddagger} = 25.6$ kcal/mol than mechanism one, however the 0.8 kcal/mol difference may not be statistically significant,

resulting in at least two potentially active mechanisms. It should be observed that ethene is the predicted byproduct of pathway 2, however ethene would be subject to further ozonolysis resulting in formaldehyde or methanediol being the likely observed byproduct.

5.3.6 Computational Studies of $SnEt_4$ with Metal Hydroxides

One of the primary observations of alkyltin ALD is the substrate effect on the deposition rate. It has been observed that the ALD deposition rate of SnO_2 from $SnEt_4$ or $SnMe_4$ on Al_2O_3, SiO_2, and ZnO is reduced, however the deposition rate appears unaffected when depositing on TiO_2 or tin(IV) oxide.[29] From the reduced temperature ALD of ZTO films using $SnEt_4$ and O_3 as well as the fit to the Brønsted elimination model presented in this work, it is unlikely that substrate redox chemistry is the active mechanism and another phenomena may be responsible for the observation.

Because ALD of MO_X films has been reported to be promoted by hydroxyl groups, computational chemistry was utilized to study the interaction of various hydroxides represented by gas phase reactions of $Al(OH)_3$, $Si(OH)_4$, $Zn(OH)_2$, $Ti(OH)_4$, $Sn(OH)_4$, and H_2O with the $SnEt_4$ precursor. All computations were performed using the M06 functional and same basis sets and conditions reported earlier. A reaction coordinate was established for each of the reactions and the activation barrier for the elimination of ethane and formation of the M-O-Sn bond compared (Figure 5.9).

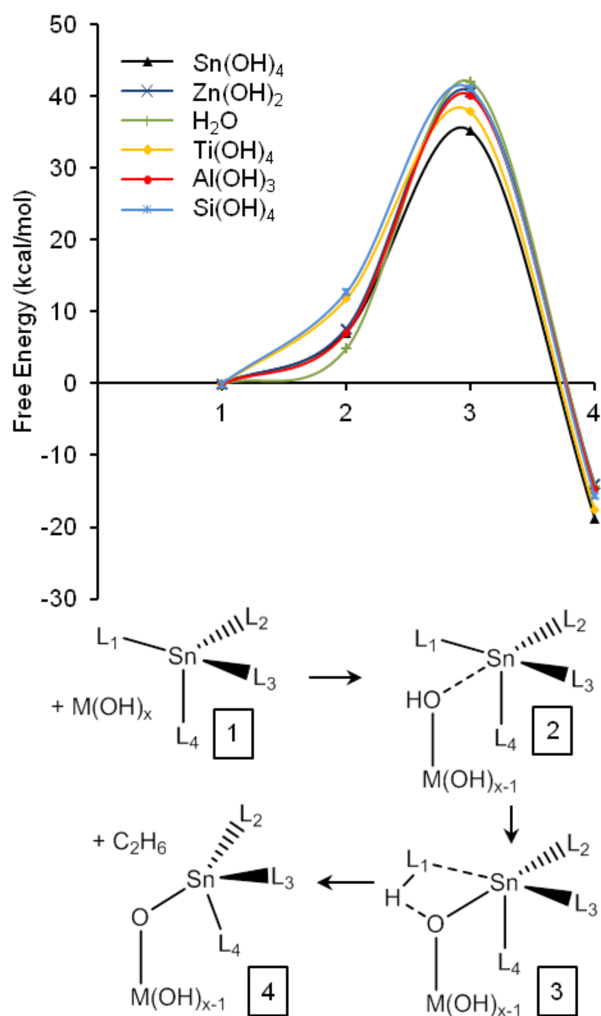

Figure 5.9 Reaction coordinate and scheme for adsorption of $SnEt_4$ on various hydroxide functional groups.

The computations predicted lower activation barriers of for the adsorption step of $SnEt_4$ on Sn and Ti hydroxides when compared to the Al, Si, Zn, and H_2O hydroxides. This prediction is consistent with the observed deposition behavior of alkyltin precursors

on the substrates and oxygen sources mentioned (chapter 4).[29] When compared to an overall 40 kcal/mol barrier, a reduction of 6.7 kcal/mol and 4.0 kcal/mol for the Sn and Ti respectively appears small; however these activation energies would appear in the exponent of a rate equation and have a significant impact on the reaction rate of $SnEt_4$ with the substrate.

The agreement between the computations and experimental observations suggest that the hydroxide behaves differently on different substrates. The likely cause for this difference in hydroxyl functionality is the acidity of the hydroxide's proton. A correlation between the computed activation energies and reported pKa of the different hydroxides was found (Figure 5.10).[122-125] The materials that had the lowest pKa were found to have lower activation barriers. Intuitively this relationship makes sense, that in the transition state, the hydrogen transfer from the hydroxide to the ethyl ligand is similar to a deprotonation event and the material with the most acidic proton (lowest pKa) would help stabilize the transition state resulting in a lower barrier.

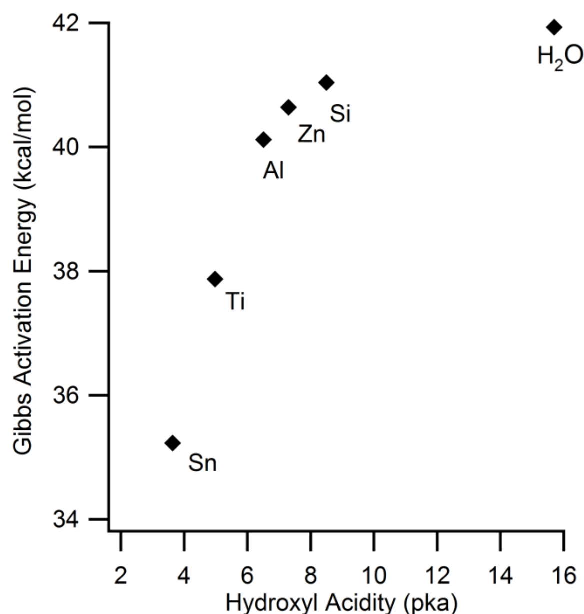

Figure 5.10 Computed activation energy as a function of hydroxyl acidity for the adsorption of $SnEt_4$ on hydroxyl sites.

Arranging the materials according to pKa can be complex, as there can be a wide range of pKa's reported for different surfaces and phases of the material. These considerations were taken into account from a surface chemistry ALD perspective in determining which hydroxyls would be present in significant quantity for adsorbing the alkyltin precursors.

Although silica is known to have acidic silanol groups with pKa ~ 4.5, only 19% of the surface has these acidic protons, the majority of a hydroxilated silica surface (81%) has a pKa close to 8.5.[123] Because the bulk of the silica surface is not acidic, ALD

suppression would still be observed, as there would only be approximately 19% active sites to adsorb the alkyltin precursor.

Both Al_2O_3 and ZnO are amphoteric oxides and appear to have pKa values between 6 and 8 which would make the materials more acidic than the bulk silica surface, but far less acidic than the isolated silanol groups.[122, 124]

Cassiterite SnO_2, is the most acidic oxide in the series and is more acidic than rutile TiO_2, possibly a result of its larger lattice constant with pKa(s) for terminal and bridging hydroxyls calculated to be 3.64 and 5.35 respectively.[125] The greater acidity of SnO_2 over rutile TiO_2 is also reflected in the point of zero charge (pzc) of the materials where cassiterite has an approximate pzc of 3.8-4.5 and rutile TiO_2 has a pzc of 4.8-5.4.[126, 127] The anatase phase of TiO_2 is reported to be more acidic than rutile TiO_2 with a pKa of 4.98, but still less acidic than the terminal cassiterite hydroxyls.[122]

The correlation between surface acidity and the computed activation energy for the alkyltin adsorption step suggests that the observed suppression in ALD deposition rate is a result of less acidic protons available for the surface adsorption step of the alkyl tin precursor.

The acid-base relationship between the precursor and the surface hydroxyl group could possibly explain the less suppressed deposition rate of SnO_X on ZnO using tetrakis(dimethylamido)tin ($Sn(NMe_2)_4$) and cyclic amides of Sn(II) for depositing ZTO films.[38, 119] The activation energy for the hydrogen transfer from a silanol to the $Sn(NMe_2)_4$ precursor, resulting in the elimination of $NHMe_2$ and formation of a tin-hydroxide functionality had a reported activation energy of 17.8 kcal/mol.[35] Additional

reactions of H_2O with $Sn(NMe_2)_4$ showed activation energies of 21.0 kcal/mol for the hydrogen transfer.[35] The difference in activation energies between the silanol and water hydroxyls are consistent with the larger pKa of water over silanol, however, both energy barriers for the $Sn(NMe_2)_4$ are approximately half of the corresponding energy barriers for $SnEt_4$ and silanol or water. This may be a result of the basicity of the nitrogen's lone pair in the NMe_2 ligand promoting the hydrogen abstraction resulting in less SnO_2 suppression on ZnO in ALD ZTO films as well as lower deposition temperatures.[38, 119]

5.4 Conclusions

Tin precursors $SnMe_4$ and $SnBu_3Cl$ have shown self-limiting SnO_2 ALD deposition using O_3 oxidant. The $SnMe_4$ precursor produced polycrystalline rutile SnO_2 films, whereas only amorphous films were observed for the $SnBu_3Cl$ films. In addition, both precursors were found to have similar substrate suppression on ZnO surfaces as had also been observed with $SnEt_4$ precursors and O_3 or N_2O_4 oxygen source (Chapter 4).[29]

Reduced temperature ALD of SnO_2 films using large doses of $SnEt_4$ and O_3 were utilized in order to better understand the ALD chemistry of the alkyltin precursors. The reduced thermal energy in these low temperature depositions were used to ascertain the validity of the thermal pyrolysis of alkyltin precursors and corresponding substrate redox chemistry previously hypothesized as being responsible for substrate suppression of SnO_2 ALD from alkyltin precursors.[29]

The results from the low temperature ALD not only demonstrated that $SnEt_4$ and O_3 could be used to deposit SnO_2 films at 200 °C, but that substrate suppression was still observed on ZnO substrates at these temperatures. The 200 °C deposition temperature appeared to be well below reported decomposition temperatures for $SnEt_4$, suggesting the observed ALD behavior of the alkyltin precursors is not promoted via pyrolysis and may be hydroxyl promoted as reported for other MO_X ALD.[15, 114, 116] Additional ZTO depositions with $SnEt_4$ were fitted with combustion and Brønsted elimination models.[118] The Brønsted elimination model provided the best fit for $SnEt_4$ ALD in ZTO films and also implied that the hydroxyl group is required for adsorption and subsequent elimination of ethane from $SnEt_4$ precursor.

A DFT computational model using gas phase molecules of $SnEt_4$ interacting with hydroxyls of Sn, Ti, Si, Al, Zn, and H_2O was employed to understand what affect the substrate might have on the proton transfer from the hydroxide to the ethyl ligand in the ALD adsorption step. A strong correlation was discovered relating the activation energy for the proton transfer to the pKa of the hydroxide with more acidic oxides having 16% lower activation energies than more basic ones. This correlation is also consistent when compared to the activation energies of $Sn(NMe_2)_4$ with silanol and water where the silanol hydrogen transfer was reported to be 3.2 kcal/mol more favorable.[35]

An acid-base relationship may exist between the tin precursor and the surface hydroxyl as the hydrogen transfer activation energy for the $Sn(NMe_2)_4$ is approximately half that calculated for the $SnEt_4$ precursor. The basicity of the nitrogen's lone pair in the NMe_2 ligand may further stabilize the transition state resulting in lower activation

energies for the ALD adsorption step which in turn produced films which have less SnO_2 substrate suppression as observed in the deposition rate, and lower ALD deposition temperatures when compared to the alkyltin precursors.[38, 119]

From the experiments and computations, it is likely that the alkyltin precursors require a hydroxylated surface for ALD depositions. An additional computational chemistry model was employed to study the O_3 interactions with the ethyl ligand and ascertain how hydroxyl groups may be formed. These computations suggested that two competing mechanisms where plausible where acetaldehyde or ethene could be eliminated. In both mechanisms, a hydroxyl functional group is formed which would promote the adsorption of $SnEt_4$ resulting in SnO_2 films.

REFERENCE

1. S. R. Vishwakarma, J. P. Upadhyay and H. C. Prasad, Thin Solid Films **176** (1), 99-110 (1989).
2. P. Varma and B. S. Ault, J. Phys. Chem. A **112** (25), 5613-5620 (2008).
3. W. H. Baur, Acta Crystallographica Section B-Structural Science **33** (AUG15), 2615-2619 (1977).
4. D. Kovacheva and K. Petrov, Solid State Ionics **109**, 327-332 (1998).
5. M. Micoulaut, Y. Guissani and B. Guillot, Physical Review E **73** (3) (2006).
6. O. H. Johnson, Chem. Rev. (Washington, DC, U. S.) **51**, 431-469 (1952).
7. W. H. Zachariasen, The Journal of Chemical Physics **4** (9), 618-619 (1936).
8. M. J. Hampdensmith, T. A. Wark and C. J. Brinker, Coordination Chemistry Reviews **112**, 81-116 (1992).
9. M. H. Hebb, General Electric Research Laboratory (1959).
10. J. F. Wheeldon, C. E. Valdivia, A. W. Walker, G. Kolhatkar, A. Jaouad, A. Turala, B. Riel, D. Masson, N. Puetz, S. Fafard, R. Ares, V. Aimez, T. J. Hall and K. Hinzer, Progress in Photovoltaics **19** (4), 442-452 (2011).
11. T. Takamoto, E. Ikeda, H. Kurita and M. Ohmori, Applied Physics Letters **70** (3), 381-383 (1997).
12. H. Q. Chiang, J. F. Wager, R. L. Hoffman, J. Jeong and D. A. Keszler, Applied Physics Letters **86** (1) (2005).
13. D. L. Young, H. Moutinho, Y. Yan and T. J. Coutts, Journal of Applied Physics **92** (1), 310-319 (2002).
14. T. Suntola, Thin Solid Films **216** (1), 84-89 (1992).
15. B. S. Lim, A. Rahtu and R. G. Gordon, Nature Materials **2** (11), 749-754 (2003).
16. M. Leskela and M. Ritala, Thin Solid Films **409** (1), 138-146 (2002).
17. R. Matero, A. Rahtu, M. Ritala, M. Leskela and T. Sajavaara, Thin Solid Films **368** (1), 1-7 (2000).
18. S. Haukka, E. L. Lakomaa and A. Root, Journal of Physical Chemistry **97** (19), 5085-5094 (1993).
19. T. A. Krajewski, G. Luka, L. Wachnicki, A. J. Zakrzewski, B. S. Witkowski, M. I. Lukasiewicz, P. Kruszewski, E. Lusakowska, R. Jakiela, M. Godlewski and E. Guziewicz, Semiconductor Science and Technology **26** (8) (2011).
20. H. Yuan, B. Luo, W. L. Gladfelter and S. A. Campbell, ECS Trans. **45**, 389-400 (2012).
21. M. Godlewski, E. Guziewicz, G. Luka, T. Krajewski, M. Lukasiewicz, L. Wachnicki, A. Wachnicka, K. Kopalko, A. Sarem and B. Dalati, Thin Solid Films **518** (4), 1145-1148 (2009).
22. E. Guziewicz, I. A. Kowalik, M. Godlewski, K. Kopalko, V. Osinniy, A. Wojcik, S. Yatsunenko, E. Lusakowska, W. Paszkowicz and M. Guziewicz, Journal of Applied Physics **103** (3) (2008).

23. Y. Widjaja and C. B. Musgrave, Appl. Phys. Lett. **80**, 3304-3306 (2002).
24. S. K. Kim, C. S. Hwang, S. H. K. Park and S. J. Yun, Thin Solid Films **478** (1-2), 103-108 (2005).
25. H. Yuan, B. Luo, D. Yu, A.-j. Cheng, S. A. Campbell and W. L. Gladfelter, J. Vac. Sci. Technol., A **30**, 01A138/131-101A138/138 (2012).
26. E. J. Warner, C. J. Cramer and W. L. Gladfelter, J. Vac. Sci. Technol., A **31**, 041504/041501-041504/041507 (2013).
27. S. K. Kim, C. S. Hwang, S.-H. K. Park and S. J. Yun, Thin Solid Films **478**, 103-108 (2005).
28. H. Yuan, B. Luo, S. A. Campbell and W. L. Gladfelter, Electrochem. Solid-State Lett. **14**, H181-H183 (2011).
29. V. E. Drozd and V. B. Aleskovski, Appl. Surf. Sci. **82/83**, 591-594 (1994).
30. R. G. Gordon, A. S. Hock, J. Heo and P. Sinsermsuksakul, Patent No. WO2011123675A1 (2011).
31. X. Du, Y. Du and S. M. George, Journal of Vacuum Science & Technology A **23** (4), 581-588 (2005).
32. J. W. Elam, D. A. Baker, A. J. Hryn, A. B. F. Martinson, M. J. Pellin and J. T. Hupp, J. Vac. Sci. Technol., A **26**, 244-252 (2008).
33. J. Heo, A. S. Hock and R. G. Gordon, Chem. Mater. **22**, 4964-4973 (2010).
34. J. A. Dean, (2000), Vol. 125, pp. 67.
35. J. T. Tanskanen and S. F. Bent, Journal of Physical Chemistry C **117** (37), 19056-19062 (2013).
36. P. Banerjee, W. J. Lee, K. R. Bae, S. B. Lee and G. W. Rubloff, Journal of Applied Physics **108** (4) (2010).
37. D. Hausmann, J. Becker, S. L. Wang and R. G. Gordon, Science **298** (5592), 402-406 (2002).
38. L. J. Zhong, Z. H. Zhang, S. A. Campbell and W. L. Gladfelter, Journal of Materials Chemistry **14** (21), 3203-3209 (2004).
39. J. Heo, S. B. Kim and R. G. Gordon, Appl. Phys. Lett. **101**, 113507/113501-113507/113505 (2012).
40. A. Heyman and C. B. Musgrave, J. Phys. Chem. B **108** (18), 5718-5725 (2004).
41. A. D. Becke, Journal of Chemical Physics **98** (2), 1372-1377 (1993).
42. S. D. Elliott, G. Scarel, C. Wiemer, M. Fanciulli and G. Pavia, Chem. Mater. **18** (16), 3764-3773 (2006).
43. G. Prechtl, A. Kersch, G. S. Icking-Konert, W. Jacobs, T. Hecht, H. Boubekeur and U. Schroeder, Tech. Dig. - Int. Electron Devices Meet., 245-248 (2003).
44. H. B. Stoner, J. M. Barnes and J. I. Duff, British Journal of Pharmacology and Chemotherapy **10** (1), 16-25 (1955).
45. M. Ohring, *Material Science of Thin Films*, 2nd ed. (Academic Press, 2001).
46. J. A. Bearden, Reviews of Modern Physics **39** (1), 78-124 (1967).
47. A. R. West, *Basic Solid State Chemistry*, 2nd ed. (Wiley, 1999).
48. G. Binnig, C. F. Quate and C. Gerber, Physical Review Letters **56** (9), 930-933 (1986).

49. D. A. M. J. D. Simon, *Physical Chemistry A Molecular Approach*. (University Science Books, 1997).
50. L. J. v. d. PAUW, Philips Technical Review **20**, 220-224 (1958).
51. P. Varma and B. S. Ault, The Journal of Physical Chemistry A **112** (25), 5613-5620 (2008).
52. J. Kwon, M. Dai, M. D. Halls and Y. J. Chabal, Applied Physics Letters **97** (16) (2010).
53. J. H. Kwon, M. Dai, M. D. Halls and Y. J. Chabal, Chemistry of Materials **20** (10), 3248-3250 (2008).
54. Z. Hu, J. X. Shi and C. Heath Turner, Molecular Simulation **35** (4), 270-279 (2009).
55. C. J. Cramer, *Essentials of Computational Chemistry second edition Theories and Models*. (Wiley, West Sussex, 2004).
56. M. J. F. *e. al*. (Gaussian, Inc., Wallingford CT,, 2009).
57. Y. Zhao and D. Truhlar, Theoretical Chemistry Accounts **120** (1-3), 215-241 (2008).
58. H. U. Lee and R. N. Zare, Combust. Flame **24**, 27-34 (1975).
59. D. N. Goldstein, J. A. McCormick and S. M. George, J. Phys. Chem. C **112** (49), 19530-19539 (2008).
60. M. Rose, J. Niinisto, I. Endler, J. W. Bartha, P. Kucher and M. Ritala, ACS Appl. Mater. Interfaces **2**, 347-350 (2010).
61. K. Knapas and M. Ritala, Chem. Mater. **23**, 2766-2771 (2011).
62. D. J. Comstock and J. W. Elam, Chem. Mater. **24** (21), 4011-4018 (2012).
63. Y. Zhao and D. G. Truhlar, J. Chem. Phys. **125**, 194101/194101-194101/194118 (2006).
64. L. R. Warren J Hehre, P. von R. Schleyer, John Pople, *Ab Initio Molecular Orbital Theory*. (Wiley-Interscience, New York, 1986).
65. C. J. Cramer, *Essentials of Computational Chemistry Theories and Models*, 2nd ed. (Wiley, 2004).
66. Y. Zhao and D. G. Truhlar, Theor. Chem. Acc. **120** (1-3), 215-241 (2008).
67. M. J. T. Frisch, G. W.; Schlegel, H. B.; Scuseria, G. E.; Robb, M. A.; Cheeseman, J. R.; Scalmani, G.; Barone, V.; Mennucci, B.; Petersson, G. A.; Nakatsuji, H.; Caricato, M.; Li, X.; Hratchian, H. P.; Izmaylov, A. F.; Bloino, J.; Zheng, G.; Sonnenberg, J. L.; Hada, M.; Ehara, M.; Toyota, K.; Fukuda, R.; Hasegawa, J.; Ishida, M.; Nakajima, T.; Honda, Y.; Kitao, O.; Nakai, H.; Vreven, T.; Montgomery, Jr., J. A.; Peralta, J. E.; Ogliaro, F.; Bearpark, M.; Heyd, J. J.; Brothers, E.; Kudin, K. N.; Staroverov, V. N.; Kobayashi, R.; Normand, J.; Raghavachari, K.; Rendell, A.; Burant, J. C.; Iyengar, S. S.; Tomasi, J.; Cossi, M.; Rega, N.; Millam, J. M.; Klene, M.; Knox, J. E.; Cross, J. B.; Bakken, V.; Adamo, C.; Jaramillo, J.; Gomperts, R.; Stratmann, R. E.; Yazyev, O.; Austin, A. J.; Cammi, R.; Pomelli, C.; Ochterski, J. W.; Martin, R. L.; Morokuma, K.; Zakrzewski, V. G.; Voth, G. A.; Salvador, P.; Dannenberg, J. J.; Dapprich, S.;

Daniels, A. D.; Farkas, Ö.; Foresman, J. B.; Ortiz, J. V.; Cioslowski, J.; Fox, D. J. , (Wallingford CT, 2009).

68. H. Yuan, B. Luo, S. A. Campbell and W. L. Gladfelter, Electrochem. Solid-State Lett. **14**, H181-H183 (2011).
69. H. Yuan, B. Luo, D. Yu, A.-j. Cheng, S. A. Campbell and W. L. Gladfelter, J. Vac. Sci. Technol., A **30**, 01A138/131-101A138/138 (2012).
70. S. M. George, Chem. Rev. **110**, 111-131 (2010).
71. J. Auld, D. J. Houlton, A. C. Jones, S. A. Rushworth, M. A. Malik, P. O'Brien and G. W. Critchlow, J. Mater. Chem. **4**, 1249-1253 (1994).
72. M. Ishimori, T. Hagiwara, T. Tsuruta, Y. Kai, N. Yasuoka and N. Kasai, Bull. Chem. Soc. Jpn. **49**, 1165-1166 (1976).
73. T. Akimoto, M. Maeda, A. Tsuji and Y. Iitaka, Chem. Pharm. Bull. **27**, 424-434 (1979).
74. A. C. Voukides, K. M. Konrad and R. P. Johnson, J. Org. Chem. **74** (5), 2108-2113 (2009).
75. E. A. Zaburdaeva, V. A. Dodonov and L. P. Stepovik, J. Organomet. Chem. **692** (6), 1265-1268 (2007).
76. R. Schmidt, J Phys Chem A **110**, 2622-2628 (2006).
77. R. J. Herold, S. L. Aggarwal and V. Neff, Can. J. Chem. **41**, 1368-1380 (1963).
78. L. Jeloaica, A. Esteve, R. M. Djafari and D. Esteve, Appl. Phys. Lett. **83**, 542-544 (2003).
79. M. D. Halls, K. Raghavachari, M. M. Frank and Y. J. Chabal, Phys. Rev. B: Condens. Matter Mater. Phys. **68**, 161302/161301-161302/161304 (2003).
80. L. Nyns, A. Delabie, G. Pourtois, E. S. Van, C. Vinckier and G. S. De, J. Electrochem. Soc. **157**, G7-G12 (2010).
81. A. Delabie, S. Sioncke, J. Rip, E. S. Van, M. Caymax, G. Pourtois and K. Pierloot, J. Phys. Chem. C **115**, 17523-17532 (2011).
82. A. Delabie, S. Sioncke, J. Rip, E. S. Van, G. Pourtois, M. Mueller, B. Beckhoff and K. Pierloot, J. Vac. Sci. Technol., A **30**, 01A127/121-101A127/110 (2012).
83. Y. Widjaja and C. B. Musgrave, Appl. Phys. Lett. **80**, 3304-3306 (2002).
84. J. Ren, G. Zhou, Y. Hu, H. Jiang and D. W. Zhang, Appl. Surf. Sci. **254**, 7115-7121 (2008).
85. Y. Xu and C. B. Musgrave, Chem. Mater. **16**, 646-653 (2004).
86. S. W. Benson and A. E. Axworthy, Jr., J. Chem. Phys. **26**, 1718-1726 (1957).
87. S. T. Oyama, Catal. Rev. - Sci. Eng. **42**, 279-322 (2000).
88. K. M. Bulanin, J. C. Lavalley and A. A. Tsyganenko, Colloid Surface A **101** (2-3), 153-158 (1995).
89. K. M. Bulanin, J. C. Lavalley and A. A. Tsyganenko, J. Phys. Chem. **99** (25), 10294-10298 (1995).
90. Y. Wang, I. Ramos and J. J. Santiago-Aviles, J. Appl. Phys. **102**, 093517/093511-093517/093515 (2007).

91. X. Q. Pan and L. Fu, J. Appl. Phys. **89**, 6048-6055 (2001).
92. R. Dolbec, M. A. El Khakani, A. M. Serventi, M. Trudeau and R. G. Saint-Jacques, Thin Solid Films **419** (1-2), 230-236 (2002).
93. J. Heo, S. B. Kim and R. G. Gordon, J. Mater. Chem. **22**, 4599-4602 (2012).
94. M. A. Alpuche-Aviles and Y. Y. Wu, Journal of the American Chemical Society **131** (9), 3216-3224 (2009).
95. W. S. Choi, Journal of the Korean Physical Society **57** (6), 1472-1476 (2010).
96. H. Yuan, B. Luo, S. A. Campbell and W. L. Gladfelter, Electrochem. Solid-State Lett. **14**, H181-H183 (2011).
97. Epichem, (2000).
98. M. Ohring, *Materials Science of Thin Films 2nd edition*. (1992).
99. B. Stjerna, E. Olsson and C. G. Granqvist, Journal of Applied Physics **76** (6), 3797-3817 (1994).
100. B. B. Burton, M. P. Boleslawski, A. T. Desombre and S. M. George, Chem. Mat. **20** (22), 7031-7043 (2008).
101. Y. Inaguma, M. Yoshida and T. Katsumata, J. Am. Chem. Soc. **130**, 6704-6705 (2008).
102. H. Gou, J. Zhang, Z. Li, G. Wang, F. Gao, R. C. Ewing and J. Lian, Appl. Phys. Lett. **98**, 091914/091911-091914/091913 (2011).
103. G. J. Exarhos and S. K. Sharma, Thin Solid Films **270** (1–2), 27-32 (1995).
104. H. Kidowaki, T. Oku and T. Akiyama, Int. J. Res. Rev. Appl. Sci. **13**, 67-72 (2012).
105. S. Whangbo, H. Jang, S. Kim, M. Cho, K. Jeong and C. Whang, J. Korean Phys. Soc. **37**, 456-460 (2000).
106. S. M. Rozati and E. Shadmani, Digest Journal of Nanomaterials and Biostructures **6** (2), 365-372 (2011).
107. F. Pern, R. Noufi, B. To, C. DeHart, X. Li and S. Glick, presented at the Solar Energy+ Applications, 2008 (unpublished).
108. S. Ishibashi, Y. Higuchi, Y. Ota and K. Nakamura, Journal of Vacuum Science & Technology A **8** (3), 1403-1406 (1990).
109. A. G. Zawadzki, C. J. Giunta and R. G. Gordon, The Journal of Physical Chemistry **96** (13), 5364-5379 (1992).
110. Y. Xu and C. B. Musgrave, Chem. Mat. **16** (4), 646-653 (2004).
111. S. Kannan Selvaraj, A. Feinerman and C. G. Takoudis, Journal of Vacuum Science & Technology A **32** (1), - (2014).
112. H. Viirola and L. Niinistö, Thin Solid Films **249** (2), 144-149 (1994).
113. X. Du, Y. Du and S. M. George, Journal of Vacuum Science & Technology A **23** (4), 581-588 (2005).
114. X. Du and S. M. George, Sensors and Actuators B: Chemical **135** (1), 152-160 (2008).
115. A. Ashworth and P. G. Harrison, Journal of Organometallic Chemistry **487** (1–2), 257-262 (1995).
116. K. Tamaru, The Journal of Physical Chemistry **60** (5), 610-612 (1956).

117. S. M. George, A. W. Ott and J. W. Klaus, The Journal of Physical Chemistry **100** (31), 13121-13131 (1996).
118. M. Leskelä and M. Ritala, Thin Solid Films **409** (1), 138-146 (2002).
119. S. D. Elliott and O. Nilsen, ECS Trans. **41** (2), 175-183 (2011).
120. M. N. Mullings, C. Hagglund, J. T. Tanskanen, Y. Yee, S. Geyer and S. F. Bent, Thin Solid Films **556**, 186-194 (2014).
121. D. H. Giamalva, D. F. Church and W. A. Pryor, Journal of the American Chemical Society **108** (24), 7678-7681 (1986).
122. E. Reisz, A. Fischbacher, S. Naumov, C. von Sonntag and T. C. Schmidt, Ozone: Science & Engineering, null-null (2014).
123. P. W. Schindler and H. Gamsjäger, Kolloid-Zeitschrift und Zeitschrift für Polymere **250** (7), 759-763 (1972).
124. K. Leung, I. M. B. Nielsen and L. J. Criscenti, Journal of the American Chemical Society **131** (51), 18358-18365 (2009).
125. K. a. Koike, *Advances in Inorganic Chemistry*. (1996).
126. G. Korotcenkov, *Chemical Sensors: Simulation and Modeling*. (2012).
127. J. Cheng and M. Sprik, Journal of Chemical Theory and Computation **6** (3), 880-889 (2010).
128. M. Kosmulski, *Surface Charging and Points of Zero Charge*. (CRC Press, 2009).